Università degli Studi di Pisa

DIPARTIMENTO DI FISICA "E. FERMI"
Corso di Laurea Magistrale in Fisica

TESI DI LAUREA MAGISTRALE IN FISICA

Search for $e^+e^- \to \mu^+\mu^- Z'\,(Z' \to \text{Invisible})$ in the first data of the *Belle*II experiment

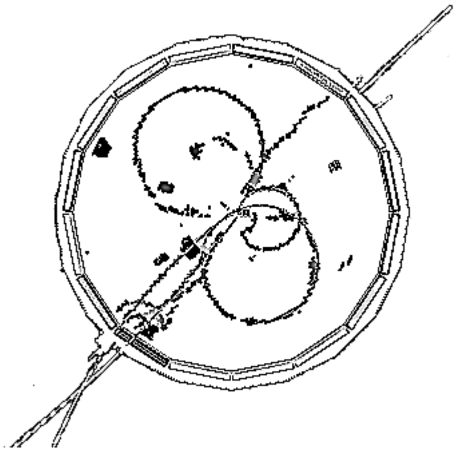

Candidato:
Luigi Corona

Relatore:
Prof. Francesco Forti

Anno Accademico 2017-2018

Contents

Introduction

The thesis work concerns the search for the process $e^+e^- \to \mu^+\mu^- Z'\,(Z' \to \text{Invisible})$ with the first data of the *Belle*II experiment, collected in the data taking period known as *Phase*-2 (February 2018 - July 2018). This work includes also the development of the calibration method of the algorithm used by the *Silicon Vertex Detector* (SVD) of *Belle*II to estimate the *hit time* of particles crossing each sensor. The SVD is a detector equipped with double-sided silicon strip sensors used for the reconstruction of charged particle tracks. Together with the *Pixel Detector* (PXD), it constitutes the vertex detector of the experiment. The *Belle*II experiment is installed on the SuperKEKB accelerator, which is an asymmetric electron-positron collider, located on KEK laboratory, Tsukuba, Japan.

The *Standard Model* (SM) is the theory that currently describes the known particles and their interactions. Recently some tensions between the theoretical predictions of the SM and the experimental measurements have been observed. For example the measurement of the anomalous magnetic moment of the muon $(g-2)_\mu$ deviates from the SM prediction by 3.4σ, while the lepton flavor universality test performed by the LHCb, BABAR and *Belle* experiments shows a deviation from the SM prediction of 4.1σ. These deviations can be explained by extensions of the SM that predict a collection of hypothetical hidden particles that could interact with SM particles, although very weakly, through new gauge bosons called *dark photons*.

The purpose of this thesis is to investigate the production of a light dark gauge boson Z' in association with a muon pair in electron-positron annihilation at the center of mass energy of 10.58 GeV. Through this analysis it is possible to limit the $L_\mu - L_\tau$ model, which introduces the boson Z' by extending the symmetry group of the SM, $U(1)_Y \otimes SU(2)_L \otimes SU(3)_C$, with the abelian group $U(1)_{L_\mu - L_\tau}$. This new symmetry introduces an interaction term of the Z' boson with muons and tauons and it preserves the difference between the μ-leptonic number and the τ-leptonic number in the processes.
The $L_\mu - L_\tau$ model is theoretically very well motivated and could explain some of the observed experimental effects.

The process analyzed is $e^+e^- \to \mu^+\mu^- Z', (Z' \to \text{Invisible})$, where the muon pair is produced at the $\Upsilon(4S)$ energy peak and the Z' boson is radiatively emitted by one of the two muons. The signature of the process consists of two muon tracks coming from the interaction point plus missing mass. The signal yield is extracted by fitting the distribution of the recoil mass against the muon pair with respect to the center of mass momentum, which is expected to peak at the Z' mass $M_{Z'}$ for signal events. The considered background processes are $e^+e^- \to \mu^+\mu^-(\gamma)$ where the photon is not detected, $e^+e^- \to \tau^+\tau^-\gamma, \tau \to \mu\nu$ and $e^+e^- \to e^+e^-\mu^+\mu^-$ where the two electrons are undetected. The recoil mass distribution of the first process peaks at small recoil masses, the second dominates $2 \lesssim M_{recoil} \lesssim 7$ GeV/c^2 and the last one dominates for $M_{recoil} \gtrsim 7$ GeV/c^2.

The MC samples produced for the analysis consist of 10 thousand signal events for eight different mass hypotheses and 10 fb^{-1} background events for each considered background process. In order to reject background, a selection in two steps, based on the kinematics of the events and on the particle identification, has been performed. The first selection requires events with two muon track, i.e. two tracks characterized by a probability to be identified as muon higher than 90%, coming from the *interaction point* and in which the direction of the recoil points to the barrel region of the ECL without photons inside a cone of 15^o from the direction of the recoil. Including a trigger efficiency of ~82%, for $M_{Z'}$ in the range [1,8] GeV/c^2, the total efficiency of the preselection is ~35%.
A further selection based on possible discriminant variables between signal events and background events has been performed. Many variables are under study yet and currently only the transverse momentum of the dimuon candidate $p_{T\mu\mu}$ has been considered for the background rejection. The selection has been optimized for each Z' mass considered.

The range of Z' mass considered in the analysis goes from 1 GeV/c^2 to 8 GeV/c^2, since the poor mass resolution for $M_{Z'} \lesssim 1$ GeV/c^2 (the resolution for $M_{Z'} \sim 500MeV$ is around 150 MeV) and the small cross section estimated for $M_{Z'} \gtrsim 8$ GeV/c^2 through the MC simulation limit the sensitivity to signal events for $M_{Z'}$ out of the considered range.

This analysis allowed to estimate the sensitivity region to the parameters of the $L_\mu - L_\tau$ model at a $CL = 90\%$, assuming $Z' \to \nu_{\mu,\tau}\bar{\nu_{\mu,\tau}}$ and $Z' \to \chi\bar{\chi}$, where χ is a dark matter particle lighter than the Z' boson.

The sensitivity has been estimated for the following integrated luminosities: 20 fb^{-1}, which is the luminosity that was expected for *Phase*-2, 2 ab^{-1} and 50 ab^{-1}, which is the full data set expected for the end of the *Belle*II experiment. With an integrated luminosity of 20 fb^{-1}, *Belle*II is already competitive with the other experiments, while with an integrated luminosity of 50 fb^{-1} a wide part of the region of parameters that can explain the $(g-2)_\mu$ anomaly is excluded.

Finally, a very preliminary comparison between the 505 pb^{-1} of data actually collected during the *Phase*-2 and the produced MC samples has been performed.

In addition, the calibration method of the algorithm used by SVD to estimate the *hit time* of particles that cross each sensor is presented, which is very important to be able to use precise timing information to reject different background sources, events which are off-time with respect to the event time, and *ghost hits*. The method consists of correcting the SVD *hit time* estimation using the timing information provided by the CDC, the only ones available, as reference. The final resolution on the *hit time* obtained is of ~4 ns for the V/n-side of the sensors.

Chapter 1 is dedicated to a brief introduction of the *Standard Model* by describing the fundamental interactions and particle contents of the model, together with a brief description of the formalism of the $\mathcal{CP}$ violation, which has been investigated in depth in the first generation of B-Factories. A brief description of some shortcomings of the *Standard Model* and some tensions between its theoretical prediction and the experimental measurements, which could be explained extending the *Standard Model*, is provided. *Dark matter* and different models that could explain its nature and its abundance in the Universe are also briefly introduced, with the focus on the experimental methods developed for its detection. A brief discussion of the *dark sector* introduced by extending the *Standard Model*, with the focus on the $L_\mu - L_\tau$ model, and a description of the current experimental limits on different *dark sector* models is presented. Finally, the motivations behind the study of the process analyzed in this thesis work are discussed.

Chapter 2 is dedicated to a general description of the B-Factories, in particular for what concerns the physics that can be investigated by these experiments and the analysis methods used. A general description of the detectors used in these experiments and finally the characteristic of the electron-positron colliders with the focus on the SuperKEKB collider, which is the accelerator that provides the luminosity to the *Belle*II experiment, is provided. In this chapter the main differences between the first generation of the B-Factories and the *Belle*II experiment are discussed.

Chapter 3 is dedicated to the detailed description of the *Belle*II detector and also a brief description of the *Belle*II software and computing is provided.

Chapter 4 regards the description of the method developed for the calibration of the *Silicon Vertex Detector* algorithm that estimates the *hit time* of particles that cross the sensors.

Chapter 5 is dedicated to an overview of the analysis of the process $e^+e^- \to \mu^+\mu^- Z'(Z' \to$ Invisible) describing the characteristics of the signal events and of the background processes, as well as the kinematic variable and the methods used to extract the signal. Finally the description of the MC samples used for the analysis and of the tools used to produce them will be provided.

Chapter 6 is dedicated to the description of the selection used to reject the background events and of the method used to optimize the selection based on the transverse momentum of the dimuon candidate, that consists of maximizing the *Punzi Figure of Merit*. The values obtained from the optimization are used to give an estimation of the sensitivity to the parameter of the $L_\mu - L_\tau$ model that can be reached through this analysis for different integrated luminosities.

Finally, this thesis will conclude with the discussion about the results obtained from the analysis here presented, the future perspectives of this analysis at *Belle*II and a preliminary data-MC comparison with the current available sample of 505 pb^{-1}, collected during the data taking period known as *Phase*-2 (February 2018 - July 2018).

Chapter 1

Theoretical Overview

The Standard Model (SM) describes successfully the phenomenology of the constituent particles of matter and their interactions, but it is an incomplete theory. It is known that the 26% of the matter of the Universe is composed by *dark matter* (DM) of which gravitational effects are observed. However, the SM does not contain a description of DM. Furthermore, experiments observed some tensions between the SM predictions and experimental results that suggest the possibility to include new physics through a more extended theory than current SM. A possibility to include new physics that could explain discrepancies and describe DM is what is called *dark sector*. It foresees a new group of particles that interact with SM particles, although very weakly, and hence it is possible in principle to observe them in precision experiments. In this chapter the SM and DM are briefly introduced and some possible extension of the SM are described, emphasizing the $L_\mu - L_\tau$ model that is of particular interest for this thesis work. The possibility to investigate the *dark sector* in accelerators will also be covered, in particular for what concerns invisible decays of the dark boson Z', which is the topic of this thesis.

1.1 Introduction to the Standard Model

The Standard Model of fundamental interactions (SM) is the theory that describes the constituent particles of matter and three of the four fundamental physics interactions between particles: the electromagnetic interaction, the weak interaction and the strong interaction.

Elementary particles are divided in two big families: fermions, with half-integer spin, following the Fermi-Dirac statistics and bosons, with integer spin and following the Bose-Einstein statistics. Matter is composed by fermions that are grouped in three generations of quarks and leptons.

Leptons are sensitive to electromagnetic and weak interactions while quarks are sensitive to all three kinds of interactions. The three generations of leptons are organized in doublets composed by a charged lepton (e, μ, τ) with charge $-e$, which interact electromagnetically and weakly, and by a neutral lepton, neutrino, which interact only weakly. A different lepton number, $L_{e,\mu,\tau}$, is associated to each generation: it is a conserved quantum number in interactions. An anti-lepton with the same mass of the respective lepton and opposite quantum numbers is associated to each lepton.

The three generations of quarks are organized in doublets of u-type quarks, characterized by a charge of $+2/3e$, and d-type quarks, characterized by a charge of $-1/3e$. Each of six quarks has a different flavour. An anti-quark with the same mass of the respective quark and opposite quantum numbers is associated to each quark. Quarks have an additional quantum number connected to strong interactions called *color*. Differently from leptons, it is not possible to observe isolated quarks because of the phenomenon called *confinement*, derived in the theory of strong interactions, implying that only color singlets can be observed. Two kinds of color singlets are known, bound states of two quarks, mesons, or three quarks, baryons.

The division in three generations of leptons and quarks gives rise to a mass hierarchy: see the Table 1.1 [1].

Leptons				Quarks			
Charge	$L_e = 1$	$L_\mu = 1$	$L_\tau = 1$	Charge			
0 $-$ 1	$\begin{pmatrix}\nu_e\\ e\end{pmatrix}$	$\begin{pmatrix}\nu_\mu\\ \mu\end{pmatrix}$	$\begin{pmatrix}\nu_\tau\\ \tau\end{pmatrix}$	+ 2/3 $-$ 1/3	$\begin{pmatrix}u\\ d\end{pmatrix}_i$	$\begin{pmatrix}c\\ s\end{pmatrix}_i$	$\begin{pmatrix}t\\ b\end{pmatrix}_i$
$M_e = 0.511$ MeV$/c^2$ $M_\mu = 105.7$ MeV$/c^2$ $M_\tau = 1777$ MeV$/c^2$ $M_\nu \sim$ eV$/c^2$				$M_u = 2.2$ MeV$/c^2$ $M_d = 4.7$ MeV$/c^2$ $M_c = 1.28$ GeV$/c^2$ $M_s = 96$ MeV$/c^2$ $M_t = 173.1$ GeV$/c^2$ $M_b = 4.18$ GeV$/c^2$			

Table 1.1: Elementary fermions of the SM. The $i = 1, 2, 3$ subscript in quarks generations is the number of colors. Each quark exists in three different colors and in the SM there are six leptons and eighteen quarks. To each of these particles is associated an anti-particle. The value of masses reported in this table are taken from the Particle Data Group (PDG) [2].

The SM is a quantum gauge theory based on the symmetry group $U(1)_Y \otimes SU(2)_L \otimes SU(3)_C$, where L stands for left-handed. The electroweak theory (EW) (the unified theory of electromagnetic interaction (QED) and weak interaction) is described by the gauge group $U(1)_Y \otimes SU(2)_L$. It introduces the vectorial gauge fields B_μ, relative to $U(1)_Y$, and W^a_μ where $a = 1, 2, 3$, relative to $SU(2)_L$. After spontaneous symmetry breaking $U(1)_Y \otimes SU(2)_L \to U(1)_{e.m.}$ and diagonalization of the gauge boson mass terms, the photon A_μ and the weak interaction bosons, $W^\pm_\mu$ and Z_μ, become explicit fields in the theory. There is no mass term associated to the gauge field of the photon because of the residual symmetry of the Lagrangian under the group $U(1)_{e.m.}$, while the mass terms of the gauge fields $W^\pm_\mu$ and Z_μ appear explicitly in the theory. The spontaneous Lagrangian gauge symmetry breaking is possible through the introduction of the complex scalar field ϕ, known as Higgs field, that induces the potential $V(\phi\phi^\dagger)$. This potential allows the spontaneous symmetry breaking because its ground state is not invariant under the symmetry. This mechanism is known as Higgs mechanism and it explains how fermions take mass interacting with the Higgs field.

The strong interaction theory is described by quantum chromodynamics (QCD) and it is based on the gauge group $SU(3)_C$ that introduces the vectorial gauge fields of the gluons, G^A_μ where $A = 1, ..., 8$.

From this theoretical framework it is derived that interactions are mediated by spin-1

gauge bosons. The photon γ is the non-massive mediator of electromagnetic interactions, the $W^{\pm}$ bosons are the massive mediators of the charged current weak interaction, the Z^0 boson is the massive mediator of the neutral current weak interaction and finally the eight gluons g are the non-massive mediators of the strong interaction between quarks.
The theory is completed by the massive scalar Higgs boson that is introduced in the SM through the Higgs mechanism. SM bosons are shown in Table 1.2 [1].

Weak ($s = 1$)	Electromagnetic ($s = 1$)	Strong ($s = 1$)	Higgs ($s = 0$)
$W^{\pm}$, Z^0	γ	g_A	H
$M_{W^{\pm}} = 80.4$ GeV/c^2 $M_{Z^0} = 91.2$ GeV/c^2	$M_{\gamma} = 0$ GeV/c^2	$M_g = 0$ GeV/c^2	$M_H = 125$ GeV/c^2

Table 1.2: Elementary bosons of the SM. The photons, the Z^0 boson and gluons are electromagnetically discharged and they have no anti-particles associated to them. Gluon carry the color charge, the quantum number connected to strong interaction. The $A = 1, ..., 8$ subscript denotes the eight gluons. W^- and W^+ bosons are electromagnetically charged and W^- is the anti-particle of W^+.

The lagrangian of the SM is [1]:

$$\begin{aligned}
\mathscr{L} &= \mathscr{L}_{kin} + \mathscr{L}_{EW} + \mathscr{L}_{QCD} + \mathscr{L}_{Higgs} + \mathscr{L}_{Y} \\
\mathscr{L}_{kin} &= -\frac{1}{4} B_{\mu\nu} B^{\mu\nu} - \frac{1}{4} W^{a}_{\mu\nu} W^{\mu\nu}_{a} - \frac{1}{4} G^{A}_{\mu\nu} G^{\mu\nu}_{A} \\
\mathscr{L}_{EW} &= \bar{\psi}_f \gamma^{\mu} \left(i\partial_{\mu} - \frac{1}{2} g' Y_W B_{\mu} - \frac{1}{2} g \tau_a W^{a}_{\mu} \right) \psi_f \\
\mathscr{L}_{QCD} &= \bar{\psi}_{f,i} \gamma^{\mu} \left(g_S G^{A}_{\mu} T_{A,ij} \right) \psi_{f,j} \\
\mathscr{L}_{Higgs} &= \frac{1}{2} \left| \left(\partial_{\mu} - \frac{1}{2} g' Y_{\phi} B_{\mu} - \frac{1}{2} g \tau_a W^{a}_{\mu} \right) \phi \right|^2 - V(\phi^{\dagger}\phi) \\
\mathscr{L}_{Y} &= \lambda_y \bar{e}^{\alpha}_{L} \phi e^{\alpha}_{R} - \Lambda_{\alpha\beta} \left(\bar{d}^{\alpha}_{L} \phi d^{\beta}_{R} \right) - \Lambda'_{\alpha\beta} \left(\bar{u}^{\alpha}_{L} \tilde{\phi} u^{\beta}_{R} \right) + h.c.
\end{aligned} \tag{1.1}$$

The couplings g and g' are associated with B_{μ} and W^{a}_{μ}. Y_W is the value of the weak hypercharge of the fermions that interact with the B_{μ} field, while Y_{ϕ} is the value of the weak hypercharge of the ϕ field and τ_a are the Pauli matrices whose eigenvalues are the isospin of particles interacting with the $W^{\pm}$ fields. The λ_y coupling is the Yukawa coupling between leptons and the Higgs field, $\Lambda_{\alpha\beta}$ and $\Lambda'_{\alpha\beta}$ are the matrix of Yukawa coupling, respectively between d-type quarks and the Higgs field and between u-type quarks and the Higgs field. The ψ fields are associated with fermions.

$\mathscr{L}_{kin}$ is the kinetic term of gauge bosons and it contains also the autointeraction terms of gauge bosons of weak and strong interactions. $\mathscr{L}_{EW}$ is the electroweak theory, describing the interaction between fermions and $U(1)_Y \otimes SU(2)_L$ gauge bosons. The term with the partial derivative is the kinetic term of fermions. $\mathscr{L}_{QCD}$ is the quark-gluons interaction term, g_S is the coupling of strong interaction, $f = 1, ..., 6$ is the flavour index and $i = 1, 2, 3$ is the color index. $\mathscr{L}_{Higgs}$ describes the interactions of the Higgs boson with gauge bosons of electroweak theory, its autointeractions and its kinetic term. $\mathscr{L}_{Y}$ describes interactions between fermions and Higgs field. In this last term of the Lagrangian fermions are represented as doublets (left-handed components) and singlets (right-handed components) of

$SU(2)_L$: $e_L^\alpha = \left(\nu_L^\alpha, e_L^\alpha\right)$ is the lepton doublet, ν_L^α is the discharged component of the doublet while e_L^α is the charged component with charge $-e$, while e_R^α is the lepton singlet with charge $+e$. The u_L^α and d_L^α terms represents respectively the u-type quarks component and the d-type quarks component of the quark doublet $q_L^\alpha = \left(u_L^\alpha, d_L^\alpha\right)$, while u_R^α and d_R^α are the respective quarks singlets. The $\alpha = 1, 2, 3$ parameter represents the number of fermion generations. Also the Higgs field ϕ is a doublet of $SU(2)_L$, hence the gauge invariance of $\mathscr{L}_Y$ is preserved [1].

The flavour changing transitions between quarks are mediated by charged current weak interactions. Nicola Cabibbo explained for the first time that the transitions between up-type and down-type quarks are possible in weak interactions, although the transitions between quarks that belong to different generations are suppressed with respect to transitions between quarks belonging to the same generation [3]. In order to explain the suppression, he introduced the eigenstates of weak interactions (d', s') as a linear combination of the eigenstates of mass (d, s) that can be expressed through the mixing matrix in Equation 1.2, where θ_C is called Cabibbo angle and from experimental observations Cabibbo estimated that $\theta_C \simeq 0.23$.

$$\begin{pmatrix} d' \\ s' \end{pmatrix} = \begin{pmatrix} cos\theta_C & sin\theta_C \\ -sin\theta_C & cos\theta_C \end{pmatrix} \begin{pmatrix} d \\ s \end{pmatrix} \tag{1.2}$$

The Cabibbo theory explains the flavour changing transitions if only two quark families are considered. The extension to three quark families is provided by the Cabibbo-Kobayashi-Maskawa (CKM) mixing matrix of quarks, which contains the probability of transitions. The CKM matrix have four free parameters: three real angles θ_{ij} and one complex phase δ that is responsible for the $\mathcal{CP}$ violation in weak interactions as shown in the following equation that shows the CKM matrix in the standard parametrization [1].

$$\begin{aligned} V_{ij} &= \begin{pmatrix} V_{ud} & V_{us} & V_{ub} \\ V_{cd} & V_{cs} & V_{cb} \\ V_{td} & V_{ts} & V_{tb} \end{pmatrix} = \\ &= \begin{pmatrix} c_{12}c_{13} & s_{12}c_{13} & s_{13}e^{i\delta} \\ -s_{12}c_{13} - c_{12}s_{13}s_{23}e^{i\delta} & c_{12}c_{23} - s_{12}s_{13}s_{23}e^{i\delta} & c_{13}s_{23} \\ s_{12}s_{23} - c_{12}s_{13}c_{23}e^{i\delta} & -c_{12}s_{23} - s_{12}s_{13}c_{23}e^{i\delta} & c_{13}c_{23} \end{pmatrix} \end{aligned} \tag{1.3}$$

The c_{ij} and s_{ij} terms are respectively defined as $c_{ij} = cos\theta_{ij}$ and $s_{ij} = sin\theta_{ij}$. The complex phase $i\delta$ is responsible for the $\mathcal{CP}$ violation.

The CKM matrix can be expressed in the basis of the independent parameters $(\mathrm{A}, \lambda, \rho, \eta)$ through the Wolfenstein parametrization:

$$V_{ij} = \begin{pmatrix} V_{ud} & V_{us} & V_{ub} \\ V_{cd} & V_{cs} & V_{cb} \\ V_{td} & V_{ts} & V_{tb} \end{pmatrix} = \begin{pmatrix} 1 - \frac{1}{2}\lambda^2 & \lambda & \mathrm{A}\lambda^3\left(\rho - i\eta\right) \\ -\lambda & 1 - \frac{1}{2}\lambda^2 & \mathrm{A}\lambda^2 \\ \mathrm{A}\lambda^3\left(1 - \rho - i\eta\right) & -A\lambda^2 & 1 \end{pmatrix} + o\left(\lambda^4\right) \tag{1.4}$$

In this parametrization, the imaginary part η is connected with the complex phase δ, hence it gives rise to the $\mathcal{CP}$ violation in weak interactions. This parametrization highlights that transitions between quarks of the same generations are favored, indeed diagonal terms are close to 1, while transitions between quarks of different generations are suppressed, indeed off-diagonal terms are proportional to increasing powers of the small parameter λ, which corresponds to the sine of the Cabibbo angle.

CKM is a unitary matrix, i.e. $\Sigma_i V_{ij} V_{ik}{}^* = \mathbb{1}$. This property defines some relations between the CKM matrix elements: for example, the relation $V_{ud} V_{ud}{}^* + V_{us} V_{us}{}^* + V_{ub} V_{ub}{}^* = 1$ means that the total probability of transition of the quark u in a down-type quark is 1, while the relations $V_{ud} V_{ub}{}^* + V_{cd} V_{cb}{}^* + V_{td} V_{tb}{}^* = 0$ means that the quark d and the quark b are orthogonal states, hence a transition between them is not possible.
The relations defined by $\Sigma_{i,j \neq k} V_{ij} V_{ik}{}^* = 0$ can be represented through unitarity triangles. For example, the relation $V_{ud} V_{ub}{}^* + V_{cd} V_{cb}{}^* + V_{td} V_{tb}{}^* = 0$ can be represented by the unitarity triangle in the (ρ, η) plane shown in Figure 1.1.

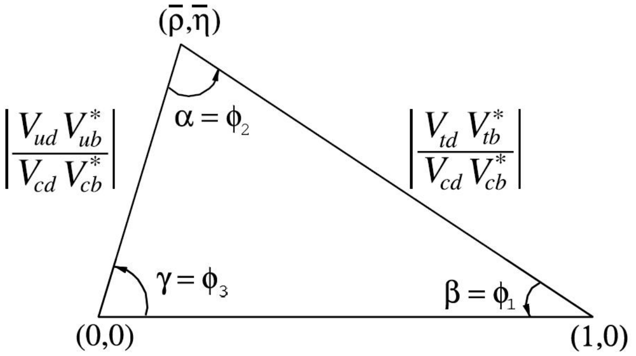

Figure 1.1: The unitarity triangle associated with the relation $V_{ud} V_{ub}{}^* + V_{cd} V_{cb}{}^* + V_{td} V_{tb}{}^* = 0$. The sides of the triangle have been normalized respect to the quantity $V_{cd} V_{cb}{}^*$. The top vertex of the triangle has coordinates $(\bar{\rho}, \bar{\eta})$, where $\bar{\rho} = \rho \left(1 - \lambda^2/2\right)$ and $\bar{\eta} = \eta \left(1 - \lambda^2/2\right)$. The angles α, β and γ are associated to the CKM matrix elements by the following relations: $\alpha = arg\left[\frac{V_{ud} V_{ub}{}^*}{V_{td} V_{tb}{}^*}\right]$, $\beta = arg\left[\frac{V_{td} V_{tb}{}^*}{V_{cd} V_{cb}{}^*}\right]$ and $\gamma = arg\left[\frac{V_{cd} V_{cb}{}^*}{V_{ud} V_{ub}{}^*}\right]$.

An overview of the most recent experimental limits on the unitarity triangle parameters are shown in Figure 1.2.

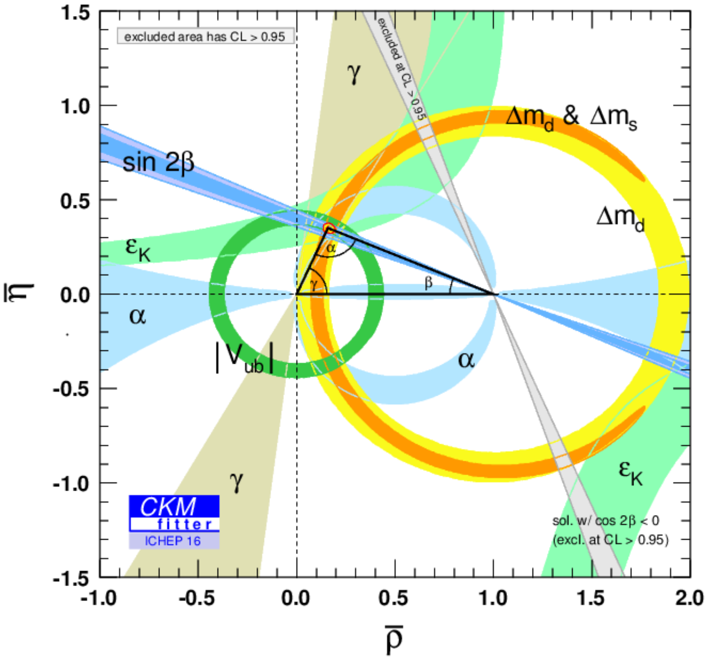

Figure 1.2: Constraints on the CKM matrix parameters in the $(\bar{\rho}, \bar{\eta})$ plane obtained from all the experimental measurements. The most probable position of the unitarity triangle vertex is into the red circle.

1.2 Introduction to Dark Matter

The first and most significant evidence of DM was attributed to the Austrian physicist F. Zwicky, who measured the rotational velocity of galaxies in the Coma cluster in 1933. Galaxies are composed of a spherical bulk of radius R_b, in the central region, and of a galactic disk of radius R_G. From the Newton's law, the rotational velocity v of an object rotating on a stable Keplerian orbit of radius r is $v(r) = \sqrt{M(r)G/r}$, where $M(r)$ is the mass of the galaxy contained inside the radius r. If $r \geq R_G$ then $M(r) = M_G$, where M_G is the mass of the galaxy, and $v(r) \propto r^{-1/2}$. The experimental measurement performed by Zwicky and confirmed by subsequent experiments shows that for $r > R_G$ the rotational velocity is $v(r) = \text{const}$, as shown in Figure 1.3, which suggests the presence of a *dark halo* with mass density of $\rho \propto 1/r^2$, i.e $M(r) \propto r$ [4].

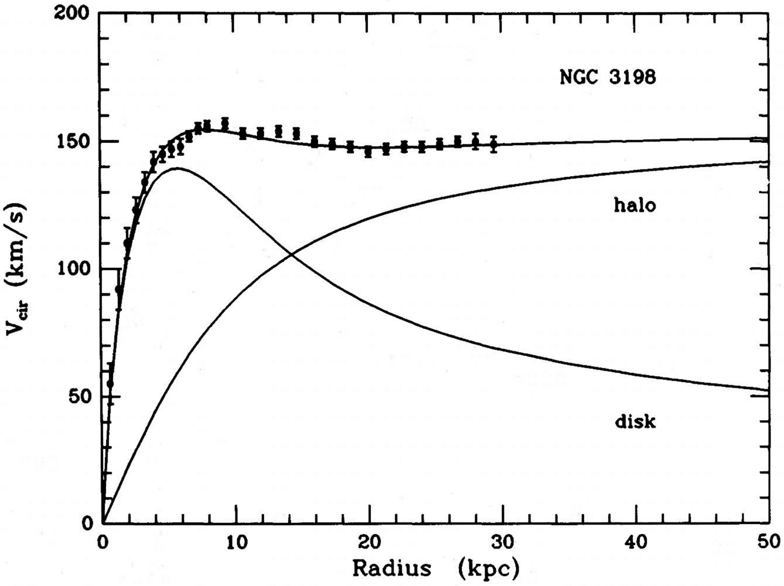

Figure 1.3: Rotational velocity curves of the NGC 3198 galaxy. Dots with error bars show the experimental data. *Halo* curve is based on a mass model assuming $a = 8.5$ kpc, $\gamma = 2.1$, $\rho(R_0) = 0.0040\ M_0\ \text{pc}^{-3}$: a is linked to the bulk radius, R_0 is the fiducial radius of the *halo*, γ is an appropriate parameter of the mass model and $\rho(R_0)$ is the mass density of the *halo*. The image was taken from the article by Albada *et al.* (1985) [5].

Other observations based on the mass distribution in the Universe, suggest the presence of DM in galaxies. For example: elliptical galaxies show evidence for DM through gravitational lensing effects; observations of X-rays from hot gas in hydrostatic equilibrium, filling the *dark halo* of elliptical galaxies, provides evidence of DM; the velocity dispersion of spiral galaxy satellites suggest the presence of *dark halos* characterized by radii ≥ 200 kpc; the velocity dispersion of dwarf spheroidal galaxies suggest the presence of higher mass compared to the mass of visible matter, and so on. Furthermore, some estimates of DM mass density in the Universe, consistent with the Big Bang cosmological model, are provided by precise measurements of the cosmological parameters through the study of *Cosmic Microwave Background Radiation* (CMBR) fluctuations [4].

The Cosmological Model is based on the *cosmological principle*, which assumes the Universe to be homogeneous and isotropic. The model is built on three fundamental ingredients: the Einstein equation, describing gravitation as an effect of the curvature of the space-time due to the presence of high masses; the metrics, associated with the symmetries of the space-time fabric; and the equation of state, which takes into account the properties of matter and energy [4, 6, 7].

From Einstein equation of gravitation, two equations of motion describing the expansion of the Universe can be derived, called Friedmann equations:

$$\begin{aligned} \frac{kc^2}{a^2} + H^2 = \frac{8G\pi\rho}{3} + \frac{\Lambda c^2}{3} \\ \frac{kc^2 + \dot{a}^2}{a^2} + \frac{2\ddot{a}}{a} = -\frac{8G\pi P}{c^2} + \frac{\Lambda c^2}{3} \end{aligned} \tag{1.5}$$

The G, Λ and c parameters are the universal constants: respectively, the gravitational constant, the cosmological constant and the speed of light in vacuum. The $a(t)$ parameter is the cosmological scale factor that describes the expansion of the Universe over time and it is assumed to be 1 at the present time. H is the Hubble parameter and it is defined in terms of the scale factor a as $H = \dot{a}/a$, so it is time dependent. The total mass density and the pressure of the matter that constitutes the Universe are expressed through ρ and P terms, which are components of the *stress-energy tensor* and are time dependent. The k parameter is the spatial curvature. In the second equation, if $\Lambda = 0$ than $\ddot{a} < 0$, which means that the Universe decelerates. Experimental observations show that the expansion of the Universe is accelerated, for this reason the $\Lambda > 0$ term is necessary [8].

The Einstein equation describes the curvature of the space-time in terms of the mass, the energy and the pressure that are represented through the *stress-energy tensor*, which is the source of the gravitational field in the equation. The equations of motion can be obtained by choosing an appropriate system described by a simple *stress-energy tensor*, in order to obtain a good approximate model of the evolution of the Universe. The Friedmann equations are obtained for the *stress-energy tensor* for a perfect fluid, assuming the *cosmological principle*, of homogeneity and isotropy of the fluid [6, 8, 9]. Finally, in order to obtain the equations it is necessary to choose the metric that describes the geometry of the system. The Friedmann equations are derived assuming the Roberson-Walker metric that is compatible with the *cosmological principle* and with a uniform expansion of the Universe, according to Hubble's observations [9].

One of the fundamental cosmological parameter is the *critical density* that expresses the Universe mass density value discriminating between closed and open Universe. Introducing the definition of the *critical density* for a flat Universe ($k = 0$) $\rho_c = 3H_0^2/8\pi G \approx 5 \cdot 10^{-30}\mathrm{gcm}^3$, where $H_0 \approx 70$ km/sMpc is the Hubble constant measured at the current time, the first of Friedmann equation can be used to derive very important properties related to the evolution of the Universe in terms of the Ω density parameters as $\Omega_M + \Omega_k + \Omega_\Lambda = 1$: $\Omega_M = \rho/\rho_c$ is the contribution of the matter, with ρ the total mass density of the matter (baryonic plus relativistic) in the Universe, $\Omega_k = -kc^2/(a^2H^2)$ is the contribution of the curvature, with H the Hubble constant, and $\Omega_\Lambda = \Lambda c^2/(3H^2)$ is the contribution of the cosmological constant [4, 8].

Very precise experimental measurements of CMBR anisotropies indicates that current values of Ω parameters are $\Omega_{0,M} \approx 0.3$, $\Omega_{0,\Lambda} \approx 0.7$ and $\Omega_{0,k} = 0$. The $\Omega_{0,M}$ parameter contains both contributions from relativistic matter and non-relativistic matter, although the contribution from the relativistic matter is negligible. These values suggest a flat Universe in accelerated expansion, in which around the 70% of the Universe is due to an unknown form of energy called *dark energy*: Ω_Λ expresses the effective density of the dark energy in the Universe. From a detailed analysis of CMBR temperature anisotropies and

Big Bang Nucleosynthesis (BBNS) models, the baryonic matter density is estimated to be $\Omega_{0,bar} \approx 0.05$. This means that DM contributes for the 25% to the total energy density of the Universe and for more than the 80% to the total matter of the Universe, while the ordinary matter contributes only for the 20% to the matter of the Universe and for around the 5% to the total energy density of the Universe [4, 10].

It has been hypothesized, until recently, that neutrinos could be good DM candidates and could explain the abundance of DM in the Universe. However, from the density of neutrinos in the Universe, which is around 400 cm^{-3}, and imposing $\Omega_{DM} = \Omega_\nu = \rho_\nu/\rho_c = 0.25$, the neutrino mass should be $m_\nu \approx 5\ \mathrm{eV}/c^2$, which is excluded from experimental measurement. For example, the tritium β-decay experiment has set the upper limit on neutrino mass at $m_\nu < 2.05\ \mathrm{eV}/c^2$ with 95% CL [11], while future experiments are expected to have a sensitivity on neutrino mass around 0.2 eV/c^2. The *relic density* of neutrinos is estimated to be $\Omega_\nu \approx 0.07$ and further constraints on Ω_ν come from analysis on CMBR anisotropies. For this reason neutrinos are not enough abundant to be the dominant part of DM [4].

A simple explanation for most of the cosmological phenomena is provided by the hypothesis of *Cold Dark Matter* (CDM) that consists of non-relativistic massive particles. Three possible candidates of CDM are Axions, *Massive Compact Halo Objects* (MACHOs) and *Weakly Interactive Massive Particles* (WIMPs).

Axions These DM candidates have been introduced in QCD in order to solve the problem of $\mathcal{CP}$ violation in strong interaction, called *Strong* $\mathcal{CP}$ *Problem* [12]. Astrophysical constraints on the mass of axions come from stellar cooling and dynamics of supernovae that force axions to have a mass $\leq 0.01\ \mathrm{eV}/c^2$ [4]. Furthermore, they are expected to be very weakly interacting, for this reason they could not be in thermal equilibrium in the early Universe. Despite constraints, some several theoretical models predict that axions could be good DM candidates [4].

MACHOs These DM candidates are very large and condensed objects, as black holes, neutron stars, planets, brown dwarfs and white dwarfs, that are in the *halo*. Experiments, which exploits gravitational lensing effect due to the transit of these objects, confirm the existence of MACHOs, but their mass is much lower with respect to DM mass in *halos* [13, 14].

WIMPs They are massive particles that interact with a self-annihilation cross section of $\sim 3 \cdot 10^{-36}\ \mathrm{cm}^2$. A non-relativistic particle that interacts weakly comes out from thermal equilibrium since its annihilation rate differs from its production rate. This can occur for two reasons in particular: lighter particles have not sufficient kinetic energy to produce heavier particles through interactions, and the rate of expansion of the Universe becomes higher than the interaction rate. At a certain time, the numerical density of heavier particles of a particular species becomes too small and those particles can't interact anymore, so the conditions of thermal equilibrium fail. This particular process is called *freeze-out* and the density of those heavier particles, since it does not change anymore, is called *relic density*. The Boltzmann equation describes the coming out of particles from thermal equilibrium [15], in terms of the numerical density normalized to the entropy density of the particle system, Y. Figure 1.4 shows the *freeze-out* of a massive particle species derived by the Boltzmann equation.

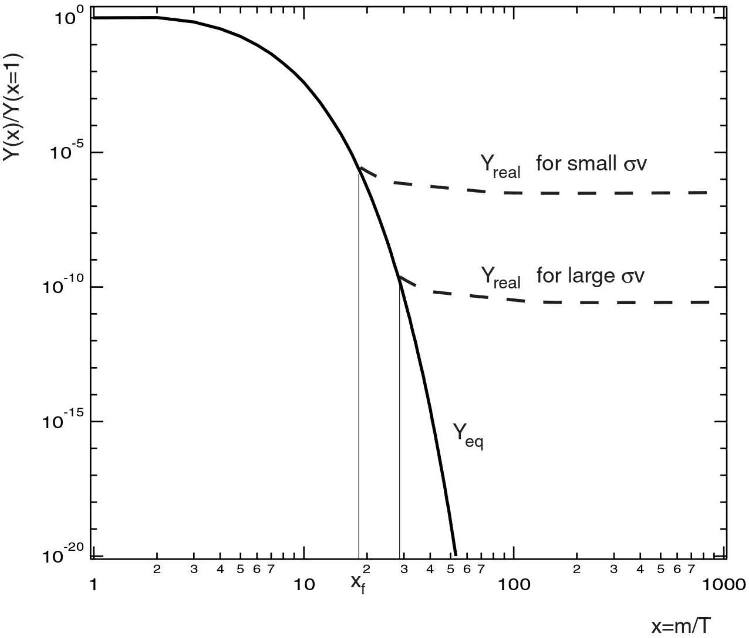

Figure 1.4: The *freeze-out* of a massive particle species derived from the Boltzmann equation. The variable $Y(x)$ is the numerical density of a particular particle species χ normalized to the entropy density s of the particle system in a volume a^3, where a is the scale factor of the Universe. The x_f parameter is defined as $x_f = m_\chi/T_f$, where m is the mass of the χ particles and T_f is the temperature at the *freeze-out*. The solid line is the value of Y at thermal equilibrium, Y_{eq}. For a certain value of x_f, χ particles leave the thermal equilibrium, Y becomes constant (dashed lines) and it represents the current abundance, Y_{real}. In the graph is shown the ratio $Y(x)/Y(x=1)$ as a function of x. At higher values of the annihilation rate σv, corresponds a smaller relic abundance. For WIMPs $x_f \approx 20$. The graph is taken from [7].

The *relic density* is inversally proportional to the annihilation rate. Assuming $x = m/T \approx 20$, where m is the mass of the DM particle and T is the temperature at the *freeze-out*, and $\Omega_{0,DM} = 0.3$, a cross section of $\sigma \simeq 3 \cdot 10^{-36}$ cm^2, which is a typical cross section of weak interaction, is obtained for WIMPS. Assuming WIMPs interacting *via* weak interaction, a mass of the magnitude of the TeV$/c^2$ is estimated. *Supersymmetric* (SUSY) extensions of the SM predict new particles with the same characteristics of WIMPs: this is known as *WIMP Miracle* [16].

The limit to the minimum mass of WIMPs was calulated by B. Lee and S. Weinberg: it results of few GeV$/c^2$, assuming the annihilation cross section of weak interaction [4]. However, if DM consists of a different kind of particles, the limit of Lee-Weinberg can be avoided and DM particles with a mass below the GeV scale has been proposed. DM characterized by sub-GeV$/c^2$ mass is called *Light Dark Matter* (LDM) and it is well motivated by several theoretical models [4, 17, 18, 19, 20, 21].
Experiments sensitive to WIMPs with masses in the range GeV$/c^2$-TeV$/c^2$ have not found interesting signals yet, for this reason theoretically well-motivated models that introduce LDM candidates with a mass in the range keV$/c^2$-GeV$/c^2$ and consistent with the observed history of the Universe have been developed. LDM particles could be part of a *dark sector* that could interact with SM particles through a mediator that is charged under both sectors, SM and *dark sector*.

1.2.1 Motivations for LDM

Several mechanisms for DM production suggest the existence of DM with masses in the range keV/c^2-GeV/c^2. Limits on DM mass depends on the DM production mechanism: the *freeze-out*, already described in Section 1.2, admits sub-GeV/c^2 LDM, assuming that DM is part of a wider *dark sector* that also include mediators of interactions. However, other mechanisms are possible, and some of them are briefly introduced in the following [22].

- Asymmetric DM scenario: as known, in the Universe there is an asymmetry between SM baryons and anti-baryons that can explain the relic abundance of baryons. The asymmetric DM scenario assumes a DM particles/anti-particles asymmetry that determines the DM relic abundance, similar to the baryon/anti-baryon asymmetry that can explains the relic abundance of baryons. The precise mechanism is unknown, but masses in the range keV/c^2-GeV/c^2 could be possible [23].

- The *freeze-in* DM production mechanism assumes that DM was not in thermal equilibrium with SM particles. However, because of the very small interactions between DM and ordinary matter, SM particles annihilated or decayed in DM particles very slowly: this mechanism can explain the DM relic abundance. Experiments could investigate the space of parameters of some LDM models that assume the *freeze-in* mechanism [24].

- In the *Strongly Interacting Massive Particles* (SIMP) model, the DM relic abundance is set by the *freeze-out* mechanism characterized by number-changing $3 \to 2$ annihilation processes of strongly interacting particles. This annihilation process consists of three particles of DM that collides producing two DM particles. In SIMP model DM particles with sub-GeV/c^2 masses arise naturally assuming sizeable coupling constants [25].

- A variation of SIMP model assumes that DM relic abundance is set by cross section of elastic collisions between DM particles and SM particles, instead of $3 \to 2$ annihilation processes. This model is called *Elastically Decoupling Relic* and DM particles with masses of few MeV/c^2 arise naturally, [26].

Finally, further good LDM candidates could be the QCD axions [12] and the *dark photon* that mediates interactions between DM particles and SM particles. Both are introduced in the next sections.

Annihilation of LDM, with masses of few MeV/c^2, can produce e^+e^- pairs that can be the origin of the 511 keV signal observed by the INTEGRAL experiment [27] and of the excess of positrons observed by PAMELA, FERMI and AMS, discussed below.

1.2.2 Detection of DM

Experiments on the detection of DM can be divided into two groups: *Direct detection* experiments and *Indirect detection* experiments. The former search for the scattering of DM particles on ordinary matter particles, the latter searches for products of annihilation or decay of DM in SM particles.

Direct detection experiments are based on the idea that our galaxy is filled with steady WIMPs. Several WIMPs should cross the Earth, because of the motion of the solar system. This kind of experiments search for low-energy signals due to the recoil of nuclei, after the interaction between WIMPs and nuclei. After the recoil, the nucleus emits scintillation photons that can be detected with an appropriate detection system. Furthermore, because of the motion of the Earth around the Sun, the signal due to the recoil of nuclei should be modulated with a period of one year. The sensitivity of *Direct detection* experiments depends on the cross section of WIMP-nuclei interaction, and on the density and the velocity distributions of WIMPs in the galaxy, [4]. Many experiments searching for WIMP-nuclei interactions exist: DAMA experiment, located at INFN laboratories under the Gran Sasso, claims the discovery of WIMPs because it observes an annual modulation of the signal consistent with the detection of a WIMP with a mass of 60 GeV/c^2 and a WIMP-nuclei scattering cross section of $\sim 10^{-41}$ cm^2 [28]. The DAMA experiment results have not been confirmed by other experiments yet.

Indirect detection experiments search for the products of annihilation or decay of DM particles. In regions of the space in which there is high density of DM particles, they can annihilate producing SM particle pairs, otherwise DM particles could be unstable and decay in SM particles that can be detected. The annihilation rate depends on the density of DM particles squared, [4]. Some important results in *Indirect detection* have been provided by PAMELA, FERMI and AMS experiments. PAMELA experiment measured the fraction of positrons in cosmic rays (CR), $\phi(e^+)/(\phi(e^+) + \phi(e^-))$, observing that it increases with energies in the range 1.5-100 GeV, [29]. Antiparticles are a small fraction of cosmic rays and they are expected to be produced in interaction between CR nuclei and atoms in interstellar medium. Antiparticles can be produced also in pulsars, microquasars or by annihilation of DM particles. The interaction of CR nuclei with interstellar gas produce charged pions that decay in positrons and neutrinos, but the production of positrons from pion decays is in tension with PAMELA results. Understanding the excess of positrons is not simple because it requires a reliable model of positron production by pulsars or other astronomical objects. A recent measure of the positron flux on Earth confirm pulsars as a source of positrons but may exclude pulsars as the origin of the excess of positrons in CR [30].

FERMI experiment measured the excess of positrons in CR with energies in the range 20-200 GeV, confirming PAMELA measurement [31]. At the same way, AMS experiment confirmed what observed by PAMELA and FERMI up to 500 GeV, observing also a tendency to decrease around 350 GeV [32].

A different approach is the production and detection of DM particles in colliders, indeed if the interaction of DM with SM particles occurs, it may be possible produce DM particles at colliders. Because DM particles have negligible interactions with ordinary matter, they may be detected as missing energy. Many constraints on DM candidates from collider experiments exist and they will be discussed in section1.4.

1.3 Extensions of the Standard Model

Although the SM is a very successful theory in describing the visible matter, it does not contain an explanation of DM and nor of dark energy. Furthermore, it does not con-

tain a description of gravity: there are some attempts to reconcile general relativity with quantum mechanics in order to include the gravity within the SM, but currently does not exist a reliable theory able to do it.
The violation of the $\mathcal{CP}$ symmetry is a necessary condition for the baryon/anti-baryon asymmetry that allows a dominated-matter evolution of the Universe. However, the complex phase responsible for $\mathcal{CP}$ violation in the SM is orders of magnitude too small to explain the baryon/anti-baryon asymmetry. The SM does not contain an appropriate explanation for baryon/anti-baryon asymmetry.
The SM is very predictive about physics processes but currently it has 19 arbitrary parameters that must be measured in experiments. In order to include neutrino masses and neutrino oscillation in the SM, which do not explain their details, 9 more arbitrary parameters (three masses, three phases and three angles) are needed.
Another problem that arises in the SM is known as hierarchy problem. It is related to the difference between the gravitational interaction magnitude and the weak interaction magnitude, which is 10^{24} times stronger than the gravitational interaction. In the context of particle physics, this problem is related to the Higgs mechanism. Indeed the strength of the weak interaction is related to the Higgs boson mass, which is much smaller than Planck Mass. This is not expected since both are related to nature constants: the weak interaction strength is related to the Fermi constant and gravitational strength is related to the Newton constant [1]. These limitations of the SM indicate the existence of additional physics, referred to as *Physics Beyond the Standard Model*, that could be detected experimentally through precision measurements.
Different tensions between the experimental measurements and the theoretical predictions of the SM have been observed and some examples of them are reported in the following.

The $(g-2)_\mu$ anomaly The experimental value of the anomalous magnetic moment of the muon $a_\mu = (g-2)_\mu/2$, where g is the gyromagnetic factor, deviates from the theoretical prediction of about 3.2σ.
The experimental measurement a_μ^{exp}, the theoretical prediction a_μ^{SM} and the deviation between the two quantities δa_μ are reported in table 1.3 [33].

	Value($\cdot 10^{-11}$)	Error($\cdot 10^{-11}$)
a_μ^{exp}	116592080	63
$a_\mu^{SM} = a_\mu^{QED} + a_\mu^{EW} + a_\mu^{QCD}$	116591790	65
$\delta a_\mu = a_\mu^{SM} - a_\mu^{exp}$	290	90

Table 1.3: The *Brookhaven National Laboratories* (BNL) $(g-2)$ experiment reduce the experimental uncertainty on the measure of a_μ^{exp} to $\sim 63 \cdot 10^{-11}$. a_μ^{exp} is the average world experimental value and it is dominated by the BNL measure. The theoretical prediction includes three contributions: QED lepton and photon loops, EW $W^\pm$, Z^0 bosons and the Higgs boson loops and QCD hadron loops.

The anomalous magnetic moment of the muon is one of the most precise tests of QED and EW theory but it is also sensitive to new physics. The deviation δa_μ could be a hint of new physics.

Lepton Flavor Universality In the SM the coupling of EW gauge bosons with charged leptons is equal for all charged leptons: this property is called Lepton Flavour Universality (LFU). Tests of LFU are sensitive to new physics models that violate LFU.
Rare B meson decays with flavour transitions as $b \to sll$ are particularly sensitive to new physics because they are suppressed in the SM, hence effects of new physics might be observable.
Some deviations from SM predictions in B meson semileptonic decays recently measured by LHCb are shown in Table 1.4 [34].

LHCb LFU tests	Deviation from SM
$R_K = Br(B^+ \to K^+\mu^+\mu^-)/Br(B^+ \to K^+e^+e^-)$	2.6σ
$R_{K^*} = Br(B^0 \to K^{*0}\mu^+\mu^-)/Br(B^0 \to K^{*0}e^+e^-)$	2.1-2.5σ [1]
$R_{D^*} = Br(\bar{B}^0 \to D^{0*}\tau^-\bar{\nu}_\tau)/Br(\bar{B}^0 \to D^{0*}\mu^-\bar{\nu}_\mu)$	2.1σ
$R_{J/\psi} = Br(B^+ \to J/\psi\tau^+\nu_\tau)/Br(B^+ \to J/\psi\mu^+\nu_\mu)$	2σ

Table 1.4: Measurements of the $B.R.$ of semi-leptonic B-meson decays from LHCb, in tension with SM predictions.

When combined with the measurements of R_{D^*} and $R_D = Br(\bar{B}^0 \to D^0\tau^-\bar{\nu}_\tau)/Br(\bar{B}^0 \to D^0\mu^-\bar{\nu}_\mu)$ previously made by the *BABAR* and *Belle* collaborations, it results in a tension with SM prediction of 4.1σ as shown in Figure 1.5 [34].

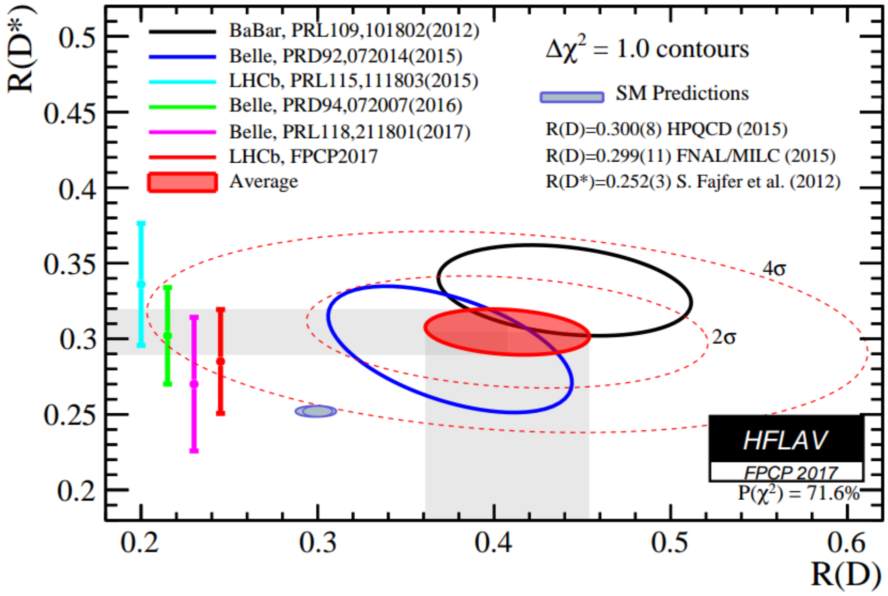

Figure 1.5: The red region in the middle of the graph is the result of the combination of the R_{D^*} measurements from LHCb and the R_{D*} and R_D measurements from *BABAR* and *Belle*. The light blue region at $(R_D, R_{D^*}) \sim (0.3, 0.25)$ is the SM prediction.

---

[1] Depending on the region of $m^2(ll)$ in which the measure is made. $m^2(ll)$ is the square of the invariant mass of the two leptons in the final state.

In order to try to explain what currently is not explained by SM, a possibility to include new physics in the SM is the *dark sector*. It defines a new group of particles that interacts with ordinary matter, although very weakly, and that could mediate a new interaction between SM particles and DM. Usually, light gauge bosons that mediate interactions between SM and DM particles are referred to as *dark photons*. The *dark sector* is well motivated by the theoretical point of view and some clues of its presence are suggested by the deviations between the SM predictions and the experimental results. The extensions of the SM provide new gauge symmetries that predict the existence of new light gauge bosons interacting with SM particles. The coupling between *dark sector* particles and the SM particles would allow *dark sector* particles to be detected in particle physics experiments and to explain astrophysical and cosmological observations.
The *dark sector* include new mediators coupled with SM through different *portals* depending on the spin and the parity of the mediator itself. The *portals* are limited by requiring gauge and Lorentz symmetries of the Lagrangian: possible *portals* are listed in the following [22].

The Vector Portal $\mathcal{L} \supset -\frac{\epsilon}{2} B_{\mu\nu} F'^{\mu\nu}$, where $B_{\mu\nu} = \partial_\mu B_\nu - \partial_\nu B_\mu$ is the tensor field of $U(1)_Y$ and $F'^{\mu\nu} = \partial^\mu A'^\nu - \partial^\nu A'^\mu$ is the tensor field of an additional $U'(1)$ that extends the gauge group of the SM. The A' field represents the vector mediator introduced by the vector portal through the *kinetic mixing* interaction term $\sim \epsilon B_{\mu\nu} F'^{\mu\nu}$, where ϵ is the *kinetic mixing* strength. The ϵ *kinetic mixing* strength is a free parameter and it can take any value because of the renormalizability of the theory, it is not required to be small. Anyway it is expected to be small, $\epsilon \lesssim 10^{-3}$, since it arises from loops of heavy states which are charged under both $U'(1)$ and $U(1)_Y$. For this reason the vector portal may provide the dominant interaction between the SM and the *dark sector* [22, 35]. The vector *portal* introduce a phenomenology that is present in several theoretically well motivated *dark sector* models and it predicts couplings between the the vector mediator boson and the DM candidates.

The Higgs Portal $\mathcal{L} \supset (\mu\phi + \lambda\phi^2) H^\dagger H$, where ϕ is the *dark sector* scalar mediator that interacts with the SM Higgs boson H and μ and λ are appropriate parameters. If the new *dark sector* mediator is scalar, it can interact with SM particles through the Higgs portal. This kind of mediator can be investigated at LHC by studying the rare decays of the Higgs boson. If the scalar ϕ is assumed to be a sub-GeV particle, several constraints already exist, see for example the Reference [36].

The Axion Portal $\mathcal{L} \supset \frac{a}{f_a} F_{\mu\nu} \tilde{F^{\mu\nu}}$, where $F_{\mu\nu} = \partial_\mu A_\nu - \partial_\nu A_\mu$ is the tensor field of the SM photon, $\tilde{F_{\mu\nu}}$ is the dual tensor field of $F_{\mu\nu}$ and a is the *dark sector* pseudoscalar mediator. The axion *portal* is suppressed by the mass scale f_a. The *dark sector* pseudoscalar mediator can be the axion, which is a pseudoscalar particle introduced by R. Peccei and H. Quinn to solve the *strong $\mathcal{CP}$ problem*. The idea of Peccei and Quinn is to extend the QCD Lagrangian with a term that violates the $\mathcal{CP}$ symmetry. This additional term is explained through a dynamic field associated to the axion and after the spontaneous symmetry breaking it becomes naturally zero, according with experimental observations of preserved $\mathcal{CP}$ symmetry in strong interactions. The axion portal is suppressed by the axion decay constant f_a that determines the strength of the spontaneous Peccei-Quinn symmetry breaking [37]. The *Axion-like-particles* (ALPs) are a generalized form of the axion [38].

The Neutrino Portal $\mathcal{L} \supset y_n LHN$, where y_n is a Yukawa coupling, N is a fermionic mediator that belongs to the *dark sector*, H is the SM Higgs boson and L is a lepton doublet of $SU(2)$. The neutrino *portal* introduces the *dark sector* mediator N, which is a fermionic mediator analogous to a right-handed neutrino with a Yukawa coupling y_n. For the mediator N with mass in the range MeV/c^2-GeV/c^2, several experimental constraints exist, see Reference [39] for details.

In the following a minimal kinetically-mixed *dark photon* model will be introduced in order to explain the vector *portal* and the *kinetic mixing* mechanism [40, 41]. Considering a model with a gauge symmetry with respect to the group $U(1) \otimes U'(1)$, the *kinetic mixing* term can be naturally introduced in the Lagrangian. The *kinetic mixing* process can only take place between two abelian gauge groups since the resulting mixing term is gauge invariant under the symmetry $U(1) \otimes U'(x)$, indeed the individual tensor fields are gauge invariant under the respective gauge group. The introduction of the *kinetic mixing* term makes the ordinary kinetic term no more diagonal, see the effective Lagrangian in Equation 1.6, where $B_{\mu\nu} = \partial_\mu B_\nu - \partial_\nu B_\mu$ is the tensor field associated to $U(1)$, $X_{\mu\nu} = \partial_\mu X_\nu - \partial_\nu X_\mu$ is the tensor field associated to $U'(1)$ and ϵ is the *kinetic mixing* strength.

$$\mathcal{L}_{eff} \supset -\frac{1}{4}B_{\mu\nu}B^{\mu\nu} - \frac{1}{4}X_{\mu\nu}X^{\mu\nu} - \frac{\epsilon}{2}B_{\mu\nu}X^{\mu\nu} \tag{1.6}$$

It is easy to verify that by redefining B_μ as $B_\mu \to B_\mu - \epsilon X_\mu$ and by considering the $\mathcal{O}(\epsilon)$ order, the kinetic term returns to be in its canonical form. After the redefinition of the gauge field, the interaction term $g\bar{\psi}\gamma^\mu B_\mu \psi$ becomes $g\bar{\psi}\gamma^\mu(B_\mu - \epsilon X_\mu)\psi$ and the additional interaction term $-g\epsilon\bar{\psi}\gamma^\mu X_\mu \psi$ between the $-g\bar{\psi}\gamma^\mu\psi$ current and the field X_μ arises in the theory.

When $U(1) = U(1)_Y$ then $B_{\mu\nu}$ is the tensor field associated with the hypercharge gauge group and after electroweak symmetry breaking, an analougus *kinetic mixing* term between the SM photon and the *dark photon*, i.e. $\epsilon/2F_{\mu\nu}F'^{\mu\nu}$, is obtained. The *kinetic mixing* matrix can be diagonalized and renormalized by redefining the fields and the physics gauge fields are those for which the kinetic term assumes its canonical form. The result of this operations is that the *dark photon* gauge field A'_μ acquires a coupling ϵe with the electromagnetic current, so the additional interaction term that arises in the theory is $\epsilon e J^\mu_{em} A'_\mu$, which makes explicit the coupling between the SM and the *dark sector* particles. Figure 1.6 shows a representation of the *kinetic mixing* mechanism between the *dark sector* fermions ϕ charged only under $U'(1)$, the SM fermions φ charged only under $U(1)_{e.m.}$ and the mechanism is mediated by some virtual heavy particles Φ charged under both groups [41] [40]. The symmetry $U'(1)$ can be broken spontaneously by a *dark Higgs* mechanism that gives mass to the *dark photon*. The *dark Higgs* boson has a renormalizable coupling with the SM Higgs boson giving rise to a mixing between the *dark Higgs* boson and the SM Higgs boson. A massive *dark photon* can solve the problem of the a_μ anomaly, the other observed deviations from the SM predictions and can explain various DM models [35].
The existence of DM is the main reason to introduce a *dark sector* and an extension of the minimal kinetically mixed *dark photon* including a DM candidate can be taken into consideration. If the DM candidate is for example a fermion χ the interaction term of the

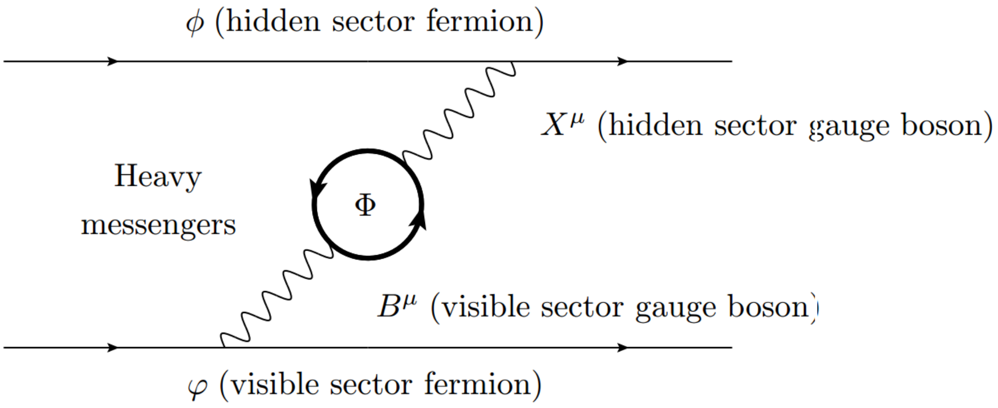

Figure 1.6: Effective interaction between *dark sector* fermions and SM fermions due to *kinetic mixing* between a dark gauge boson X_μ and a visible gauge boson B_μ at first loop order mediated by some heavy messengers Φ. Image taken from [41].

Lagrangian is $\mathcal{L} = \bar{\chi}(i\gamma^\mu D_\mu - m_\chi)\chi$ where $D_\mu \equiv \partial_\mu - ig' A'_\mu$, g' is the *dark sector* coupling and A'_μ is the field associated to the *dark photon*. Theoretically the DM could interact with the SM matter if a *dark photon*, which mediates the interaction between DM and SM particles, exists.

Also more complex extensions of the SM have been developed in order to explain DM and fill in the shortcomings of the SM. Among the other theories, one of the most relevant is the SUSY theory [42], which predicts two bosonic partners for each SM fermion and two fermionic partners for each SM boson. The minimal model that introduces SUSY in the SM is the extension called *Minimal Supersymmetric Standard Model* (MSSM) [43], which needs of two Higgs doublet more than the SM Higgs boson and consequently different *two-Higgs-doublet* models have been developed [44].

1.3.1 $L_\mu - L_\tau$ Model

The $L_\mu - L_\tau$ model introduces a new gauge boson Z' extending the SM gauge group $G_{SM} = U(1)_Y \otimes SU(2)_L \otimes SU(3)_C$, with an additional abelian gauge group $U(1)_{L_\mu - L_\tau}$. This extension is anomaly-free and provides an additional global symmetry that preserves the difference between the μ-leptonic number and the τ-leptonic number in processes. The particle content of the SM allows to gauge three differences between the leptonic numbers, $L_e - L_\mu$, $L_\mu - L_\tau$ and $L_e - L_\tau$, that are anomaly-free. However, the $L_\mu - L_\tau$ is preferred with respect to other ones since it predicts a degenerate neutrino pair in the limit of preserved symmetry. After breaking the symmetry $U(1)_Y \otimes SU(2)_L \otimes U(1)_{L_\mu - L_\tau} \to U(1)_{e.m.}$, the degenerate neutrino pair will be split generating a small deviation from the $\mu - \tau$ symmetry, that could explain experimental data. On the contrary, the $L_e - L_\tau$ and $L_e - L_\mu$ models predict a neutrino mass matrix, in the limit of preserved symmetry, that is far away from that necessary to reproduce the experimental results [45].

The extension $G = U(1)_Y \otimes U(1)_{L_\mu - L_\tau} \otimes SU(2)_L \otimes SU(3)_C$ leads to a kinetic mixing between $U(1)_Y$ and $U(1)_{L_\mu - L_\tau}$, i.e. to an additional gauge-invariant term $\sim B_{\mu\nu} Z'^{\mu\nu}$ in the Lagrangian density. The Lagrangian density takes the form $\mathcal{L} = \mathcal{L}_{SM} + \mathcal{L}_{Z'} + \mathcal{L}_{mix}$, where $\mathcal{L}_{SM}$ is the SM Lagrangian reported in Equation 1.1, and the other terms are in the following equation [45]:

$$\begin{aligned}
\mathcal{L}_{mix} &= -\frac{\epsilon}{2}B_{\mu\nu}Z'^{\mu\nu} \\
\mathcal{L}_{Z'} &= -\frac{1}{4}Z'_{\mu\nu}Z'^{\mu\nu} + \frac{1}{2}M_{Z'}^2 Z'_{\mu\nu}Z'^{\mu\nu} - g'j'^{\mu}Z'_{\mu} \\
j'^{\mu} &= \bar{\mu}\gamma^{\mu}\mu + \bar{\nu}_{\mu}\gamma^{\mu}\nu_{\mu} - \bar{\tau}\gamma^{\mu}\tau - \bar{\nu}_{\tau}\gamma^{\mu}\nu_{\tau}
\end{aligned} \tag{1.7}$$

The tensor field $Z'_{\mu\nu} = \partial_\mu Z'_\nu - \partial_\nu Z'_\mu$ is associated to $U(1)_{L_\mu - L_\tau}$ while $B_{\mu\nu} = \partial_\mu B_\nu - \partial_\nu B_\mu$ is the tensor field associated to the SM $U(1)_Y$.
The field Z'_μ is associated to the new gauge boson Z', mediator of the interaction between the SM and the *dark sector*. The ϵ parameter represents the kinetic mixing strength between $U(1)_Y$ and $U(1)_{L_\mu - L_\tau}$, while g' is the coupling constant associated to the new gauge boson. The j'^{μ} current is associate to the symmetry due to the additional gauge group. The μ, τ and ν fields are associated respectively to muons, tauons and neutrinos, where the subscript of the ν fields indicates the flavour of the neutrinos. Finally the γ^μ are the Dirac gamma matrices.

The particular symmetry ensures that the new gauge boson, Z', interacts only with tauons and muons and their neutrinos through the interaction term $-g'j^{\mu}Z'_{\mu}$, where j'^{μ} is the interaction current.

The interaction term predict a coupling between the Z', muonic and tauonic charged leptons and neutrinos, for this reason Z' could decay visibly in a lepton pair or invisibly in a neutrino pair. The decay widths in neutrinos and leptons predicted by the model are shown in Equation 1.8, where $l = \{\mu, \tau\}$ [46], $M_{Z'}$ is the Z' mass and m_l is the lepton mass.

$$\begin{aligned}
\Gamma_{Z' \to l^+ l^-} &= \frac{g'^2 M_{Z'}^2}{12\pi}\left(1 + \frac{2m_l^2}{M_{Z'}^2}\sqrt{1 - \frac{4m_l^2}{M_{Z'}^2}}\right) \\
\Gamma_{Z' \to \nu\bar{\nu}} &= \frac{g'^2 M_{Z'}^2}{12\pi}
\end{aligned} \tag{1.8}$$

The model is theoretically well motivated: it could explain the a_μ anomaly in a region of the space of parameters that is not excluded yet by other models tested by the BABAR, Borexino and CCFR experiments [46]. The model can also explain the disagreement between the angular distributions of the final state particles in the rare decay $B \to K^* \mu^+ \mu^-$ observed by the LHCb experiment and the SM theoretical prediction [47]. The $L_\mu - L_\tau$ model is one of those models that, introducing a light mediator, could explain: the discrepancy observed in the measurements of e^+e^- pairs produced in ^{8}Be transitions from an excited state to the ground state [48], the deficit of high energy neutrinos in cosmic rays observed by the IceCube experiment [49, 50], the EDGES collaboration observations in the absorption spectrum about the 21-cm signal due to hydrogen transitions in the interstellar medium, which appears anomalously stronger than expected [51], the excess of positron in cosmic rays observed by the PAMELA, FERMI and AMS experiment. [29, 31, 46, 52, 53].

At colliders, a light Z' boson can be produced in association with a charged lepton pair: figure 1.7 shows Feynman diagrams of some possible detection processes that can be investigated in order to put constraints on the $L_\mu - L_\tau$ model.

Another possibility is to investigate the processes in which the Z' decays in an invisible final state, $Z' \to$ Invisible. The author of Reference [46] studied the possibility to detect

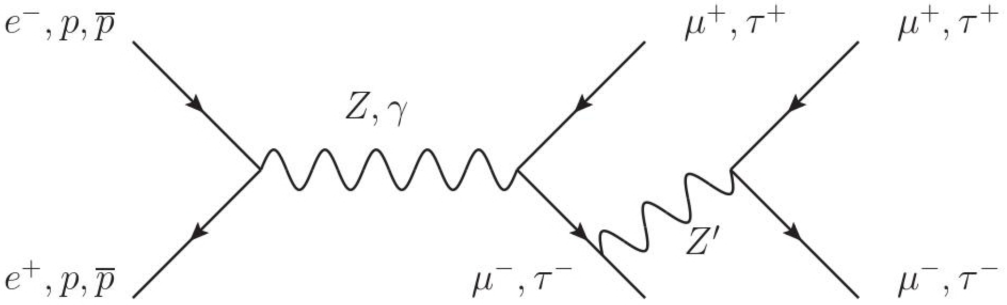

Figure 1.7: Detection process of Z' produced in association with a μ or τ pair in electron-positron or in proton-proton colliders. Image taken from [45].

Z' boson at *Belle*II anlyzing the process $e^+e^- \to \gamma Z', (Z' \to \nu\bar{\nu})$, where the Z' is produced *via* kinetic mixing with the ordinary photon[2]. The photon energy calculated in the center of mass frame $E_\gamma = (s - M_{Z'}^2)/2\sqrt{s}$ shows that the distribution of the photon energy is limited by the mass of the Z'. The production rate of the Z' is obtained multiplying the cross section $\sigma_{e^+e^- \to \gamma Z'}$ by the branching ratio of $Z' \to \nu\bar{\nu}$, shown in Table 1.5, [46].

$$\begin{array}{lccc}
B.R.(\Gamma \to \nu\bar{\nu}) = & \frac{\Gamma(Z' \to \nu\bar{\nu})}{\Gamma(Z' \to \nu\bar{\nu}) + \sum\limits_{l=\mu,\tau} \Gamma(Z' \to ll)} & \text{if} & M_{Z'} > 2m_\tau \\
B.R.(\Gamma \to \nu\bar{\nu}) = & \frac{\Gamma(Z' \to \nu\bar{\nu})}{\Gamma(Z' \to \nu\bar{\nu}) + \Gamma(Z' \to \mu\mu)} & \text{if} & 2m_\mu < M_{Z'} < 2m_\tau \\
B.R.(\Gamma \to \nu\bar{\nu}) = & 1 & \text{if} & M_{Z'} < 2m_\mu
\end{array}$$

Table 1.5: Branching ratios of Z' decaying in neutrinos, depending of its mass.

The background sources for the analysis considered are the SM processes mediated by an off-shell electroweak boson: for example the process in which an electroweak Z boson, which will decay in two neutrinos, is produced instead of a photon that mixes in a Z' boson. Other possible background sources are the QED processes in which only a photon is detected since the other final state particles produced in the process, for example a second photon or a lepton pair, escape the detector. The author used the signal significance defined as $S \equiv N_{sig}(g_{Z'}, M_{Z'})/\sqrt{N_B}$, where N_{sig} and N_B are respectively the number of signal and background events, in order to determine the sensitivity of *Belle*II to the process in question. Figure 1.8 shows the estimated sensitivity [46].

1.4 Searches at Accelerators

Generally, the experiments that search for *new physics* (NP) are based on two different approaches. The first consists in search for NP at the energy frontier, examples that employ this approach are ATLAS and CMS experiments at LHC that aim at searching NP in the direct production of new particles in proton-proton collisions, while the second consists in search for NP at the precision frontier. The *Belle*II experiment at SuperKEKB is based on this approach, which aim at doing high precision measurements in flavor physics that highlight deviations between the SM and the experimental observations, which could

---

[2] The process is $e^+e^- \to \gamma\gamma$ in which one of the two photons kinematically mixes in Z' that decays in two neutrinos.

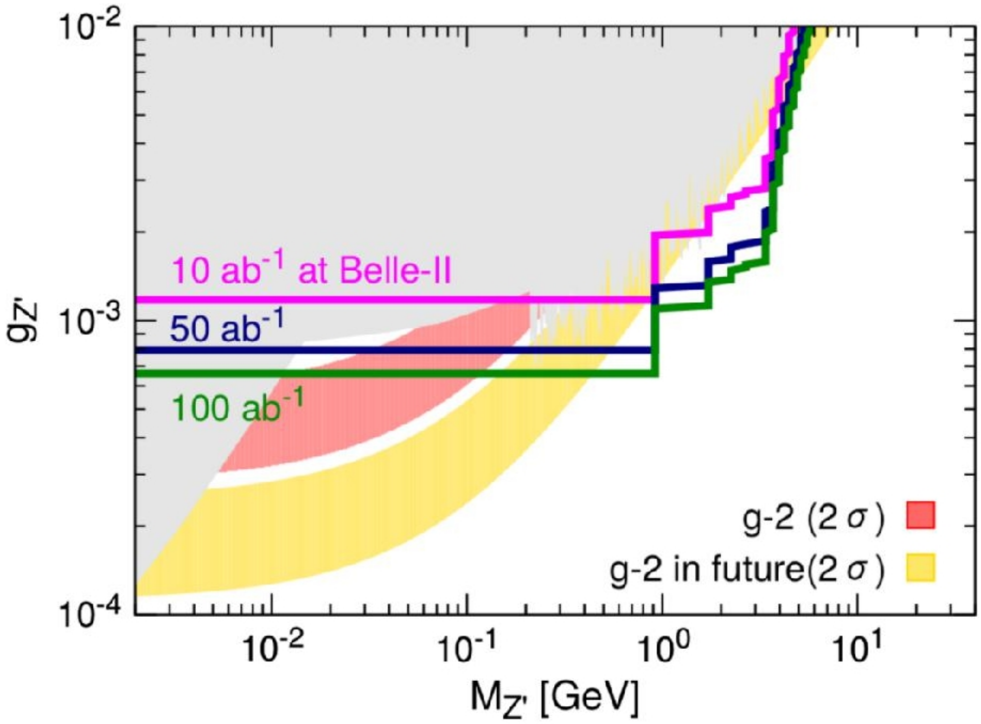

Figure 1.8: Sensitivity of *Belle*II to model parameters of the process $e^+e^- \to \gamma Z', Z' \to \nu\bar{\nu}$, assuming $S > 3$ for different integrated luminosities. The $g_{Z'}$ is the coupling constant of the Z' with fermions, analogous to g' in equation 1.7. The light gray region is the region of the parameters excluded by the Borexino, CCFR neutrino experiments, see the Reference [46] and references therein, and by *BABAR* experiment [54]. The red and the yellow bands are the regions that could explain the a_μ anomaly, respectively coming from the current measurements and the expected future measurements, assuming that in the future measurements the error on a_μ will be reduced and the tensions with the SM prediction will remain of 3σ. The estimations on the sensitivity depends a lot on the photon energy resolution ΔE_γ and on the energy in the center of mass $\sqrt{s}$, since $N_b \propto \sqrt{s}\Delta E_\gamma$, in this case it is assumed to be $\Delta E_\gamma = 0.1$ GeV and $\sqrt{s} = 10.58$ GeV. The image is taken from Reference [46].

be interpreted through new physics models. The sensitivity of the experiments on new physics depends on the model parameters, luminosity of accelerators and performance of the detectors.

Many experiments and different strategies have been developed for the search for NP, some of them are described in the following sections.

Search for signals of the minimal *dark photon* scenario

The search for *dark photon* can be pursued in collider and in fixed target experiments and the main production channels include the bremsstrahlung emission, the production in electron-positron annihilation and in meson decays. A brief description of different searches for the kinetically-mixed *dark photon*, as introduced in the minimal scenario, are listed in the following.

***Dark photon* at fixed target experiments** The search for the *dark photon* can be pursued in fixed target experiments, in which and electron beam collides with a nuclear target and electrons interact with nuclei in the target according to the process $e^-Z \to e^-ZA'$, where Z is the atomic number of nuclei in the target and A' is the *dark photon* produced *via* bremsstrahlung emission. If the energy of the electron beam is much higher than the *dark photon* mass, the *dark photon* carries the highest part of the beam energy and electrons are scattered at large angles.

***Dark photon* at colliders** The *dark photon* can be produced also in colliders, for example in e^+e^- annihilation. For this kind of search, a relevant process is $e^+e^- \to \gamma A'$ where the *dark photon* A' can decay in a visible state, $A' \to l^+l^-, l = e, \mu, \tau$, or in an invisible state, $A' \to$ Invisible.

In particular, for what concerns the B-Factories, the *dark photon* could be produced via direct production in e^+e^- annihilations, in resonant production by the decay of $\Upsilon(nS)$ or in rare flavor changing B meson decays. The accessible mass of the *dark photon* in colliders is limited by the center of mass energy. The rejection of background is one of the most relevant issues because of the high luminosity environment of B-Factories and the small cross sections of processes involving the *dark photon*. Furthermore, there may be additional difficulties, depending on the considered process: in section 1.5 the process $e^+e^- \to \mu^+\mu^- Z', (Z' \to \text{Invisible})$ and problems related to its study will be discussed. Some constraints on the parameters of kinetic mixing model, through the search for the visible and invisible decays of the *dark photon*, have been put by BABAR using respectively a data sample of 514 fb^{-1} and a data sample of 53 fb^{-1} [55].

In the case in which the *dark photon* decays in an invisible state, what should be observed is a peak in the missing mass distribution, defined as $M^2_{miss} = s - 2\sqrt{s}E^{CM}_{\gamma}$, corresponding to the *dark photon* mass. The event selection in this case needs the single photon trigger. For $M_{miss} \approx 0$ GeV, which means that $E^{CM}_{\gamma} \approx \sqrt{s}/2$, the background is dominated by $e^+e^- \to \gamma\gamma$ events in which one photon escapes the detector. At higher masses of the *dark photon*, the background is dominated by radiative Bhabha events in which both the electron and the positron are undetected.

In the case in which the dark photon decays in a visible state, $A' \to l^+l^-$, what should be observed is a peak in the dilepton invariant mass distribution, defined as $M^2_{l^+l^-} = s - 2\sqrt{s}E^{CM}_{\gamma}$, corresponding to the *dark photon* mass value. For example, when $l = e, \mu$ the background sources for this process are radiative Bhabha events, $e^+e^- \to \mu^+\mu^-(\gamma)$ events, $e^+e^- \to \gamma\gamma$ events, where a photon convert in a lepton pair, and $e^+e^- \to R(\gamma)$ events where R is a resonance that decays in a lepton pair, as for example $J/\psi \to \mu^+\mu^-$.

Figures 1.10 and 1.9 show the current experimental limits on the parameters of the kinetic mixing model (gray regions), respectively, for the invisible and visible *dark photon* decays. The colored curves show the prospects of the experimental limits that will be reached in future experiments.

***Dark photon* in meson decays** If the *dark photon*-quarks coupling is not zero, the *dark photon* can be produced in meson decays. If the *dark photon* mass is small enough, it could be produced in rare decays of light mesons, for example $K \to \pi A'$ or $\pi^0 \to \gamma A'$. In this cases the *dark photon* mass is limited by the parent meson mass. The production of the *dark photon* in meson decays can be studied also in e^+e^- colliders, since several mesons that decay inside the detectors are produced.

Constraints on LDM In several models, LDM particles don't interact directly with ordinary matter, but through new mediators that couple both with SM particles and DM particles. For this reason could be possible produce and detect LDM particles in

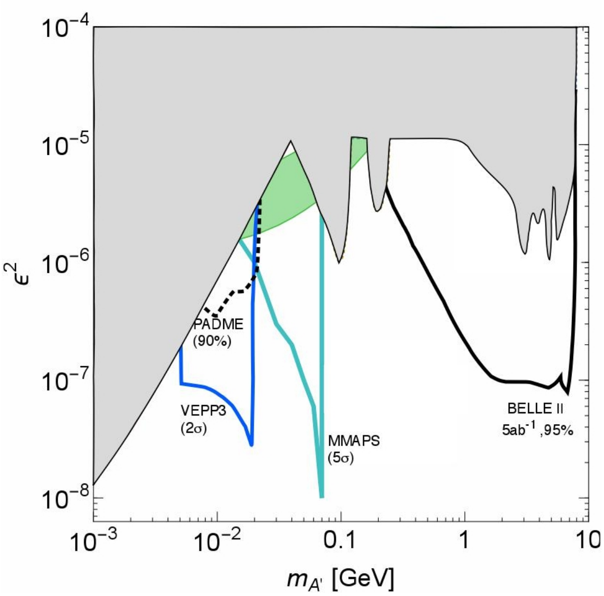

Figure 1.9: Sensitivity on the parameters of the kinetically-mixed *dark photon* model for the decay $A' \to$ Invisible, where $m_{A'}$ is the mass of the *dark photon* and ϵ is the *kinetic mixing* strength between the SM photon and the *dark photon*. Gray regions are the current experimental limits on the parameters of the model, while colored curves show the prospects of the experimental limits that will be reached in future experiments. Image taken from Reference [22].

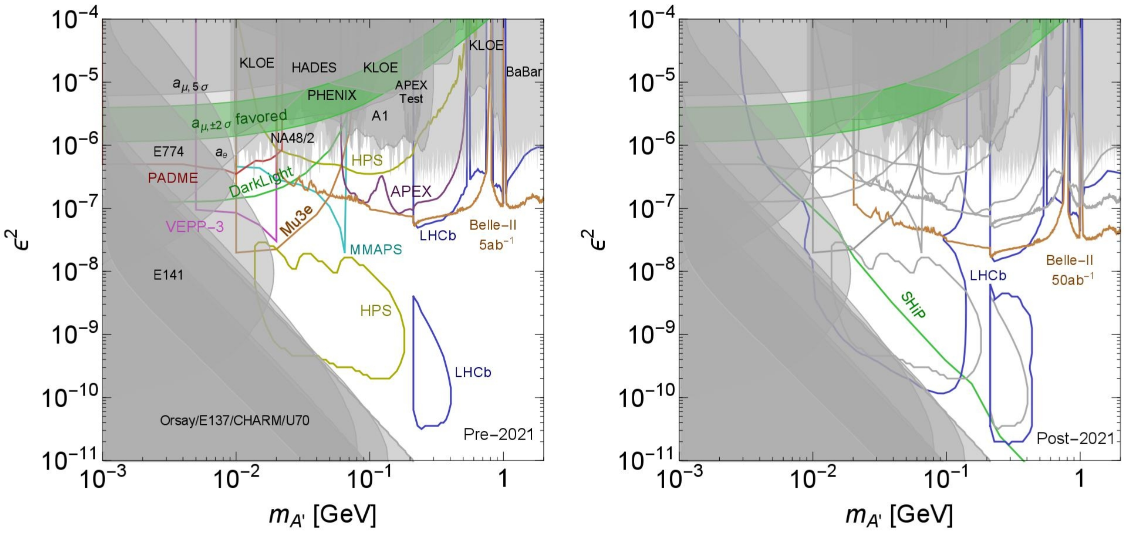

Figure 1.10: Sensitivity on the parameters of the kinetically-mixed *dark photon* model for the visible decay $A' \to l^+l^-$, where $m_{A'}$ is the mass of the *dark photon* and ϵ is the *kinetic mixing* strength. Gray regions are the current experimental limits on the parameters of the model, while colored curves show the prospects of the experimental limits on the parameters that will be reached in future experiments. The green band shows the region in which the *dark photon* could explain the a_μ anomaly. In the right image the expected experimental sensitivity by 2021 are shown, while in the image on the left longer term prospects beyond the 2021 are shown. Image taken from Reference [22].

laboratories.

As said Section 1.3, there are different *portals* with which DM could interact with SM particles, but the most viable is the vectorial portal that introduce the kinetically-mixed *dark photon* A' that can decay in DM particles.

The searches for the *dark photon* allow to put some constraints on LDM candidates and Figure 1.11 shows a summary of constraints on LDM candidates provided by different kinds of experiments based on missing momentum and missing energy.

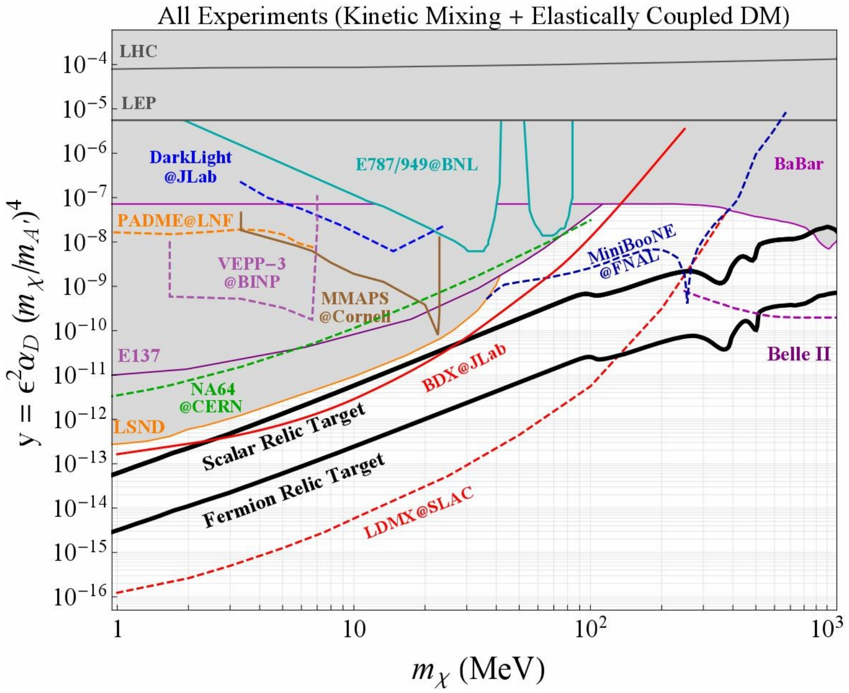

Figure 1.11: Summary of constraints from different experiments on direct LDM production in the context of a kinetically-mixed *dark photon*. The parameter m_χ is the mass of the LDM particle, and y is a dimensionless parameter that depends on the coupling between the DM particles and the *dark photons* α_D, the kinetic mixing strenght ϵ, the *dark photon* mass $m_{A'}$ and the dark matter particle mass m_χ. The y parameter is fixed by the decay width of the *dark photon* in DM that depends on DM relic abundance and on the assumed annihilation cross section of DM particles. Image taken from Reference [22], for details see Reference [56].

Search for signals of a rich *dark sector* scenario

If DM is part of a wider *dark sector*, its experimental signature can differ significantly from that of the minimal scenario described above. Due to the lack of any evidence of DM to date, the search strategies need to be expanded over a wide range of possible theories. Furthermore, several questions arise relating to the origin of the *dark photon* mass, the possibility to have more states in *dark sector* in addition to DM and *dark photon*, the entity of their couplings to SM particles and the influence of these states on cosmology, astrophysics and phenomenology. Experiments on kinetically-mixed *dark photon* can also be sensitive to the parameters of some rich *dark sector* models that predict new gauge interactions. Many existing experiments can investigate models introducing new *dark sector* states, as for example the $L_\mu - L_\tau$ model studied in this thesis work. Some examples are in References [57, 58, 59, 47] and Figure 1.12 shows constraints on exotic *dark sector* obtained reinterpreting the existing results on the parameters of the kinetically-mixed *dark photon* model in terms of some rich *dark sector* models. This is possible if experiments provide information about constraints on kinetically-mixed *dark photons* as a function of the individual couplings with leptons or quarks.

One of the possible mechanism that could explain the *dark photon* mass is the dark

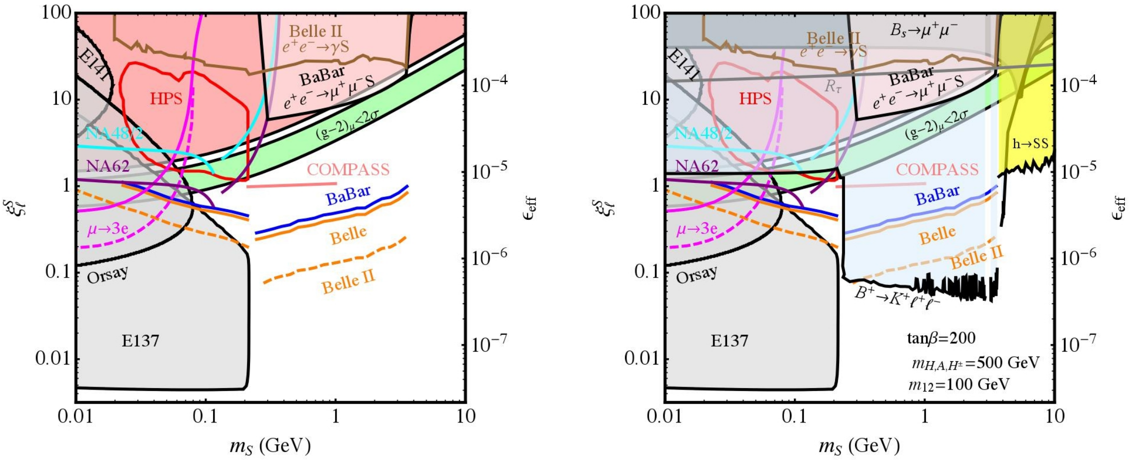

Figure 1.12: Summary of the constraints on a *leptophilic* dark scalar S. The ξ_l^S parameter is the S-leptons coupling and it is analogous to the SM Yukawa coupling of leptons with a scalar particle. Leptophilic DM consists of DM particles that have tree-level couplings only with leptons but not with gauge bosons or quarks (for details see Reference [60]). Left: model independent constraints and projections assuming only the coupling between S and leptons. Right: constraints and projections on a model that assumes an additional coupling between the scalar S and the b quarks. Image taken from Reference [22].

Higgs mechanism that introduce a *dark Higgs* boson h'. An example of a process involving an exotic *dark sector* that allows to search for *dark Higgs* production is the six-lepton final state, already investigated by *BABAR* [61] and *Belle* [62]. It consists of the production of a *dark photon* and a *dark Higgs* in electron-positron annihilation, the process is $e^+e^- \to A'h', h' \to A'A'$. The *dark Higgs* is emitted *via* Higgs-strahlung, and each *dark photon* decays in a lepton pair, $A' \to l^+l^-$. Another possibility is the production of a six-lepton final state by a DM bound state coming from the electron-positron annihilation. The DM bound state decays in three dark photons each of them decays in a lepton pair [22].
The selection of those events can be expanded requiring for missing energy, in order to include possible invisible particles. KLOE experiment looks for the same process, but with h' decaying invisibly [63].

BABAR studied different processes that allow to limit different rich *dark sector* models. Some examples are the following processes: $e^+e^- \to \mu^+\mu^-Z', Z' \to \mu^+\mu^-$ that provides a test of the gauge boson introduced by the $L_\mu - L_\tau$ model and a test for all those models that predict leptophilic dark scalars with mass $m_S > 2m_\mu$ and $m_S < 2m_\tau$ [54], $e^+e^- \to \mu^+\mu^-S, S \to l^+l^-$ where $l = e, \mu$ that provides limits on a dark scalar boson S model [64]; $e^+e^- \to A'^* \to W'W' \to 4l$ that provides constraints on the *dark photon* introduced inside a model that extend the SM with a non-Abelian gauge group $SU(2)$ [65].

LDM particles can be produced also at high-energy colliders through direct production in the collisions or in the decays of heavy gauge bosons or in the Higgs decays. These production mechanisms are predicted by many rich *dark sector* models, for this reason the ATLAS, CMS and LHCb experiments have a wider research program focused on *dark sector* searches that comprises:

- the search for Higgs decays in different final states as *dark sector* particles, dilepton resonances, b-quark resonances, low-mass DM particles and photons [67, 66];
- the search for new lepton resonances in semileptonic B meson decays [68];

- the search for *lepton-number-violating* processes in which the B mesons decay *via* sterile neutrinos [69] or new low-mass, long-lived, hadronically decaying particles [70]. Sterile neutrinos, called also *Neutral Heavy Leptons* (NHLs), are hypothetical particles that does not interact with SM particles through any SM interaction, except for the gravitational interaction. They are right-handed neutrinos introduced in the SM in order to give rise to the neutrino mass term naturally [71].

Search for *Axion Like Particles.*

Another field of research in the *dark sector* concerns the ALPs, which are neutral spin-zero states with a pseudoscalar coupling with the SM particles, which is described by the pseudoscalar *portal* introduced in Section 1.3. For what concerns the research of ALPs at the accelerators, experimental constraints come from studies of processes involving the coupling between ALPs and photons or ALPs and leptons. The main channels include: $e^+e^- \to \gamma a$ at B-Factories or $pp \to \gamma a$ at LHC, SM Higgs boson and electroweak Z boson decays ($h \to Za$, $h \to aa$ and $Z \to \gamma a$) where the axion a decays in a photon pair or a lepton pair. Figure 1.13 shows the existing constraints on the couplings of ALPs respectively with leptons (right) and photons (left), coming from particle physics experiments, astro-particle physics and cosmological observations. The searches for ALPs at collider are sensitive to the couplings C_i/Λ in the range $\mathcal{O}(1\ \text{TeV})^{-1} \div \mathcal{O}(100\ \text{TeV})^{-1}$, where C_i are some appropriate coefficients in the effective Lagrangian of ALP interactions. The Λ parameter indicates a new-physics energy scale, which is the characteristic scale at which the spontaneous global symmetry breaking occurs [72]. The $|C^{eff}_{\gamma\gamma}|$ and $|c^{eff}_{ll}|$ parameters are effective coefficients appearing in the axion decay width, respectively, in 2γ and in $2l$, which are reported for completness in the following:
$\Gamma(a \to \gamma\gamma) \sim \alpha m_a^2 \left(|C^{eff}_{\gamma\gamma}|/\Lambda\right)^2$, $\Gamma(a \to l^+l^-) \sim m_a m_l^2 \left(|c^{eff}_{ll}|/\Lambda\right)^2 \sqrt{1 - 4m_l^2/m_a^2}$ [72].

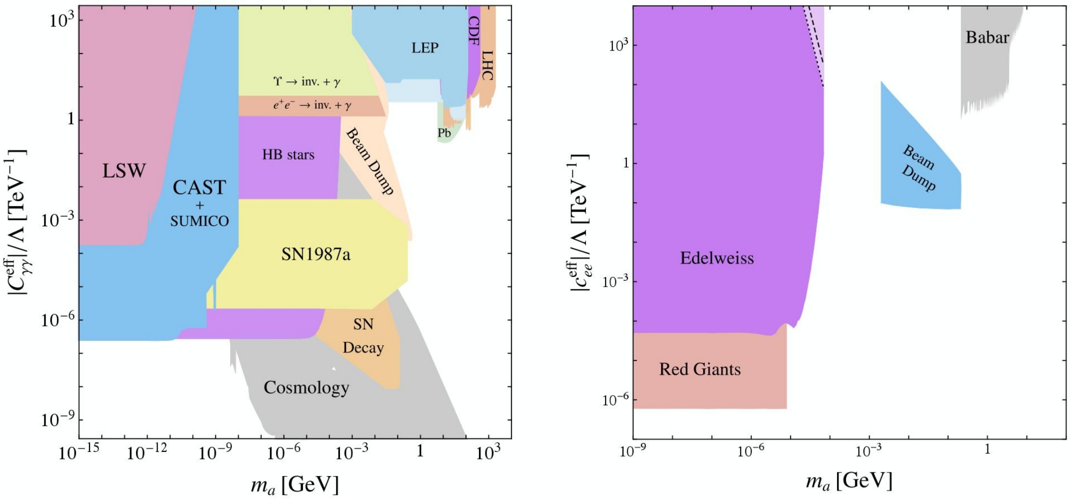

Figure 1.13: Left: Existing constraints on the ALPs-γ coupling. Right: Existing constraints on the ALPs-leptons coupling. The limit established by the BABAR experiment is a constraint on $|c^{eff}_{\mu\mu}|$ that can be interpreted as a limit on $|c^{eff}_{ee}|$ assuming $c_{\mu\mu} \approx c_{ee}$.
The constraints are provided by particle physics experiment and astrophysical and cosmological observations. Image taken from [72].

1.5 Motivations for $Z' \to$ Invisible searches

The purpose of this thesis work is to investigate the production of a light dark gauge boson Z' in association with a muon pair in electron-positron annihilations at the center of mass energy of 10.58 GeV, and Z' boson is emitted radiatively by one of the two muons, as shown in the Feynman diagram in Figure 1.14. The process analyzed in this thesis is reported in Equation 1.9.

$$e^+e^- \to \mu^+\mu^- Z'(Z' \to \text{Invisible}) \tag{1.9}$$

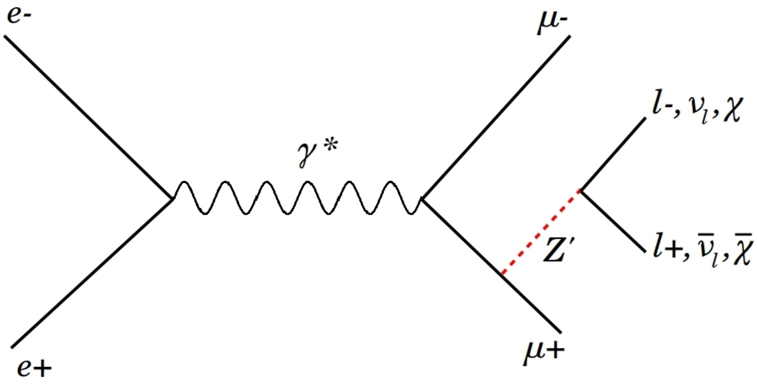

Figure 1.14: Feynman diagram of the processes $e^+e^- \to \mu^+\mu^- Z', Z' \to l^+l^-, l = e, \mu, \tau$ and $e^+e^- \to \mu^+\mu^- Z', (Z' \to \text{Invisible})$. The invisible final state of the Z' decay can be a $\nu\bar{\nu}$ state or a $\chi\bar{\chi}$ state, which is the favored one if a χ DM particle lighter than the Z' boson exists.

While the analysis of the process $Z' \to \mu^+\mu^-$ has been already performed by the *BABAR* experiment using a data sample of 514 fb^{-1} [54], the process in which the Z' decays in an invisible state has never been investigated yet.

The signature of signal events consists of two muon tracks coming from the interaction point plus missing mass. Since muons are very penetrating and well identifiable particles, a selection based on the particle identification can be used to reject a large part of background and the signal reconstruction efficiency is expected to be quite high. Furthermore, as described in Chapter 3, the *Belle*II detector allows to reconstruct and identify muons with high efficiency.

The Z' that decays in an invisible final state appears as missing mass and the signal yield is extracted by fitting the distribution of the recoil mass against the muon pair with respect to the center of mass momentum, which is expected to peak at the Z' mass.

The preliminary analysis of the process will be performed using the data sample collected during the data taking period known as *Phase*-2, see Section 2.2.

The data sample collected during *Phase*-2 is not enough to reach the sensitivity required by the analysis which will be finally performed using the data sample collected during the next data taking period known as *Phase*-3, whose expected data sample of 50 ab^{-1} will allow to strongly constrain several *dark sector* models and perform several NP searches.

This analysis allows to constrain the $L_\mu - L_\tau$ model, which is a very well theoretically motivated *dark sector* model that introduces the Z' boson. The model predicts that the Z' couples only with particles characterized by muonic and tauonic flavours, i.e. μ, τ and $\nu_{\mu\tau}$. A different possible process that allows to constraint the same model is

$e^+e^- \to \tau^+\tau^- Z', (Z' \to \text{Invisible})$, in which the Z' is emitted radiatively by one of the two tauons. This process is experimentally more challenging and can only be explored with the full detector installed and a large data sample.

The analysis of the process $e^+e^- \to \mu^+\mu^- Z', (Z' \to \text{Invisible})$ is the first *dark sector* analysis of the *Belle*II experiment and it has been used also to test and understand the performances of the detector and of the *Belle*II software tools.

Chapter 2

Experiments at B-Factories

BABAR and *Belle* experiments are the first generation of B-Factories. They were located respectively at the PEP-II (SLAC National Accelerator Laboratory) and at the KEKB (KEK) electron-positron colliders and they have been operational from 1999 to 2008. In the period of their activity they got important results in the study of bottom physics, charm physics, τ physics and in the search of new physics beyond the SM. In particular their most relevant result was the discovery of $\mathcal{CP}$ violation in the B sector complemented by many precision measurement of CKM matrix elements as well as rare decay processes. *Belle*II is the upgrade of the *Belle* experiment and it is located at the SuperKEKB collider, which is the upgrade of the previous accelerator KEKB.

As discussed in Section 1.3, the SM has a lot of open questions and *Belle*II is designed to answer these questions through searches of new physics. The approach used by *Belle*II is to do high precision measurements of flavour physics processes that are suppressed in the SM and could be sensitive to new physics. The evidence of deviations between SM predictions and experimental results can be interpreted through new physics models. The sensitivity on new physics depends on the new physics models, on the performances of the detector and on the size of the data sample. *Belle*II is planning on a fifty times higher statistics and improved performances with respect to the first generation of B-Factories, so it can be very competitive in new physics searches.
Some examples of the *Belle*II experiment searches are detailed below [73].

- The possibility that in the quark sector more than one $\mathcal{CP}$ violating phases able to explain the baryon/anti-baryon asymmetry are present. This possibility can be investigated examining the difference between B and $\bar{B}$ meson decay rates through time dependent $\mathcal{CP}$ violation measurements in transitions $b \to s$ and $b \to d$ or in the charm mixing mechanism that, being suppressed in the SM, could be sensitive to new phenomena involving u-type quarks.

- Investigate models that foresee multiple Higgs bosons, also electromagnetically charged, in addition to the neutral SM Higgs boson. The signature of these additional Higgs bosons can be searched in B meson leptonic and semileptonic decays involving τ leptons, for example $B \to \tau\nu_\tau$ and $B \to D^*\tau\nu_\tau$.

- The presence of flavour-changing neutral currents (FCNC) beyond the SM, improving measurements of $b \to s$, $b \to d$ and $c \to u$ transitions, for which the measurement of the $B \to K\nu\bar{\nu}$ decay is of great interest.

- Search of *Lepton Flavour Violating* processes, such as $\tau \to \mu\gamma$, which is forbidden in the SM.
- Search of hidden particles, coupling with SM particles through new gauge symmetries, at the mass scale in the range MeV/c^2-GeV/c^2 predicted by *dark sector* models. These models predict a wide variety of DM candidates and new gauge bosons. An example is the *dark photon* search through the process $e^+e^- \to \gamma A'$, where A' is the dark photon that can decay visibly or invisibly.
- Detailed analysis of bound states of quark or multiquark states, as quarkonium, to better understand the nature of the strong force in hadrons.

In this chapter the physics of the B-Factories is introduced and a detailed presentation of the SuperKEKB accelerator will be made, while Chapter 3 is dedicated to the description of the *Belle*II experiment.

2.1 Overview of experimental methods of B-Factories

B-Factories are e^+e^- colliders designed to study the physics of B mesons providing a clean environment and a very well known initial state. The idea of B-Factories was born from the necessity to have big samples of B mesons in order to test the $\mathcal{CP}$ violation in the B sector. From CKM matrix, the $\mathcal{CP}$ violation in the B sector is expected to be larger than $\mathcal{CP}$ violation in the K sector [1], since it involves directly the third quark generation. In B-Factories, $B^0\bar{B}^0$ meson pairs and B^+B^- meson pairs are produced through electron-positron collisions at the $\Upsilon(4S)$ resonance energy peak in the center of mass (CM) reference system: $\sqrt{s} = M_{\Upsilon(4S)} = 10.58$ GeV. The $\Upsilon(4S)$ resonance is a bound state of one b quark and one $\bar{b}$ anti-quark and it is the first bottomonium state whose mass allows the decay in a B meson pair. The properties of the $\Upsilon(4S)$ resonance, of B mesons produced by the decay of the $\Upsilon(4S)$, and the production cross sections for different processes at the $\Upsilon(4S)$ energy in the center of mass are listed in Table 2.1. The branching ratio of the $\Upsilon(4S)$ decay in B mesons is higher than 96% [2, 73, 74].
The relevant features of B-Factories are reported in the following [74], with the indication they are modified in SuperKEKB/*Belle*II:

- an asymmetric e^+e^- collider is needed because the *Q-value* of the process $\Upsilon(4S) \to BB$ is $Q = M_{\Upsilon(4S)} - 2M_B \simeq 20\text{MeV}/c^2$, hence the momentum of the B meson in the CM frame is very small, about $p^*_B \approx 300$ MeV/c, so B mesons are produced almost at rest in the CM reference system. In the case of symmetric colliders, the short lifetime of B mesons leads a displacement between the primary interaction vertex and the decay vertex of B mesons of about 30 μm that is hardly measurable, considering the state-of-the-art of vertex detectors. An asymmetric collider provides a Lorentz boost of the CM frame in order to improve the decay length $l = c\tau\beta\gamma$ of B mesons in the laboratory frame. The boost allows to reconstruct the decay vertices and to extract temporal information;

---

[1] The $\mathcal{CP}$ violation in K meson system was observed for the first time in 1964 in the experiment performed by physicist J. Cronin and V. Fitch realized at the *Alternating Gradient Synchrotron* (AGS) installed at the BNL, Brookhaven, New York.

	M (MeV/c^2)	J^{PC}	Γ (MeV)	Composition in quarks
$\Upsilon(4S)$	10579 ± 1.2	1^{--}	20.5 ± 2.5	$b\bar{b}$

	M (MeV/c^2)	J^{P}	τ_B ($\cdot 10^{-12}s$)	Composition in quarks
B^0	5279.58 ± 0.17	0^-	1.519 ± 0.007	$d\bar{b}$
B^+	5279.25 ± 0.17	0^-	1.641 ± 0.008	$u\bar{b}$

$e^+e^- \to$	$b\bar{b}$	$c\bar{c}$	$s\bar{s}$	$u\bar{u}$	$d\bar{d}$	$\tau^+\tau^-$	$\mu^+\mu^-$	e^+e^-
Cross section (nb)	1.05	1.30	0.35	0.39	.35	0.94	1.16	∼40

Table 2.1: The table reports the properties of the $\Upsilon(4S)$ and of B mesons B^0B^+. The values have been taken from the PDG [2]. B mesons are not eigenstates of charge conjugation, indeed they are composed by two quarks, one of which is heavier than the other, hence J^P, and not J^{PC}, is listed for B mesons. In the last two lines: the production cross sections in e^+e^- annihilation for different processes evaluated at the $\Upsilon(4S)$ energy in the center of mass, $\sqrt{s} = 10.58$ GeV/c^2 [75].

- in origin a high luminosity was required for $\mathcal{CP}$ violation studies in the B sector, since B mesons have many decay channels with a small branching ratio. For example, the process $B^0 \to J/\psi K_S,\ J/\psi \to l^+l^-$ is very interesting for $\mathcal{CP}$ violation studies since it is directly related to the measurement of the β parameter of the unitarity triangle shown in Figure 1.1, however its B meson decay branching ratio is around 10^{-4}%. In the new generation of B-Factories an even higher luminosity is required for studies of processes that are suppressed in the SM and are sensitive to new physics. The first generation of B-Factories reached a luminosity of about $2 \cdot 10^{34}$ cm^{-2}s^{-1}, while *Belle*II aims to reach an instantaneous luminosity of $8 \cdot 10^{35}$cm^{-2}s^{-1};

- a clean environment with a high signal-to-noise-ratio (SNR) for $b\bar{b}$ events. These events are characterized by a higher mean charged multiplicity, around 11 tracks for event, with respect to background events, as shown in Figure 2.1. Furthermore, the clean environment allows to apply simple trigger strategies;

- a hermetic detector designed to observe all decay products of the interaction between e^+ and e^- in the collider: the detector covers the greatest possible geometric acceptance around the interaction region (IR) and it incorporates multiple sub-detectors. The reliability of the detector in the reconstruction of neutral particles as π^0 and γ is also relevant;

- the initial state and the momentum of B mesons in the center of mass reference system are completely known and it is possible exploit these information to apply kinematical constraints on reconstructed candidates. This is relevant for the rejection of the background.

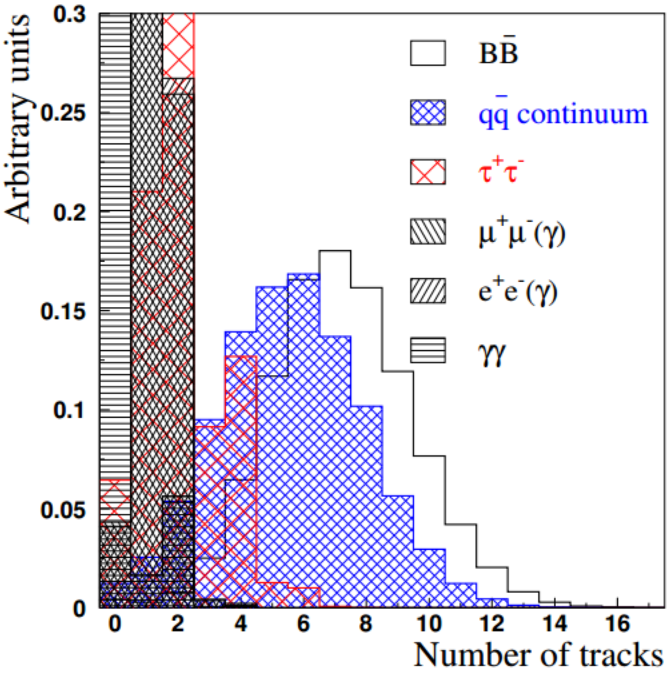

Figure 2.1: The figure shows the number of charged tracks per event for different processes. The graph was taken from section 9.4.1 of *The Physics of the B factories* [74].

Kinematical variables of $B\bar{B}$ events

The experimental setup of B-Factories allows to use kinematical constraints in order to discriminate between signal and background B meson candidates. It improves also the knowledge of B meson momenta. The $\Upsilon(4S)$ decays in two B mesons of same mass: if B mesons are well reconstructed, the total energy of their decay products is half of the $\Upsilon(4S)$ invariant mass and their invariant mass is the same as the mass of the B meson [74]:

$$\begin{aligned} E^*_{rec} &= E^*_{beam} = \frac{\sqrt{s}}{2} = \frac{M_{\Upsilon(4S)}}{2} \\ m_{rec} &= m_B \end{aligned} \tag{2.1}$$

The apex * is referred to quantities calculated in the CM frame.

In order to use the kinematic information of B meson decays, two variables are used: the energy difference ΔE and the beam-energy substituted mass m_{ES}, defined in the CM system below.

$$\begin{aligned} \Delta E &= E^*_B - E^*_{beam} \\ m_{ES} &= \sqrt{\frac{\left(\frac{s}{2} + \mathbf{p}_B \mathbf{p}_0\right)^2}{E_0^2} - |\mathbf{p}_B|^2} \end{aligned} \tag{2.2}$$

The reconstructed energy of the B meson is E^*_B, while E^*_{beam} is the beam energy. $(E_0, \mathbf{p}_0)$ represents the quadri-momentum of the CM system calculated in the laboratory frame and $\mathbf{p}_B$ is the reconstructed tri-momentum of the B meson. The definition of m_{ES} reported in the equation is the one used by *BABAR* experiment.

The ΔE distribution is expected to peak at 0 MeV, while the m_{ES} distribution is expected to peak at the B meson mass for signal events $\Upsilon(4S) \to B\bar{B}$. The uncertainty of ΔE depends on the uncertainty on the B meson energy measurement and on the beam energy spread: the dominant contribution comes from the uncertainty on E_B^*, which depends on detector energy resolution, especially for those final states involving photons. ΔE depends strongly on the mass hypothesis of particles in the final state, since it depends on the energy of the reconstructed B meson that needs the momenta and the mass assignment to be calculated. The misidentification of particles causes a shift of ΔE towards positive or negative values depending on whether a particle produced in the B meson decay is misidentified as a heavier particle or a lighter particle. For example, if a pion is misidentified as a kaon, the energy associated to this particle, and consequently associated to the reconstructed B meson, will be higher than the true value, hence ΔE will be shifted towards positive values. Since ΔE peaks at 0 MeV for signal events, it is a very effective variable for discriminating signal events from background events involving misidentification.

In contrast, m_{ES} variable is not affected by the mass hypothesis since it depends only on tri-momenta reconstruction. The dominant contribute on m_{ES} uncertainty comes from the beam energy spread $\sigma_{E^*_{beam}}$, while the contribution due to the reconstructed B momenta $(p^*_B/m_B)\sigma_{p^*_B}$ is negligible since B mesons are produced almost at rest in the CM frame, hence the value $(p^*_B/m_B) \approx 300/5279 \approx 0.06$ is small. The typical m_{ES} resolution is around 3 MeV$/c^2$ if there are no neutral particles in the final state, while the ΔE resolution depends on the B meson decay mode and it can change from around 5 MeV, for high mass final states, to around 30 MeV, for low mass final states.

Figure 2.2 shows an example of m_{ES} and ΔE distributions.

Finally, Figure 2.3 shows the correlation between the two variables described in this section for the $\bar{B}^0 \to \Lambda_c^+ \bar{p} \pi^- \pi^+$ decay. A strong correlation between ΔE and m_{ES} is present since both variables are calculated starting from the same quantities: the beam energy, the measured momenta of charged particles and the energy of neutral particles. On the contrary the correlation between the invariant mass of the reconstructed B meson and the m_{ES} variable becomes small since the invariant mass does not depend on beam energy.

B-Factories detectors

The main requirements of the *B*-Factories detectors are in the following [74].

- Low material budget for inner detectors in order to reduce multiple scattering effects: for example, beryllium was chosen to made the beam pipes, since it has a low atomic number, so multiple scattering and the loss of energy of particles crossing the beam pipes are minimized.

- Vertex detection capability in order to determine the B meson decay vertex with very high precision: it is fundamental for time dependent $\mathcal{CP}$ violation measurements. Strip-vertex detectors are used for this purpose. The *Belle*II vertex detector is composed by a Pixel Vertex Detector (PXD) and a Silicon Vertex Detector (SVD), both described in section 3.

- Particle identification (PID) capability in order to classify particles in the final state. A Central Drift Chamber (CDC) able to provide measures of dE/dx to perform PID of low momentum tracks is installed into the detectors. In addition to the CDC, a Time-of-Propagation (TOP) detector and an Aerogel Ring-Imaging Cherenkov (ARICH) detector for PID of high momentum tracks are installed on the *Belle*II detector.

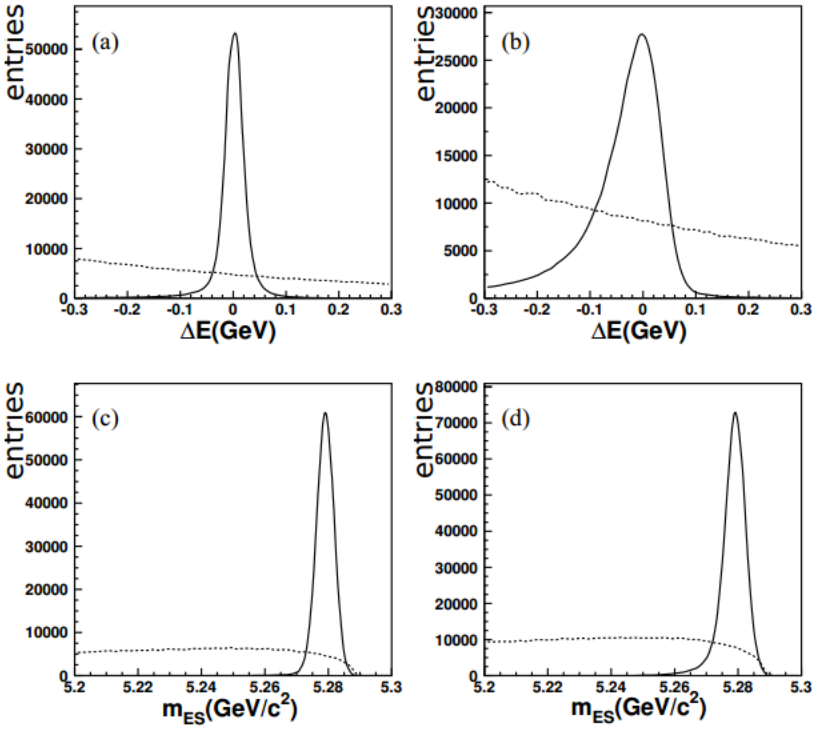

Figure 2.2: The ΔE and m_{ES} distributions for $B^+ \to K_S\pi^+$ mode, graphs (a) and (c), and for $B^+ \to K^+\pi^0$ mode, graphs (b) and (d). Solid line histograms show signal events, while dotted line histograms show the background continuum; both are produced using the official MC production. Graph (b) shows a worse ΔE resolution than graph (a) due to the presence of the neutral pion in the $B^+ \to K^+\pi^0$ mode final state that decay in two photons: the long tail at low ΔE values is due to photons shower leakage in the calorimeter. The same thing is less observable in the case of the m_{ES} resolution, graph (d), because it is less affected by the uncertainty on the measurement of the B meson reconstructed quadri-momentum, as explained in the text. The graphs are taken from section 7.1.1.2 of *The Physics of the B factories* [74].

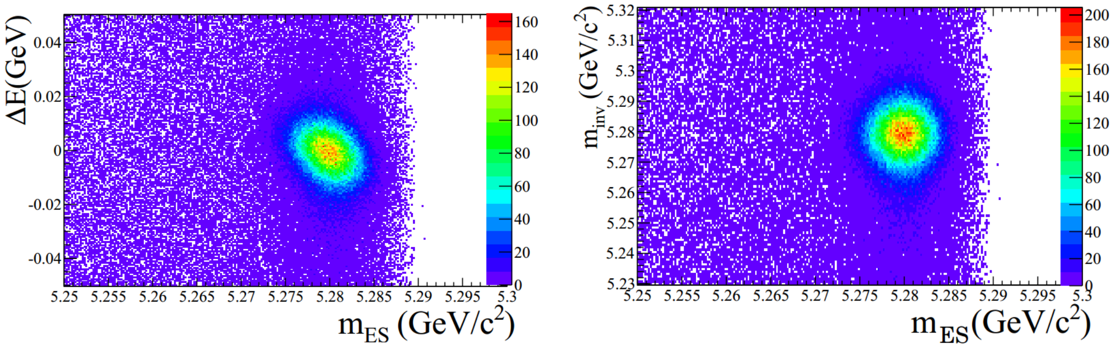

Figure 2.3: Scatter plots of Δ_E vs m_{ES} (left) and of $m_{inv} = m_B$ vs m_{ES} (right) for the $\bar{B}^0 \to \Lambda_c^+\bar{p}\pi^-\pi^+$ mode. The graph on the left shows the correlation between Δ_E and m_{ES}. The graph on the right shows m_{inv} vs m_{ES} that are very weakly correlated. The graphs are taken from section 7.1.1.2 of *The Physics of the B factories* [74].

- An electromagnetic calorimeter, which is composed of CsI(Tl) crystals, in order to measure the energy of both electron and neutral particle final states.
- K_L mesons and μ detectors because, in contrast with K_S mesons that decay into the beam pipes because of their very short mean lifetime, $\tau_{K_S} \approx 9{\cdot}10^{-11}$ s, the K_L mesons have a long mean lifetime, $\tau_{K_L} \approx 5 \cdot 10^{-8}$ s, hence they cross the whole detector and can only be detected through their hadronic interactions in the outer detector. Muons

also cross the whole detector because they interact little compared to electrons. It is very important detect efficiently K_L and μ because some processes, as for example $B^0 \to K_S J/\psi$ and $B^0 \to K_L J/\psi$ where $J/\psi \to l^+l^-$, are fundamental to verify $\mathcal{CP}$ violation in B meson decays. *Belle*II is equipped with a K_L and μ detector (KLM) described in Chapter 3

- Significant computing power is needed to manage the big data flow from the detectors electronic to the storage system. This is achieved by a combination of local computing farms for prompt event reconstruction and high level trigger, and a distributed (Grid) computing environment

A detailed description of the *Belle*II apparatus is provided in Chapter 3.

2.2 B-Factories colliders and SuperKEKB

In order to reach instantaneous luminosity higher than $10^{33}\mathrm{cm}^{-2}\mathrm{s}^{-1}$ and a Lorentz boost factor $\beta\gamma$ that allows to observe the time evolution of B meson decays, the accelerators of B-Factories are constituted of two different storage rings, one for electrons and one for positrons, allowing asymmetric beam energies. Only one IR for the detectors is present in order to optimize the luminosity. The general expression for instantaneous luminosity of e^+e^- colliders is [74]:

$$\mathcal{L} = \frac{N_b n_{e^+} n_{e^-} f}{\mathscr{A}_{eff}} \tag{2.3}$$

The number of bunches is N_b, the number of electrons and positrons for each bunch are respectively n_{e^+} and n_{e^-}, the circulation frequency is f and $\mathscr{A}_{eff}$ is the effective overlapping area of the two beams at the IP.

When high currents circulate in the rings the $\mathscr{A}_{eff}$ parameter becomes strongly beam-current dependent and increases together with $N_b n_{e^+} n_{e^-}$, this $\mathscr{A}_{eff}$ trend limits the instantaneous luminosity achievable.

Increasing the beam current to enhance the luminosity can lead to bunch instabilities along the entire ring that can be caused by coupling between bunches. For example, if the number of bunches N_b increases, the separation between bunches decreases and they can feel effects of near bunches. Another cause for bunch instabilities are the interactions between electrons in the bunches and the residual gas ions in the beam pipes, or between positrons and photoelectrons emitted by the interactions between synchrotron X-rays and beam pipe walls. High currents can also be harmful for hardware components of the accelerator and of the detectors: a very good vacuum level throughout the beam pipes is necessary in order to limit the damage due to high currents in an environment in which hardware components already suffer a large bombardment of synchrotron radiation. In order to achieve a high luminosity is necessary to optimize the fundamental parameters in the definition of the luminosity.

PEP-II and KEKB are the colliders that provided luminosity to the first generation of B-Factories consisting of *BABAR* and *Belle* experiments. In Figure 2.4 a schematic representation of PEP-II and KEKB colliders is shown.

The second generation of B-Factories starts from the KEKB to SuperKEKB upgrading, which is the accelerator designed to provide the luminosity to the *Belle*II experiment.

SuperKEKB is an asymmetric electron-positron collider operating at the $\Upsilon(4S)$ energy

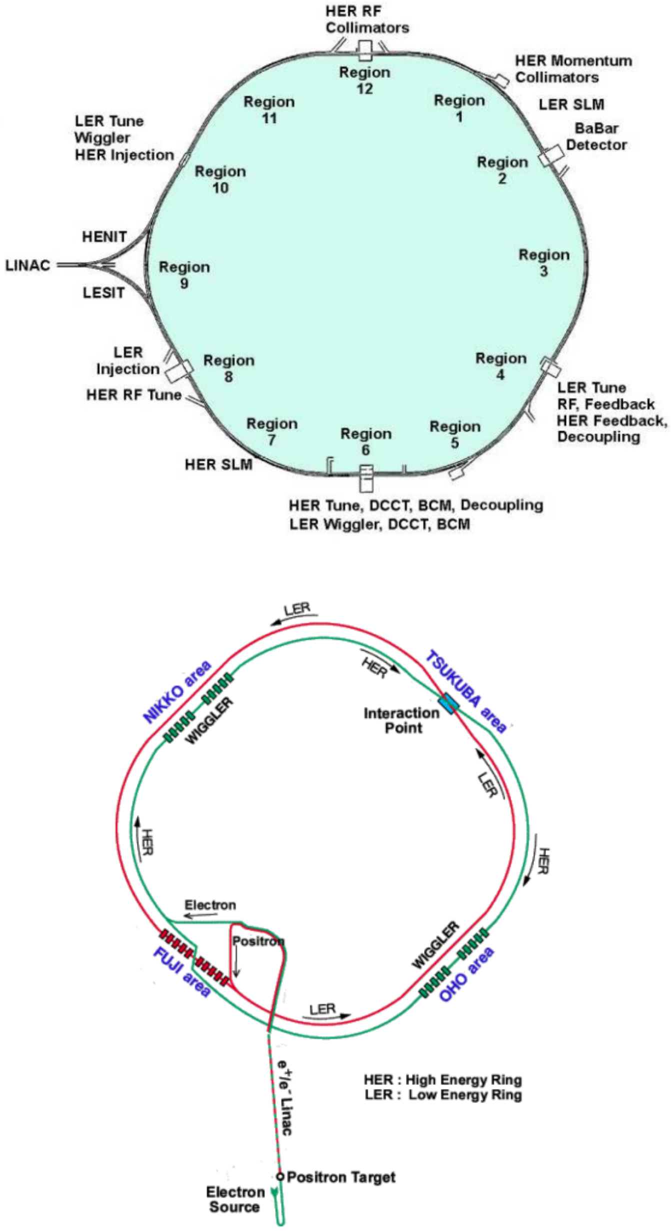

Figure 2.4: Schematic view of PEP-II and KEKB accelerators respectively on the left and on the right. In KEKB the two beams circulate inside the rings one next to the other, while in PEP-II the two rings are one on the top of the other. The images are taken from section 1.2.4 of *The Physics of the B factories* [74].

peak in the CM. The electron beam is generated in the pre-injector, located at the beginning of the linear accelerator (LINAC), through a short-pulse photons laser irradiating a cold cathode. The positron beam is generated irradiating a fix target of tungsten with electrons, hence positrons are produced as secondary particles of interactions between electrons and tungsten nuclei. Electrons used for positron production are generated in a different pre-injector, compared to that used for the electron beam, because the production of positrons requires much higher electron intensity compared to the intensity of the electron beam.

The electron beam is characterized by low emittance, which is a property of charged particle beams that measures the averaged spread of the beam in momentum and position phase-space. Low emittance beams are composed by particles with nearly the same momentum and confined in a small space, hence they have high probability to interact resulting in high luminosity. The emittance of the positron beam at its production is much higher because of the mechanism used to produce positrons. In order to reduce the emittance of the positron beam before to be stored in the main ring, it is injected in a *damping* ring that reduces the emittance by a factor of 130. After the beam production, the electron beam is accelerated in the LINAC until the energy of $E_{e^-} = 7$ GeV and then it is stored in the High Energy Ring (HER); the positron beam is accelerated in the LINAC until an energy of $E_{e^+} = 4$ GeV and then it is stored in the Low Energy Ring (LER). The HER and the LER collide in the interaction point (IP) inside of the *Belle*II detector. The energy in the CM reached through the collision between electrons and positrons, at which the SuperKEKB collider works is [76]:

$$\sqrt{s} = \sqrt{(p_{e^+} + p_{e^-})^2} \simeq 2\sqrt{E_{e^+}E_{e^-}} \simeq 10.58 \text{ GeV} \tag{2.4}$$

The asymmetric energy of electron and positron beams produces a Lorentz boost $\beta\gamma$ of the CM in the laboratory reference system respect to the CM reference system. The boost allows to measure the decay vertex of B mesons. The entity of the boost is:

$$\beta\gamma = \frac{E_{e^-} - E_{e^+}}{\sqrt{s}} \simeq 0.28 \tag{2.5}$$

A schematic view of the SuperKEKB collider is shown in Figure 2.5.

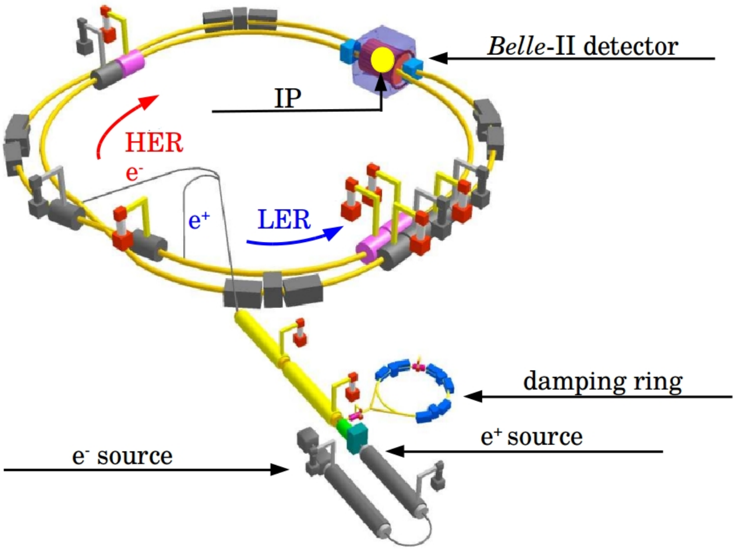

Figure 2.5: Schematic view of the SuperKEKB collider. The image is taken from *Letter of Intent for KEK Super B Factory. Part III: Accelerator Design* [77].

The upgrading of KEKB to SuperKEKB has been done on the same tunnel as KEKB: it is based on the *nano-beam* scheme to achieve higher luminosity with only a moderate increase of beam currents. A schematic representation of the *nano-beam* scheme is shown in Figure 2.6 [76].

The basic idea of the *nano-beam* scheme is to reduce the vertical betatron function β_y^* at the IP in order to improve the instantaneous luminosity $\mathcal{L}$ of the accelerator that depends on β_y^* as $\mathcal{L} \sim \left(\beta_y^*\right)^{-1}$. The betatron function is associated to the transverse size of beams in a certain position x along the trajectory and it is related to the width $\sigma(x)$ and the

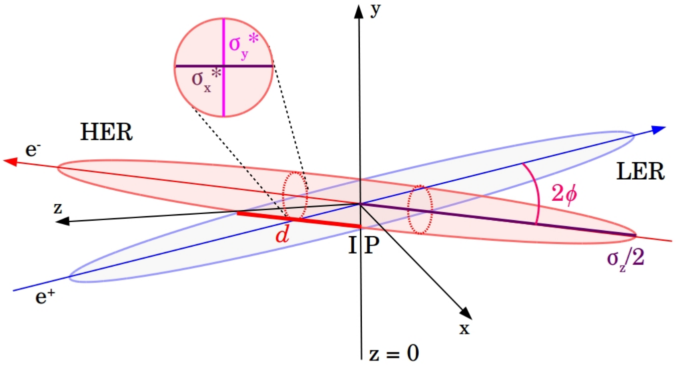

Figure 2.6: Representation of the *nano-beam* scheme; σ_x^* is the horizontal beam size, σ_y^* is the vertical beam size and σ_z is the bunch length; d is the size of the overlap region; ϕ is half of the horizontal crossing angle.

emittance $\epsilon(x)$ of the beam in the position x.
The reduction of β_y^* is possible minimizing the size of the overlapped region d of the HER and LER beams that limits the minimum value of β_y^*. The overlap region d depends on the angle ϕ and on the horizontal size of the beam σ_x^* as shown in equation 2.6 [76].

$$d \cdot sin(2\phi) = 2\sigma_x^* \rightarrow d \simeq \frac{\sigma_x^*}{\phi} \tag{2.6}$$

Assuming flat beams, the expression of the instantaneous luminosity is [76]:

$$\mathcal{L} = \frac{\gamma_\pm}{2er_e}\left(1 + \frac{\sigma_y^*}{\sigma_x^*}\right)\frac{I_\pm \xi_{y\pm}}{\beta_{y\pm}^*}\frac{R_L}{R_{\xi_y}} \tag{2.7}$$

where $+$ and $-$ subscripts are respectively for the LER and for the HER, γ is the Lorentz factor, e is the electron charge, r_e is the electron classical radius, I is the total beam current, $\xi_{y\pm}$ is the vertical-beam parameter and β_y^* is the vertical betatron function. The R_L and R_{ξ_y} parameters are reduction factors for the luminosity and the vertical beam-beam parameter.

The ratio R_L/R_{ξ_y} is of the order of 1, so the most relevant parameters in the luminosity definition are the total current of the beams $I_\pm$, the vertical beam-beam parameter $\xi_{y\pm}$ and the betatron function $\beta_{y\pm}^*$. The beam-beam parameter quantifies the strength of the interaction between the beams and a higher value of this parameter is related to a higher value of the luminosity. The tuning of these parameters allows to achieve the luminosity goal of SuperKEKB that is 40 times higher than the luminosity peak achieved by KEKB: $\mathcal{L} = 8 \cdot 10^{35}$ cm^{-2}s^{-1}. The main machine parameters of the three B-factories colliders are reported in Table 2.2 [76, 74].
In SuperKEKB the boost is reduced with respect to KEKB to improve the luminosity of the accelerator and the decay length of B mesons varies from ∼200 μm to ∼130 μm. The reduction the decay length is compensated by reducing the distance of the vertex detector from the interaction point and by introducing a pixel detector that improves the vertex resolution.
The *Belle*II experiment has two data taking period called *Phase*-2 and *Phase-3*.

Parameters		Units	PEP-II Achieved (LER/HER)	KEKB Achieved (LER/HER)	SuperKEKB (LER/HER)
Beam Energy	E	GeV	3.1/9	3.5/8	4/7
Beam Current	I	A	2.7/1.8	1.6/1.2	3.6/2.62
Beam sizes at the IP	σ_x^*	μm	140	80	10.2/11.2
	σ_y^*	μm	3	1	0.048/0.062
	σ_z	mm	8.5	5	6/5
Lorentz boost factor	$\beta\gamma$		0.56	0.43	0.28
Number of bunches	N_b		1732	1584	2503
Beam crossing angle	2ϕ	mrad	0	22	83
Beam-beam parameter	ξ_y^*			0.129/0.090	0.090/0.088
Horizontal emittance	ϵ_x	nm			3.2/5.1
Emittance ratio	ϵ_y/ϵ_x	%			0.27/0.25
Luminosity	$\mathcal{L}(\cdot 10^{34})$	cm^{-2}s^{-1}	1.2	2.11	80

Table 2.2: The main machine parameters achieved by PEP-II and KEKB at the end of their activity compared to those chosen for SuperKEKB in order to achieve the luminosity goal.

Phase-2, started in February 2018 and ended in July 2018, has been a test bench in preparation for *Phase*-3. It has been dedicated to the study of the response of the *Belle*II detector, described in Chapter 3, and of the accelerator. This phase was relevant also for the tuning of the machine parameters in order to reach the design luminosity. In this phase the vertex detector was not installed inside *Belle*II, instead the BEAST detector, which contain a sector of the vertex detector was installed. The BEAST detector is composed by radiation monitors and it is used to study the machine backgrounds levels that could damage the vertex detector in the physics run. A sample of 505 pb^{-1} of data at the $\Upsilon(4S)$ peak has been collected and it has been used to measure the luminosity reached, to validate the simulations through the comparison between data and Monte Carlo samples, to calibrate the individual sub-detectors in order to find the right values of the mass of particles and to perform material mapping. In particular the *Phase*-2 has been very important to learn how to operate the whole machine, to better understand the problems to be faced in future, and for the commissioning of the sub-detectors for *Phase*-3.

The data sample collected during the *Phase*-2 can also used also to do initial physics analysis, in particular to do rediscovery of well known particles. Since the vertexing system is not fully installed and the data sample size during this period it is not possible to do full studies on B-mesons, however collected data can be used to do *dark sector* analyses, which do not require the vertexing system and can be done also with low statistics.

Phase-3 will start at the beginning of 2019. In this phase the whole detector will be installed and thanks to the complete vertex detector will be possible to do flavour physics analysis. The target integrated luminosity, expected by 2025, is of $\mathcal{L}_{int} = 50$ ab^{-1}: fifty times the total integrated luminosity collected by *BABAR* and *Belle*. At least 70% of the total data set is estimated that will be on-peak at the energy of the $\Upsilon(4S)$ [76].

Figure 2.7 shows the schedule for the luminosity of SuperKEKB from first collisions occurred during the *Phase*-2 of the experiment, in the night between the 25th and the 26th of April 2018, until reaching the peak luminosity goal in 2022 during the *Phase*-3 of the experiment [76], and the target integrated luminosity in 2025.

In Table 2.3 are reported the data sets size achieved by *BABAR* and *Belle* experiments[74][76].

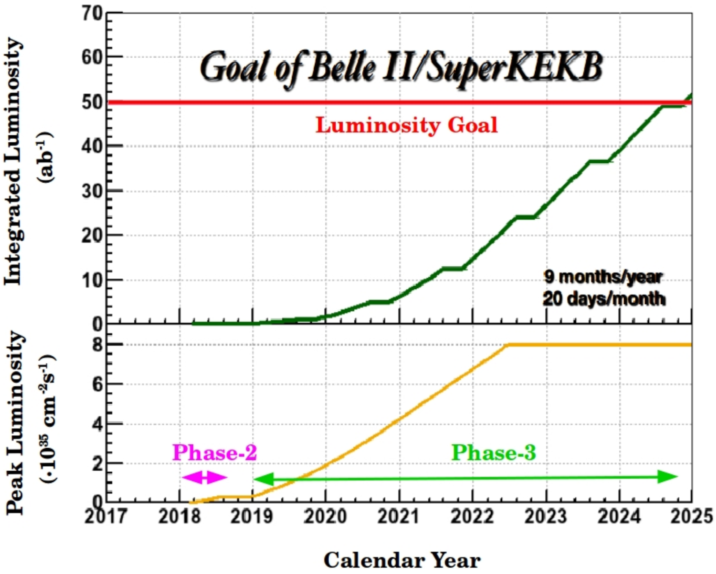

Figure 2.7: SuperKEKB luminosity projection. On June 20, 2018, during the *Phase*-2 of the experiment, the luminosity $\mathcal{L} = 3.04 \cdot 10^{33}\text{cm}^{-2}\text{s}^{-1}$ has been achieved.

		On-Resonance		Off-Resonance
		$\mathcal{L}_{int}$ (fb^{-1})	$\Upsilon(4S)$	$\mathcal{L}_{int}$ (fb^{-1})
BABAR and *Belle*		424.2	$(471.0 \pm 2.8) \cdot 10^6$	43.9
Belle	SVD-1	140	$(152 \pm 1) \cdot 10^6$	15.6
	SVD-2	571	$(620 \pm 9) \cdot 10^6$	73.8

Table 2.3: Summary of the time integrated luminosity on- and off-peak at the energy of the $\Upsilon(4S)$ achieved by *BABAR* and *Belle* experiments, and of the number of $\Upsilon(4S)$ particles collected by the two experiments.

Chapter 3

The *Belle*II detector

The *Belle*II detector is designed to maintain high performances in an environment characterized by high background levels, with an improvement in luminosity and precision with respect to the *Belle* detector. Because of higher currents, smaller beam size and modified IR, the background hit rate is estimated to be twenty times higher and the event hit rate is estimated to be fifty times higher with respect to those of *Belle*. The main components of the *Belle*II detector are listed here and described in more detail in the following sections:

- two layers of silicon *Pixel Detector* (PXD), just outside the beam pipe. The PXD is based on DEPFET technology and it has an excellent spatial resolution that improves the vertex resolution;

- a *Silicon Vertex Detector* (SVD) based on double-sided silicon strip sensors used for the reconstruction of charged particles, which occupies a larger volume and is positioned closer to the *Interaction Point* compared to the *Belle* SVD: this improves the efficiency of event reconstruction for events as $K_S \to \pi^+\pi^-$. SVD signals are read by APV25 chips that are faster than chips used in the *Belle* detector in order to face the high hit rate;

- an axial-stereo *Central Drift Chamber* (CDC) that occupies a larger volume and has a higher granularity than the *Belle* CDC;

- a *Particle Identification* (PID) systems based on Cherenkov effect, with the TOP detector located in the barrel region and the ARICH detector located in the forward endcap region, are completely new and have a fast readout system. They especially improve the separation efficiency between pions and kaons;

- an electromagnetic calorimeter (ECL) that reuses the CsI(Tl) crystals from *Belle*, but it has a faster readout electronics that reduces the occupancy and pileup. This is very important for missing energy studies;

- a K_L and μ detector (KLM) composed of resistive plate chambers (RPCs) in the outermost layers of the barrel region and of scintillators, which are read by silicon photomultipliers (SiPM), in the innermost layers of the barrel region and in the endcaps;

- a fast readout electronics of the sub-detectors and a fast trigger system able to face the high hit rate.

In this chapter each sub-detector and the trigger system are described. The method developed for the calibration of the algorithm used by SVD to estimate the *hit time* of the individual particle on the individual sensor is described in Chapter 4. Finally some details of the software framework will also be given. The full detector is described in detail in Reference [76].
The schematic view of the detector is shown in Figure 3.2, while the Figure 3.1 shows the coordinate system of *Belle*II.

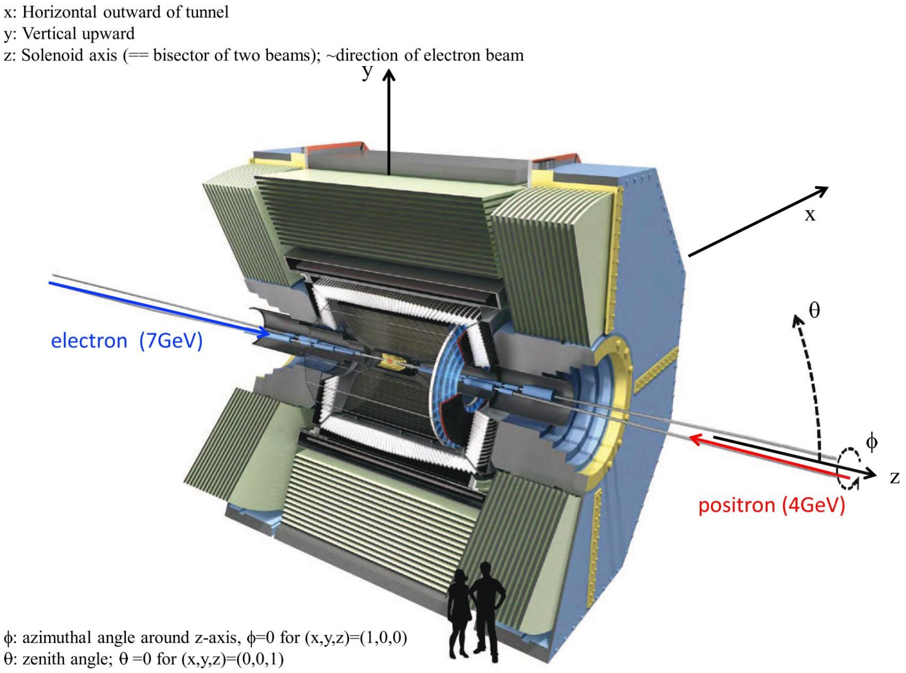

Figure 3.1: 3D representation of the *Belle*II detector. The coordinate system is shown: the x coordinate is directed opposite compared to the center of the accelerator, the y coordinate is directed upward and the z coordinate is the bisector of the two beams and is directed towards the forward region, which is defined by the Lorentz boost of the CM (the IP is in $x = y = z = 0$, $+z$ is the forward region of the detector, while $-z$ is the backward region of the detector). The θ angle is the polar angle and $\theta = 0$ for $(x, y, z) = (0, 0, 1)$, while ϕ is the azimuthal angle and $\phi = 0$ for $(x, y, z) = (1, 0, 0)$. The image is taken from [78].

In Table 3.1, the performances of the detector discussed in the following sections are summarized.

	*Belle*II detector performances
B vertex reconstruction	$\sigma_z = 26~\mu$m
Tracking	$\sigma_{pt}/pt = 0.0011pt[\text{GeV}/c] \oplus 0.0025/\beta$
K/π ID	$\epsilon_K \simeq 0.90$ with pion fake rate $\epsilon_\pi \simeq 0.04$ for $p = 2$ GeV/c tracks
Calorimeter resolution	$\sigma_E/E = 7.7\%$ at 0.1 GeV and 2.25% at 1 GeV
Muon ID	$\epsilon_\mu = 0.92 - 0.98$, fake rate $\epsilon = 0.02 - 0.06$ for $p > 1$ GeV/c
L1 Trigger	30 kHz max average rate, with efficiency for hadronic events $\epsilon_{hadron} \simeq 1$
Data Acquisition System (DAQ)	<3% dead time at 30 kHz L1 rate

Table 3.1: Summary table of the detector performances. The table has been taken from Reference [79].

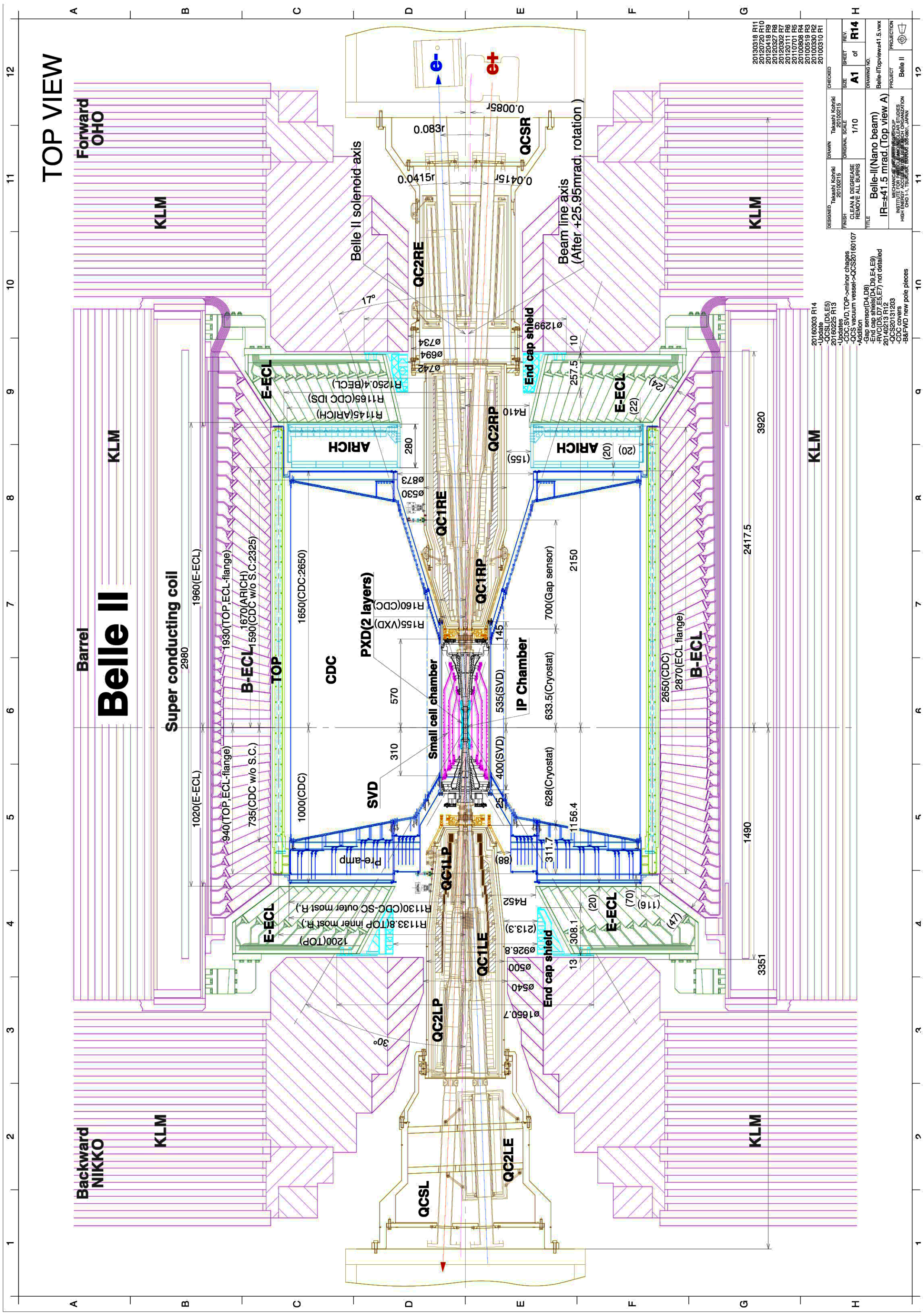

Figure 3.2: Side section of the *Belle*II detector. The image is taken from Reference [79].

3.1 Pixel Vertex Detector: PXD

Because of the higher beam background levels of SuperKEKB expected at the nominal luminosity, the detectors close to the beam pipe suffer very high hit rates. In *Belle*II the innermost layers of the tracking system are closer to the IP than the *Belle* innermost vertex detector, in order to compensate a smaller Lorentz boost factor ($\beta\gamma = 0.28$) and maintain a good vertex resolution. The background levels increase as the inverse of the distance squared and in these conditions, the silicon strip-based vertex detectors are not usable because of the large occupancy that does not make possible the vertex reconstruction of B meson decay vertices. The PXD can cope with higher background rate keeping a lower occupancy, because of the higher granularity.

The *Belle*II PXD is a barrel system consisting of two cylindrical layers of active pixel sensors. The two layers are coaxial with the beam pipe and located at 14 mm and 22 mm from the IP, respectively. The innermost layer is composed by 8 planar modules, called ladders, and the outermost layer is composed by 12 ladders. The ladders overlap in the ϕ direction, where ϕ is the azimuthal angle, in such a way that the active pixel area of one of the two layers covers the insensitive area of the other layer. The geometric acceptance covered by the sensitive sensors is in the range $17^{\mathrm{o}} \lesssim \theta \lesssim 155^{\mathrm{o}}$, where θ is the polar angle. The PXD is composed of around 8 million pixels in total, organized into arrays. In order to improve the resolution on the position of individual hits, which is limited by multiple scattering, a very thin technology is required: the sensitive area of each PXD sensor is 75 μm thick, while the mechanical supports are 525 μm thick, in order to satisfy the thickness required to reduce the material budget. The size of the pixel surface is 50×50 $\mu\mathrm{m}^2$ and 50×75 $\mu\mathrm{m}^2$, respectively in the innermost and outermost layers, and it is determined by the requirements on the vertex resolution, which should be larger than 20 μm.

The readout system of the PXD is located at both ends of the cylindrical structure of the PXD, and it exploits high level of parallelization in order to guarantee a readout time of 20 μs for the entire matrix of pixels.

The sensors are mounted on a supporting structure that can slide on the beam pipe in order to compensate the thermal expansion of the beam pipe and of its support. A schematic view of the PXD is shown in Figure 3.3.

PXD sensors are based on the DEPleted Field Effect Transistor (DEPFET) technology. A DEPFET device is a semiconductor-based device that detects and amplifies signals. Because it works also as amplifier, it is a thin device that does not need other devices for signal amplification. A DEPFET is also a low power device and the readout electronic, which needs of a cooling system, is located out of the geometric acceptance of the detector. For all this reason, DEPFET technology is excellent to minimize the material budget. A section of a DEPFET device is shown in Figure 3.4. The basic idea of the DEPFET is the fully depletion of the n-type substrate applying a high negative tension to the p^+ contact in the backside of the device. In this way a potential well, in which the potential has its minimum, is created and it becomes an accumulation region for electrons inside the device. A particle crossing the device produces electron-hole (e-h) pairs: electrons are collected very quickly in the potential minimum, called *internal gate*, while holes move towards the p^+ back contact. When the transistor is on, being the *internal gate* capacitively coupled with the *gate*, the charge into the *internal gate* modulates the *drain* current that circulates through the pMOSFET towards the *source* contact.

In order to reset the sensor, a n^+ doped contact, called *clear*, is put to a positive potential:

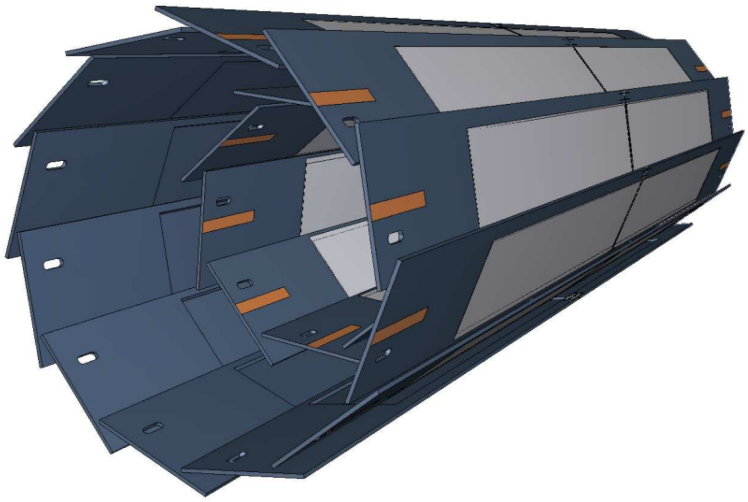

Figure 3.3: 3D representation of the PXD that shows the geometric arrangement of the sensors. The light gray areas are the DEPFET sensitive ones, 50 μm thick, that cover the whole geometric acceptance. The dark blue area are the insensitive areas of the modules. The total length of the outermost modules is 174 mm.

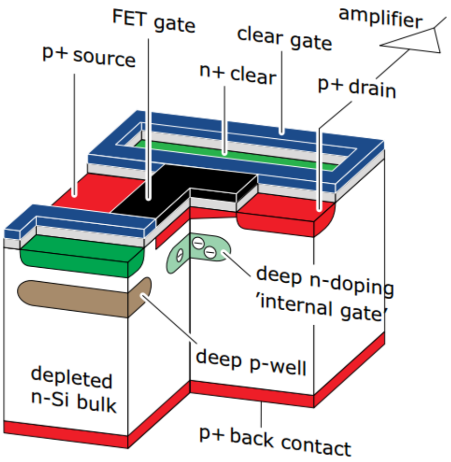

Figure 3.4: Schematic view of a section of a DEPFET device. It is composed by p-channel Metal Oxyde Semiconductor Field Effect Transistor (pMOSFET) installed onto a n doped silicon substrate, called *bulk*. A pMOSFET is equipped with four contacts: *source*, *gate*, *drain* and *bulk*. The *bulk* is connected to the *source* contact: they are at the same potential. In the backside of the device there is p^+ contact to which is possible to apply a high voltage in order to fully deplete the n substrate. Just below the *gate* there is a n doped *internal gate*. It is a potential well that works as a region of accumulation for the negative charges. The distance between the *gate* and the *internal gate* is 1 μm. Above the substrate there is a n^+ contact, called *clear*, that is used to empty the *internal gate*. The *clear gate* is a polycrystalline silicon structure. The image has been taken from Reference [76].

it attracts the accumulated electrons in the *internal gate* emptying it. A polycrystalline silicon additional structure called *clear gate* modulates the potential difference between the *clear* and the *internal gate*.

The DEPFET readout is relatively slow, using a rolling shutter system that requires 20 μs for a full readout. In spite of the high granularity, occupancy can reach 3%, leading to an amount of data coming from the PXD higher than the amount of data accepted by the data-acquisition system. In order to reduce the amount of data from the PXD, the *Region-Of-Interest* (ROIs) are defined onto the PXD sensors. A preliminary reconstruction of tracks is done using the SVD and the CDC only, those tracks are then extrapolated onto the PXD sensors. The extrapolation of the tracks on sensors defines the ROIs, which are rectangular regions whose size is defined by the statistical and systematic uncertainties on the position of the track.

3.2 Silicon Vertex Detector: SVD

SVD, together with the PXD, makes up the vertex detector (VXD) of *Belle*II. The SVD is composed by four layers numbered from 3 to 6 and respectively placed at distance of 3.9 cm, 8.0 cm, 10.4 cm and 13.5 cm from the IP. Each layer consists of a different number of modules, called ladders, arranged around the IP to form a nearly cylindrical geometry: layers 3-6 are composed respectively by 7, 10, 12 and 16 ladders that are supported by carbon fiber ribs. Each ladder is equipped with Double-Sided Silicon Strip Detectors (DSSD), described in section 3.2.1. The geometrical acceptance covered by SVD goes from $\theta = 17^o$, in the forward region, to $\theta = 150^o$, in the backward region. Ladders are equipped with three different kind of sensors: each ladder of layer 3 consists of two equal rectangular sensors of size 123 mm $\times$ 38 mm, while each ladder of layers 4, 5 and 6 has respectively 2, 3, 4 rectangular sensors of size 123 mm $\times$ 58 mm and one trapezoidal sensor in the forward region. Trapezoidal sensors are arranged in the forward region and are slanted of an appropriate angle with respect to the other sensors in order to improve the angular acceptance and optimize the incident angle on the sensor of particles coming from the IP. Rectangular sensors have a thickness of 320 μm while trapezoidal sensor have a thickness of 300 μm. Figure 3.5 shows a schematic view of the SVD.

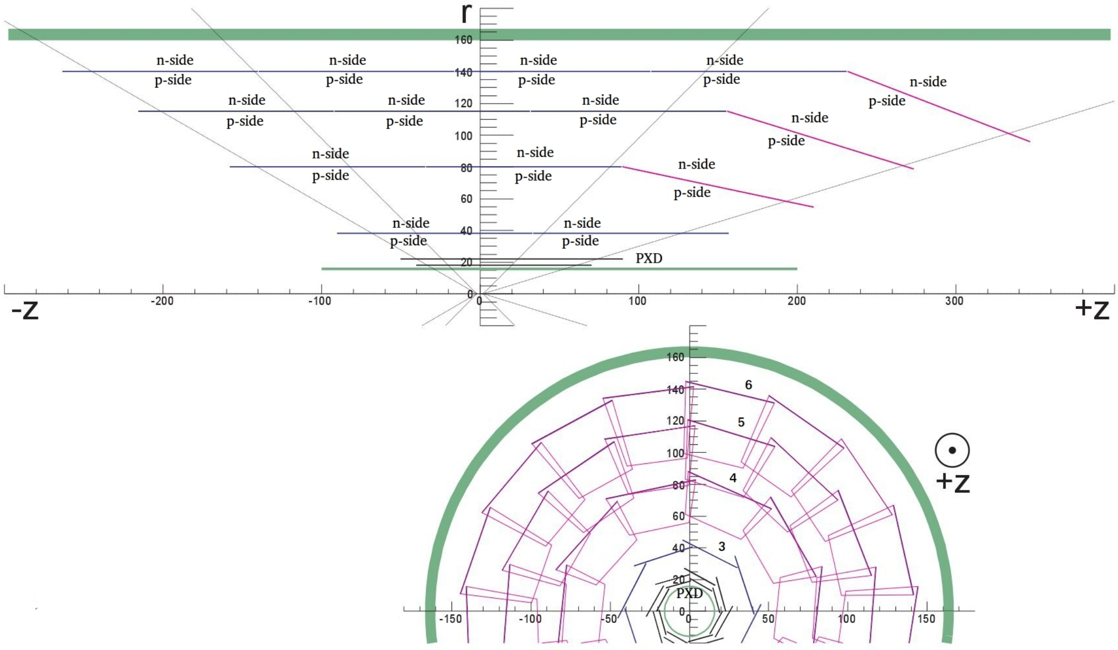

Figure 3.5: Schematic view of SVD in the r-z plane and r-ϕ projection showing the different sensor composition in each layer. In r-ϕ view the two layers of PXD are shown also. The image has been taken from *The Belle*II *Technical Design Report* [76].

3.2.1 Working principle of DSSD

The main purpose of SVD, together with PXD, is to measure with extreme precision the tracks near the IP and to reconstruct the decay vertices of B mesons, D mesons and τ leptons. SVD is also able to reconstruct K_S mesons that decays outside of the PXD volume. In order to reconstruct tracks characterized by low transverse momentum, which are affected particularly by multiple scattering, it is required to maintain a low material budget giving a 2-dimensional information. DSSD sensors satisfy both requirements: they provide a very precise measurement of the position of charged particles on sensors and they allow to maintain a low material budget. DSSD sensors are based on the working principle of p-n junctions.

When a charged particle crosses the sensor, it generates electron-holes (e-h) pairs interacting with the material of the sensor. If an external electric field is applied, the e-h pairs move inside the sensor and the current due to the motion of e-h pairs can be detected. The number of e-h pairs generated in the material by a charged particle can be estimated considering the value of mean energy loss $dE/dx|_{mean}$ by a minimum ionizing particle (MIP), the thickness of the sensor d_s and the energy required to create an e-h pair E_{e-h}. Assuming $d_s = 300$ μm and by considering that for silicon $dE/dx|_{mean} = 388$ eVμm^{-1} and $E_{e-h} = 3.63$ eV, the number of e-h pairs generated is:

$$N_{e-h} = \frac{dE/dx|_{mean} \cdot d_s}{E_{e-h}} \simeq 3.2 \cdot 10^4 \tag{3.1}$$

The number of intrinsic thermal equilibrium e-h pairs in a silicon sensor at room temperature, can be estimated considering the density of intrinsic charge carriers n_i, $1.45 \cdot 10^{10}$ cm^{-3} for silicon, a sensor electrode with an area $A_s = 100$ μm $\times$ 10 cm $= 0.1$ cm^2 and $d_s = 300$ μm thick:

$$N^i_{e-h} = n_i \cdot A_s \cdot d_s \simeq 4.35 \cdot 10^7 \tag{3.2}$$

The number of intrinsic e-h pairs N^i_{e-h} is four order of magnitude higher than the number of e-h pairs generated by a MIP crossing the sensor: in order to detect the small signal of a particle crossing the sensor, the number of intrinsic e-h pairs must be reduced drastically and the best way to do it is using a p-n depleted junction.

A p-n junction is an interface between two oppositely doped semiconductors. In the n-doped semiconductor there is an excess of electrons while in the p-doped semiconductor there is an excess of holes: the region between the two semiconductors forms a depletion region. Because of the different doping concentration, electron in excess in the n-doped semiconductor diffuse inside the p-doped semiconductor and recombine with holes and vice versa. For this reason donor and acceptor atoms used for doping are not compensated anymore by the free charge carriers and a potential difference is generated by the not compensated atoms. The potential difference generates an electric field that stops the diffusion motion of free charges: this leads to a limited depletion region in which the p-n junction is free of charge carriers. In DSSD sensors an asymmetric p-n junction is created introducing a semiconductor highly p-doped on a n-doped substrate, called *bulk*. The depletion region is larger in the bulk lightly doped and is extended applying a reverse bias voltage V_b that allows to remove intrinsic charge carriers from the *bulk*. The e-h pairs generated by a particle crossing the depleted bulk in the sensor drift towards the electrodes under the effect of the applied reverse bias V_b. The motion of charge carriers inside the *bulk* induce an electric current on the electrodes [80] that is the signal of response of the sensor at the passage of the particle. When electrodes are segmented they provide also spatial information about the passage of the particle: sensor elements closest to the point of production of e-h pairs will collect most of the induced signal with respect to the other neighboring sensor elements, which may collect a small fraction of the induced signal. The SVD sensors are segmented with long, thin sensor elements called strips that extend the full length, or width, of the sensor. Usually strips are a few tens of μm wide and they can be spaced by a few tens of μm to hundreds of μm: the separation between strips is called *pitch*. The strips allow to measure the position of the crossing ionizing particle, providing a one-dimensional measurement of the position, if the segmentation of the electrodes is done only on one side of the sensor, or a two-dimensional measurement of the position, if electrodes are segmented in both sides of the sensor. The latter case is that of DSSD sensors, whose structure allow to use the same material budget of a common silicon strip detector: with p^+ implemented strips on one side and orthogonal n^+ implemented strips on the opposite side of the sensor. Aluminium strips are used for the readout of electrode strips and are isolated from the silicon substrate by a $\mathrm{SiO_2}$ layer, in order to create a decoupling capacity and avoid leakage currents entering the preamplifier channel connected to each sensor strip. Figure 3.6 shows a schematic view of the working principle of a DSSD sensor.

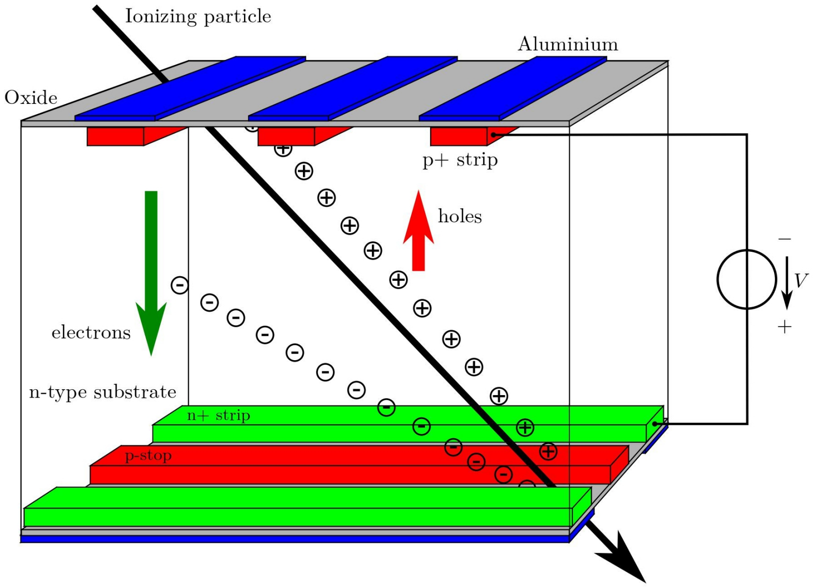

Figure 3.6: Schematic view of a DSSD device, which shows the working principle. A charged particle crosses the sensor and generates e-h pairs through ionization. The e-h pairs drift towards the electrodes because of the inverse potential difference applied between implanted p-type and n-type strips. The drifting motion induce a signal on sensitive strips. In the figure, the *p-stop* between the two n-doped strips is shown too. The image has been taken from [81]

The $\mathrm{SiO_2}$ layer contains positive oxide charges, which are charges trapped in the oxide layer during the fabrication, that attract electrons generating an accumulation region. Electrons form a layer of negative charges shorting the n-doped electrode strips. The accumulation region can be interrupted introducing p-doped strips, called *p-stops*, between the n-doped electrode strips: *p-stops* introduce p-n junctions that drives electrons away from the accumulation region. Figure 3.6 shows the *p-stop* between two n-type strips.

To identify strips that are crossed from particle a given cut is applied on their signal Signal-to-Noise-Ratio (SNR) to perform the zero suppression and after that identify the

position of the particle crossing. The position of the particle crossing the sensor, x_p, is calculated as the weighted mean of the position of the strips in which a signal is induced, using as weight with the intensity of the signal induced on the individual strip.
If the signal is induced in only one strip, the resolution on the position is simply $d_{pitch}/\sqrt{12}$, where d_{pitch} is the value of the *pitch*. If the signal is induced in more than one strip, to form a cluster, the resolution on the position in determined by the SNR as well as by d_{pitch}.
A cluster is a group of strips in which at least one strip is characterized by SNR ≥ 5 and the adjacent strips have SNR ≥ 3. The strip with the higher SNR is called *seed* of the cluster.
Strips of the p-side are parallel to the z axis, so they measure the r-ϕ coordinate (called U in the local sensor coordinate system), while n-side strips are perpendicular to the z axis, so they measure the z coordinate (called V). The most relevant features of SVD are listed in Table 3.2.

layer	Distance from the IP	θ_{fwd}	Nº of ladders/ layer	Nº of DSSD/ ladder	Nº of Origami/ ladder	Nº of APV25/ DSSD
3	3.9 cm	0^o	7	2	0	12
4	8 cm	11.9^o	10	3	1	10
5	10.4 cm	17.2^o	12	4	2	10
6	13.5 cm	21.1^o	16	5	3	10

	sensor type	number of strip side p/n	strip *pitch* side p/n (μm)	active area (mm^2)
3	rectangular	768/768	50/160	4738
4,5,6	rectangular	768/512	75/240	7030
4,5,6 fwd	trapezoidal	768/512	50-75/240	5893

Table 3.2: Summary table of the main features of SVD described in the text. The main features of the ladders are reported in the upper table, while the main features of the sensors are reported in the lower table. Data have been taken from *The Belle*II *Technical Design Report.* [76].

3.2.2 Ladder structures and readout electronics

The readout electronics is based on APV25 chips [82], each of which reads 128 strips. The APV25 chip contains a low-noise front-end preamplifier followed by a shaper with a shaping time of 50 ns. In ladders of layers 4, 5, and 6 each sensor uses 10 APV25 chips, 6 are for the readout of the p-side and 4 are for the readout of the n-side of the sensors. The ladders of layer 3 use 12 APV25 chips for each sensor, 6 on the readout of the p-side and 6 on the readout of the n-side. The APV25 chips in layer 3 and on the forward and backward sensors of the layers 4, 5, 6 are mounted on readout boards called *Hybrid Sandwich* (HS) boards positioned at the end of the sensor outside the active area. For what concerns the sensors disposed in the central part of the ladders, the *Origami-chip-on-sensor* concept is applied for the readout electronic. It is a concept based on the use of flexible circuits, called *Origami*, on which APV25 chips for the readout are glued. The *Origami* circuits are separated from the surface of the sensor by a layer of AIREX foam 1 mm thick that acts as a thermal and electrical isolator to reduce crosstalk effects and heat transfer from the chips to the sensor. Strips in the upperside of the sensor are connected to the APV25 chips using planar *fan-outs*, while strips in the bottomside are connected to the APV25 chips located in the upperside using flexible *pitch adapter* (PA) wrapped around the edge

of the sensor (as in *Origami*). The advantages of this manufactured design is to allow all chips to be aligned only on one side of the sensor and then to use only one cooling pipe to cool all APV25 chips, minimizing the material budget. The cooling system of APV25 uses CO_2 that flows inside cooling pipes 100 μm thick: the total amount of material budget is around 0.6 X_0, where X_0 is the radiation length.
Forward and backward sensors of layers 4, 5 and 6 and the two sensors for each layer 3 ladder are connected to APV25 chips through a flexible circuit PA that carries the signal from strips to the APV25 chips located on the HS at the end of the sensors. The APV25 chips of layer 3 are cooled through the cooling system of the end-ring, which provide the interface between ladders and the whole support structure of the SVD. The PAs and *Origami* are composed by kapton layers in which the copper wires that connect the sensors with the APV25s are arranged. Four different types of PAs, with different sizes and different connections, are used depending on the module (forward or backward) and on the side (n or p). Figure 3.7 shows the *Origami-chip-on-sensor* concept.

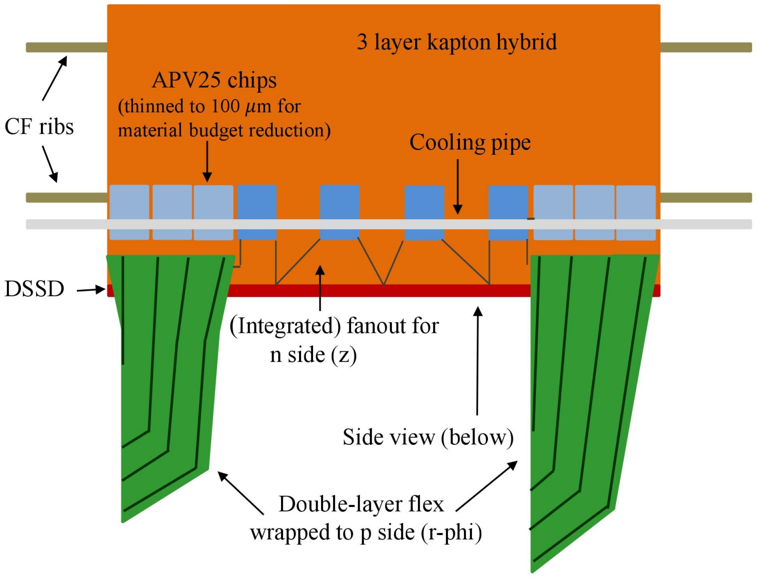

(a) Top view

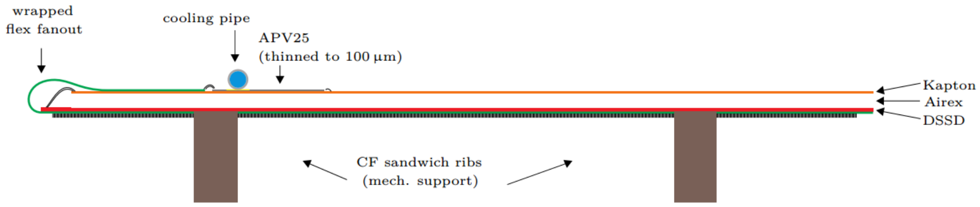

(b) Side view

Figure 3.7: The *Origami-chip-on-sensor* concept: Top view (a), cross section (b).

The ladders of layer 3 have a simpler geometry with sensors directly connected to HS boards located at the end of each sensor.
The signal waveform of each strip is sampled by the APV25 chips, in *Belle*II it is operated with a sampling frequency of 31.8 MHz. Two types of sampling are possible: 6 samples or 3 samples. The baseline plan is to use 6 samples, but in case of high trigger rates it may be necessary to use 3 samples to reduce the amount of data produced by the chips and reduce dead time, since 3 samples close to the peak of the waveform are enough to reconstruct the whole waveform itself. The samples are recorded in a buffer that is composed by 192 cells of which 160 are writable cells and the signal waveform is sampled every $t_S \simeq 31.45$

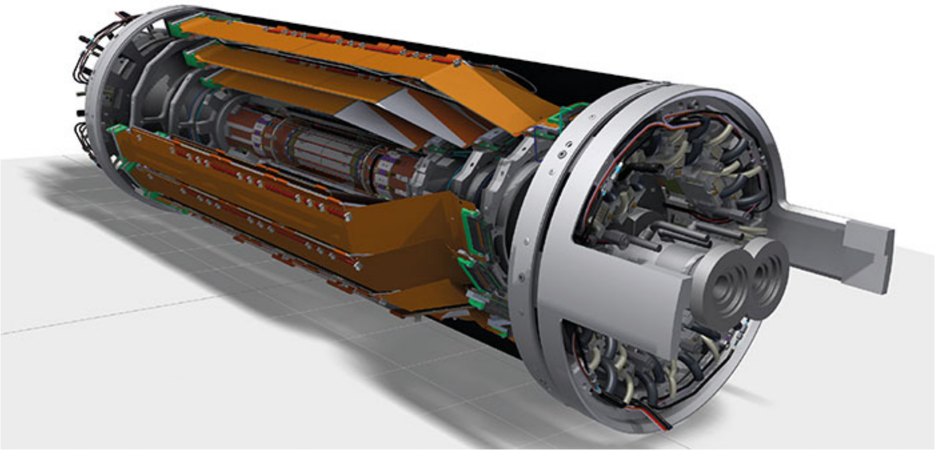

Figure 3.8: The 3-dimensional representation of the SVD in which the structural support and the two PXD layers inside are shown.

ns. When an event is readout the APV samples are digitized by a *Fast Analog-to-Digital Converter* (FADC) synchronized with the APV clock.

The *event time* provided by the L1 trigger is delayed by a time Δt (latency) with respect to the physics event, and it is therefore necessary to start to read the cells of the buffer that has been registered a Δt time before the L1 trigger. Currently the value of the *latency* is set to $\Delta t = 158 \cdot 31.45$ ns ≈ 4.97 μs. The arrival time of the L1 Trigger is registered by the FADC and peripheral SVD electronics with a clock frequency that is four time higher than the APV25 clock frequency and this allow to know the event time with a better precision. FADC provides the quarter of the 31.45 ns in which the trigger sent a signal, i.e. a time window of ~ 8 ns called *trigger bin* (TB).

The FADC converts the analog signal to a 10-bit number and performs common mode subtraction, pedestal subtraction, and zero-suppression, which consists of rejecting the strips with SNR under a given threshold.

More details on the readout electronics and the online processing of signal output of SVD are in *The Belle*II *Technical Design Report* [76].

Figure 3.8 shows a 3-dimensional representation of the SVD, with the two PXD layers inside it.

3.2.3 VXD *Phase*-2 geometry

In *Phase*-2 only two ladders of the PXD and four ladders of the SVD were installed, one for each layer, mounted in a mechanical structure called *cartridge*. The SVD *cartridge* is located at $\phi = 0$, i.e. in opposite direction compared to center of the ring. Figure 3.9 shows the geometric arrangement of the SVD during the *Phase*-2.

Around the IP other detectors are arranged to monitor the levels of radiation near the IP and understand if those levels are safe for the PXD and for the SVD. Through the information provided by them and by radiation monitoring diamonds, it is possible to characterize the background. The detectors for radiation levels monitoring are:

- FANGS detectors are silicon pixel sensors used to investigate the Synchrotron Radiation and the deposit energy of the background;

- CLAWS are plastic scintillators coupled to SiPM readout used to study the time evolution of the beam injected background and its decay constant;

- PLUME are CMOS monolithic active pixels used to study the spatial distribution and the direction of the beam injected background.

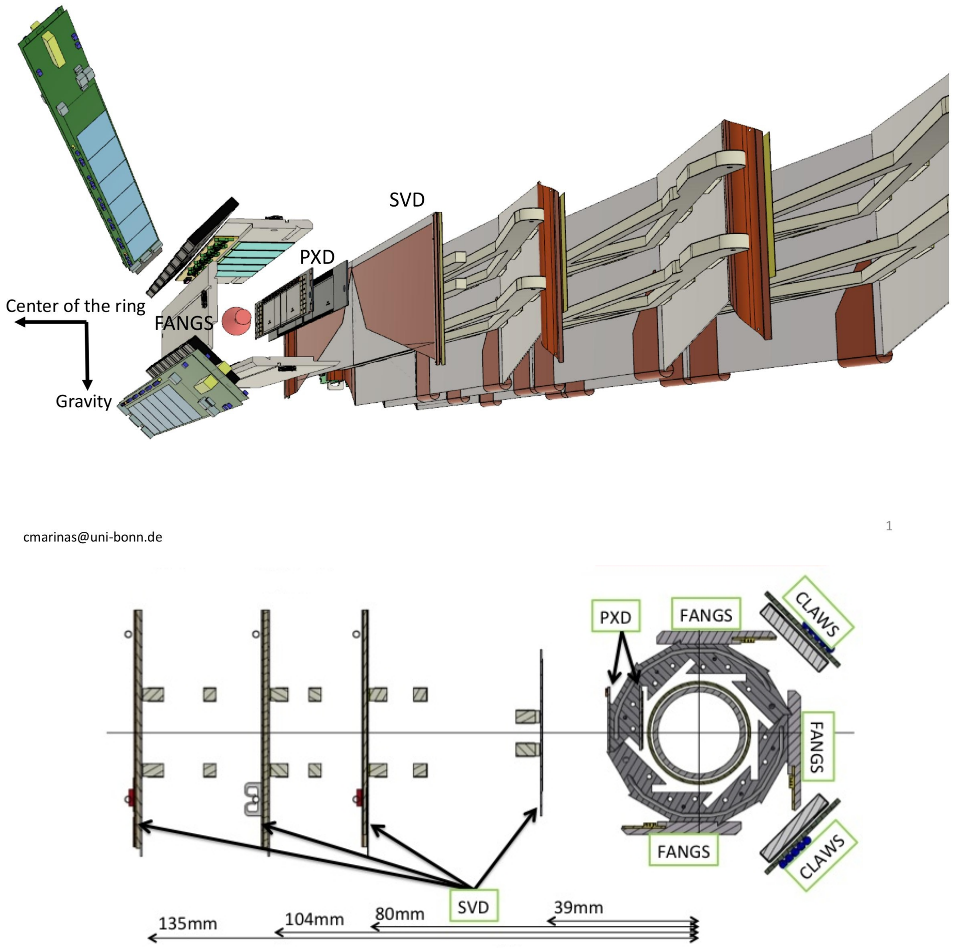

Figure 3.9: Geometry of the VXD in *Phase*-2. Around the IP there are other detectors (FANGS, CLAWS and PLUME) for the measurement of the radiation levels.

The first data collected at *Belle*II during the *Phase*-2 by the SVD subsystem have been analyzed and used to calibrate the estimator of the time at which particles cross the SVD sensors, which is called $\mathcal{COG}$. The method developed for the calibration is described in Chapter 4.

3.3 Central Drift Chamber: CDC

The *Central Drift Chamber* (CDC) performs three important tasks:

- it reconstructs charged particles tracks with a precise measurement of charged particle momenta;
- it provides PID through the information about the particle energy loss, dE/dx, within its gas volume with a high resolution. The dE/dx resolution depends on the incident angle of particles: it is around 12% for particles crossing perpendicularly the CDC;
- it provides 3D trigger information.

A comparison between the main parameters of the CDC of *Belle* and *Belle*II are listed in Table 3.3.

	Units	*Belle*	*Belle*II
Radius of the innermost cylinder	mm	77	160
Radius of the outermost cylinder	mm	880	1130
Radius of the innermost sensitive wire	mm	88	168
Radius of the outermost sensitive wire	mm	863	1111.4
Number of sensitive wires		8400	14336
Gas		He-C_2H_6	
Diameter of sensitive wire		30	

Table 3.3: Some relevant parameters of the CDC of *Belle* and *Belle*II are listed. The largest number of sensitive wires of *Belle*II CDC allows to have a better granularity and a better spatial resolution on the tracks. Respect to the *Belle* CDC, the *Belle*II CDC must face higher levels of background and a higher trigger rate. The higher inner radius allows to avoid the high radiation levels near the IP and provides more space to place the SVD. The values are taken fom *The Belle*II *Technical Design Report* [76].

The CDC is composed by 56 layers of wires divided in 9 superlayers with axial-stereo readout, the 9 superlayers and the configuration of the wires is shown in Figure 3.10, where the axial and the stereo wires are represented respectively in blue and red.

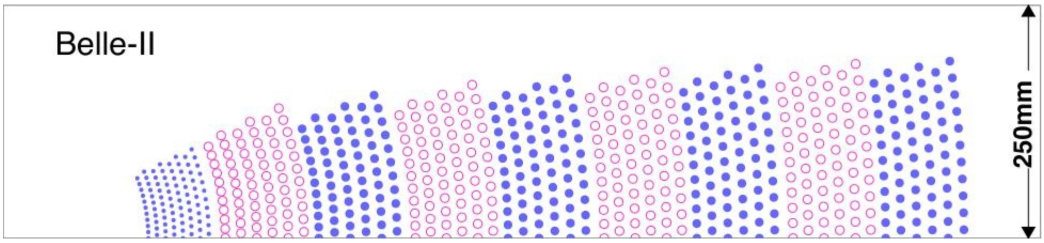

Figure 3.10: The 9 superlayers composing the CDC with the configuration of the wires. The innermost superlayer is composed by two layers while the other eight are composed by 6 layers each. Image taken from Reference [79].

The layers are immersed in a gas, composed of 50% helium and 50% ethan, able to provide a high drift speed. The sense wires are interspaced with aluminium field wires. The configuration of wires and the properties of the gas allow to reduce dead time and handle high trigger rates. The CDC is supported by two carbon-fiber cylindrical supports that end with aluminium endplates.

The geometrical acceptance on the polar angle covered by the CDC goes from $\theta = 17^o$ to $\theta = 150^o$. The measured spatial resolution on the individual hit is around 100 μm.

The readout electronics is composed by 15 thousand channels with a timing resolution of about 1 ns located on the backward side. The forward side used exclusively to connect HV cables.

The main structure of the CDC is shown in Figure 3.11.

3.4 Time Of Propagation counter: TOP

In order to improve the K/π separation capability of the detector and improve the PID, *Belle*II is equipped with Cherenkov effect based detectors.

The TOP detector is composed by quartz radiator and exploits the Cherenkov effect in order to perform PID. In particular it measures the time of propagation of the Cherenkov

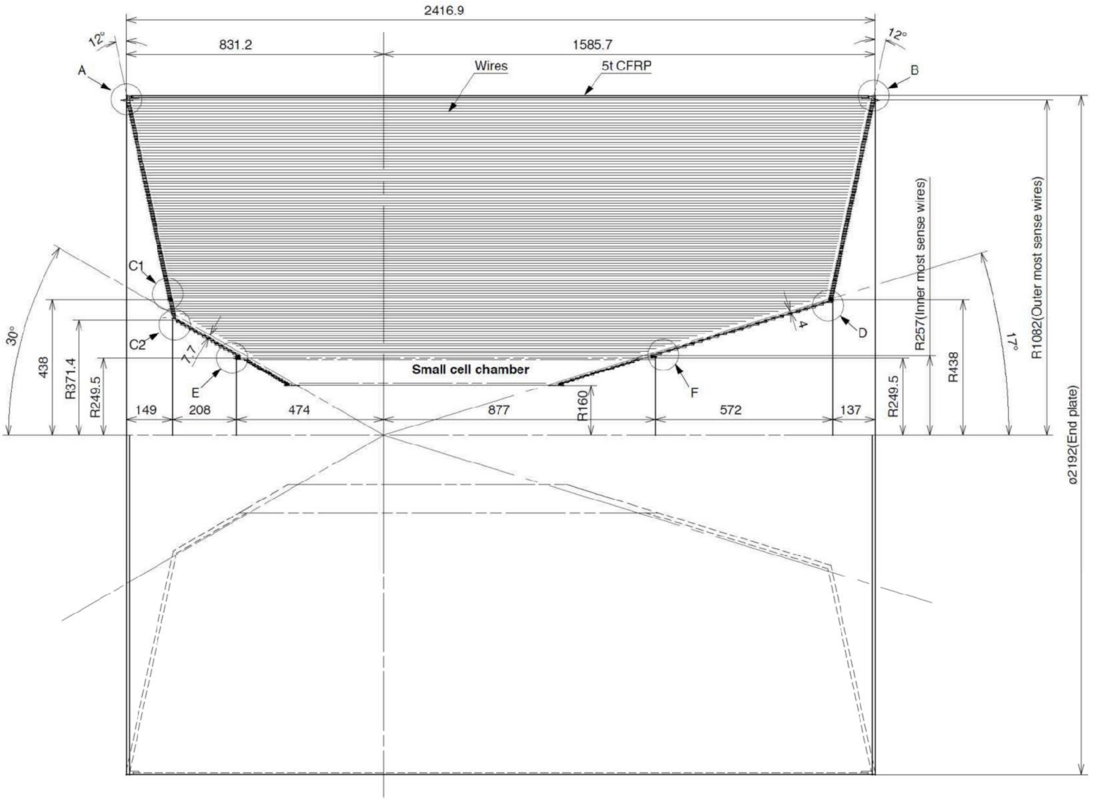

Figure 3.11: Structure of the CDC. The sizes are expressed in mm. The figure is taken from *The Belle*II *Technical Design Report.*

photons that propagates into the quartz radiators. The radiators are composed by a long quartz bar, by micro-channel plate photomultipliers (MCP-PMTs) installed at one of the two final part of the bars and by a spherical focusing mirror on the other final part of the bar. When particles cross the quartz bar they produce Cherenkov photons that are propagated *via* total reflection on the inner walls of the radiator. The direction of Cherenkov photons emitted by particles respect to the direction of the particle momenta is defined by the Cherenkov angle θ_C that characterizes the Cherenkov ring image: the total reflection allows to preserve the Cherenkov ring image. Cherenkov photons are focused and directed towards the MCP-PMTs by the focusing mirror. Before the MCP-PMTs, an expansion prism is installed in order to expand the Cherenkov ring image. Finally the MCP-PMTs measure the time of propagation, t_{TOP}, of the Cherenkov photons and provide information on the arrival (x, y) coordinates of the photons. The Cherenkov ring image is reconstructed from the 3-dimensional information, (x, y, t_{TOP}), provided by the MCP-PMTs. The time resolution can be limited by chromaticity of Cherenkov photons. The focusing mirror minimize the effect of the chromaticity avoiding the dispersion of photons. The Cherenkov ring image is divided in different MPC-PMTs, according with the wavelength of the photons. Figure 3.12 shows a schematic view of the TOP detector and the chromaticity effect.

The TOP counter is installed in the barrel region of the *Belle*II detector between the ECL inner support and the CDC outer cover. It is composed by 16 modules surrounding the CDC, the radius of the TOP is around 1.24 m.
The MCP-PMTs are characterized by a gain of $\sim 10^6$ and by a very fast response. Furthermore they can work inside the 1.5 T magnetic field of *Belle*II. The spatial resolution of the photon detectors is of few mm and the time resolution is lower than 50 ps.

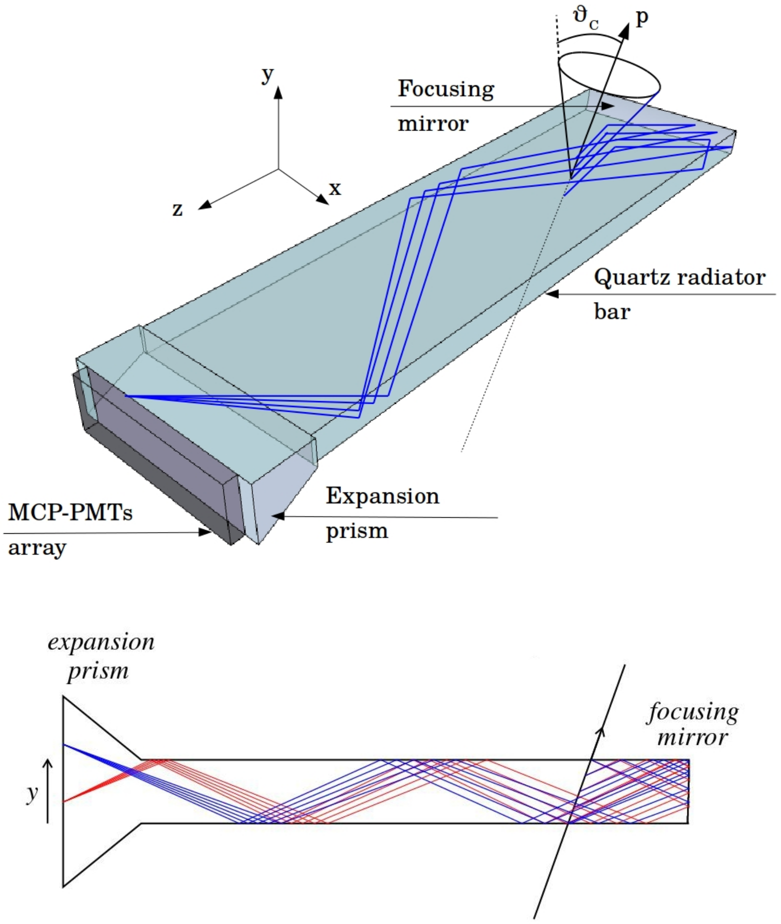

Figure 3.12: Above: Schematic view of the TOP counter. The blue lines represent the direction of Cherenkov photons that are focused by the focusing mirror. The dimension of the quartz radiator are 2.7 m × 45 cm × 2 cm. The expansion prism is 10 cm long. Photons are focused and directed towards a 2 × 16 matrix of MCP-PMTs. Each MCP-PMT has a size of 27.5 × 27.5 mm^2 with a sensitive area of 22 × 22 mm^2 divided in 16 anodes. The MCPs have a diameter of 10 μm. Under: Chromaticity effect, image taken from [83].

To evaluate the K/π separation, the probability distribution functions (PDFs) for K and π particle hypothesis are introduced: respectively they are $\mathcal{P}^K(x,t)$ and $\mathcal{P}^\pi(x,t)$. Photons detected by MCP-PMTs for each track are tested against this two PDFs hypothesis. From the PDFs it is possible to determine the likelihood defined as $\mathcal{L}^{K,\pi} = \prod_{i=1}^{N_\gamma} \mathcal{P}_i^{K,\pi}(x,t)$, where N_γ is the number of photons detected. If $\Delta\mathcal{L} = \log\mathcal{L}^\pi - \log\mathcal{L}^K$ is positive the particle is classified with a pion otherwise with a kaon. Figure 3.13 shows $\Delta\mathcal{L}$ in the two cases.

3.5 Aerogel Ring-Imaging Cherenkov detector: ARICH

ARICH is the other Cherenkov effect-based detector used for PID inside the *Belle*II detector. It is located in the forward endcap and it is designed to improve the separation between pions and kaons up to momenta of 4 GeV/c and between pions, muons and electrons below momenta of 1 GeV/c. ARICH is composed by an aerogel radiator in which charged particles produce Cherenkov photons that are detected by an array of photon detectors. Aerogel can be produced with any desired refractive index n between 1.01 and 1.2. Between the aerogel radiator and the array of photon detectors there is a 20-cm-thick

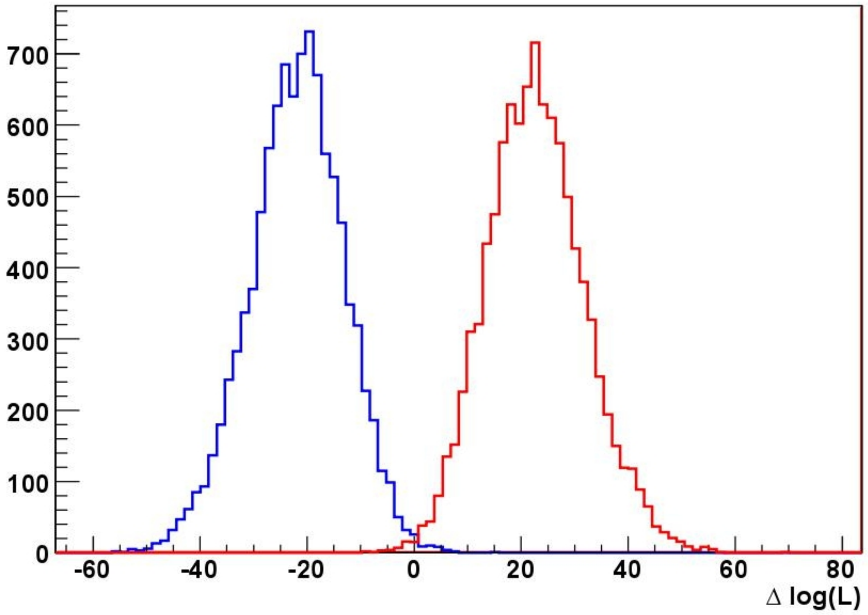

Figure 3.13: $\Delta\mathcal{L}$ distributions for pions, in red, and kaons in blue, corresponding to 500 tracks of 300 GeV$/c$ that cross the quartz bars perpendicularly.

expansion volume necessary to produce large enough Cherenkov rings. For ARICH two radiators with different refractive index are used: $n_1 = 1.046$ and $n_2 = 1.056$. In this configuration the number of photons detected and the Cherenkov angle resolution improves since the slight difference in refractive index make the photon from the two radiators arrive in the same point of the focal plane. Figure 3.14 shows the focusing configuration.

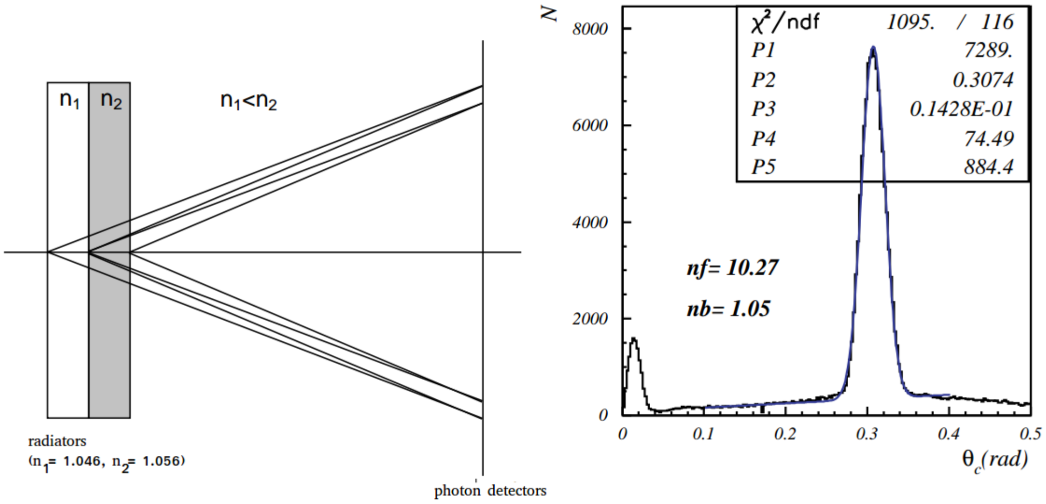

Figure 3.14: Left: Focusing configuration of the ARICH. It is based on the use of an inhomogeneous aerogel radiator. Right: θ_C distribution in the focusing configuration (with refractive index of $n_1 = 1.046$ and $n_2 = 1.056$); the resolution is $\sigma_{\theta_C} \approx 14$ mrad. Events have been simulated with radiator 4 cm thick. The image is taken from *The Belle*II *Technical Design Report* [76].

Photon detectors are based on Hybrid Avalanche Photo-Detectors (HAPD) technology: they consists of a vacuum tube with included an avalanche-diode type photo-detector (APD). Cherenkov photons generate photoelectrons from a photocatode through photoelectric effect. Electrons are accelerated by a potential difference of 8 kV towards the APDs

that provide a gain of a factor 40. HAPDs are arranged in 9 concentric rings, in total 540 sensors of size 73 mm × 73 mm are required: they are composed by a matrix of APD pixels 12 x 12, each APD is 4.9 mm × 4.9 mm.
The inner radius of the ARICH is 410 mm, the outer radius is 1140 mm and ARICH covers a geometric acceptance from $\theta \simeq 15^o$ to $\theta \simeq 30^o$.
The number of photons detected expected is around 20 for each track. The resolution on the Cherenkov angle for N photons detected is $\sigma_{\theta_C}^N = \sigma_{\theta_C}/\sqrt{N}$, considering $N = 20$ and the Cherenkov angle resolution for the individual photon, $\sigma_{\theta_C} = 14$ mrad, the resolution on the Cherenkov angle becomes:

$$\sigma_{\theta_C}^{N=20} = \frac{\sigma_{\theta_C}}{\sqrt{20}} = \frac{14}{\sqrt{20}}\ \text{mrad} \approx 3.1\ \text{mrad} \tag{3.3}$$

3.6 K_L^0 and μ detector: KLM

KLM is the detector used for K_L and μ reconstruction. It consists of active detector elements spaced by iron plates, which provide 3.9 X_0 of material. Inside the iron plates the K_L can shower hadronically. The KLM is composed by Resistive Plate Chambers (RPCs), located in the outermost layers of the barrel region, and by scintillator strips coupled with silicon photomultiplier (SiPM), arranged in the endcaps and in the two innermost layers of the barrel region. The barrel region covers a angular acceptance from $\theta \simeq 45^o$ to $\theta \simeq 125^o$ that is extended by endcaps from $\theta = 20^o$ to $\theta = 155^o$.
The RPCs are composed by two electrodes (2 parallel planes 2 mm thick) made by high resistivity glass spaced of 2 mm. The space between electrodes is filled with a gas mixture of 62% HFC-134a freon, 30% argon and 8% butane. The outer surface of each electrode is painted with a carbon-doped paint that allows to distribute high voltages (HV) to electrodes, in this way an uniform electric field of 4.3 kV/mm in the gas filled gap is generated. A charged particle crossing the RPCs ionizes the gas molecules along its path. The electric field accelerates the electrons towards the anode and ions towards the cathode. Electrons and ions induce a signal on a 5 cm wide metal strips located on each side of RPCs, used for the readout of the signal. The metal strips are separated from an external ground plane by a dielectric foam layer: this structure work as a transmission line with a characteristic impedance of 50 Ω. Two RPCs are coupled to form a single superlayer in order to improve the detection efficiency of particles. The metal strips are arranged orthogonally in the two RPCs in order to measure both z direction and ϕ direction. Figure 3.15 shows a section of a RPC superlayer.
Because of the estimated inefficiency of RPCs located in the endcaps in the high rate environment of *Belle*II, endcaps of the KLM are equipped with scintillator strips that are coupled with SiPM for the signal readout: the whole system consists of 16800 scintillator strips long up to 2.8 m and have a cross section between 7 mm and 10 mm × 40 mm. Strips width has been chosen in order to maximize the spatial resolution for muons and K_L reconstruction and minimize the total number of channels. Each strip has a groove in the center where an optical fiber is arranged. The fiber pick up the scintillation light and carries it to the SiPMs that are composed by 667 photodiodes pixel of 1.3×1.3 mm^2. The system composed by fibers coupled with SiPM is characterized by a high time resolution, which is around $\sigma_t = 0.7$ ns, and by a high output rate capability. The high time resolution allows to measure the time of flight of K_L mesons.

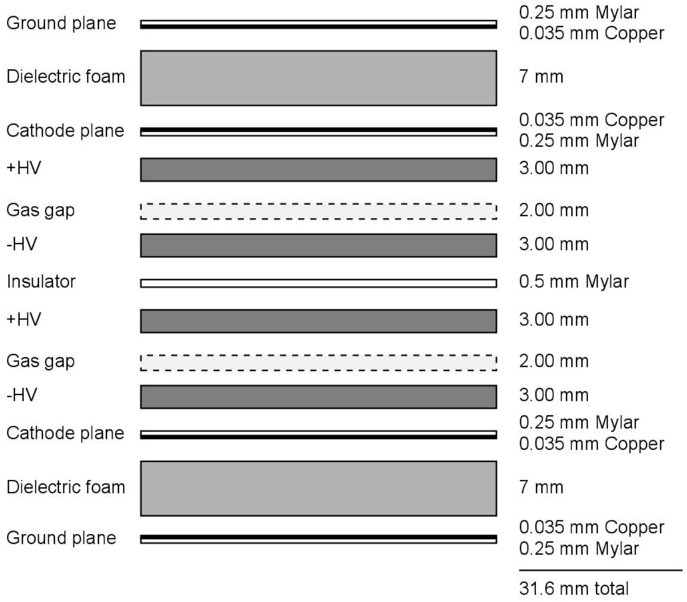

Figure 3.15: Cross section of a RPC superlayer. Superlayers are 2.20 m long and the width of each superlayer varies from 1.67 m to 2.75 m. A module is composed by two superlayers disposed side by side above the iron plate. Each module is 4.40 m long.

Disadvantages of SiPM are the high level of noise, pixel cross-talk and a high ambient temperature dependence.
Muon identification begins from the reconstruction of a charged track in the CDC. The charge track is extrapolated up to the KLM region under the hypothesis that it was generated by a π: 0.6 GeV/c is the minimum momentum that a track needs in order to cross at least one KLM module and be considered into the KLM acceptance. If a KLM hit is near the crossing of the extrapolated track on the KLM module, than it will be associated to the track. Two range are defined: the predicted range by the track and the effective range. The predicted range is defined by the outermost KLM module crossed by the extrapolated track considering the interactions that the particle associated to the track makes inside the KLM. The effective range is defined by the outermost KLM module in which there is a hit associated to the track. If the predicted range and the effective range differ significantly, the track is classified as hadron, otherwise the same procedure is repeated starting from the extrapolation of the track under the hypothesis that the track is generated by a μ. Hits associated to the track with an appropriate fitting technique are used to predict the path of the track into the KLM. The goodness of fit and the difference between the measured range and the predicted range are used in a likelihood ratio test in order to test the hypothesis of μ against the hypothesis of hadron.
For what concerns the K_L identification, all the KLM hits within a 5^o opening angle measured from the IP are grouped together to form a cluster. When all clusters are formed the charge track veto is applied. Each track is extrapolated to its entrance into the KLM and a straight line is drawn between the entrance point and the IP. If the track is within a 15^o opening angle compared to a line drawn form the center of a cluster and the IP, the event is rejected. If the KLM cluster is aligned to a neutral reconstructed ECL cluster within a cone of 15^o the two cluster are associated and the direction of the ECL cluster is considered for the application of the charge veto track. A K_L candidate is classified as

KLM only candidate if there are at least two clusters associated to the candidate in two different KLM modules. While a K_L candidate is classified as KLM + ECL candidate if there are at least one cluster in the ECL and one cluster in the KLM associated to the candidate.

The muon detection efficiency in the barrel KLM (BKLM) is about 89% for momenta $p \geq 1$ GeV/c. The contamination from hadrons is around 1.3% rising up to 3.8% at 0.7 GeV/c. Fake muons are pions that do not decay in flight and do not produce inelastic hadronic interactions in the KLM. The contribution from kaons to the hadron fake rate is much less because they are identified efficiently from the PID systems. The K_L detection efficiency is of the 80% for momenta $p \geq 3$ GeV/c. Muon and K_L detection efficiencies in the endcaps KLM (EKLM) are similar.

Figure 3.16 shows the side view of the *Belle*II KLM.

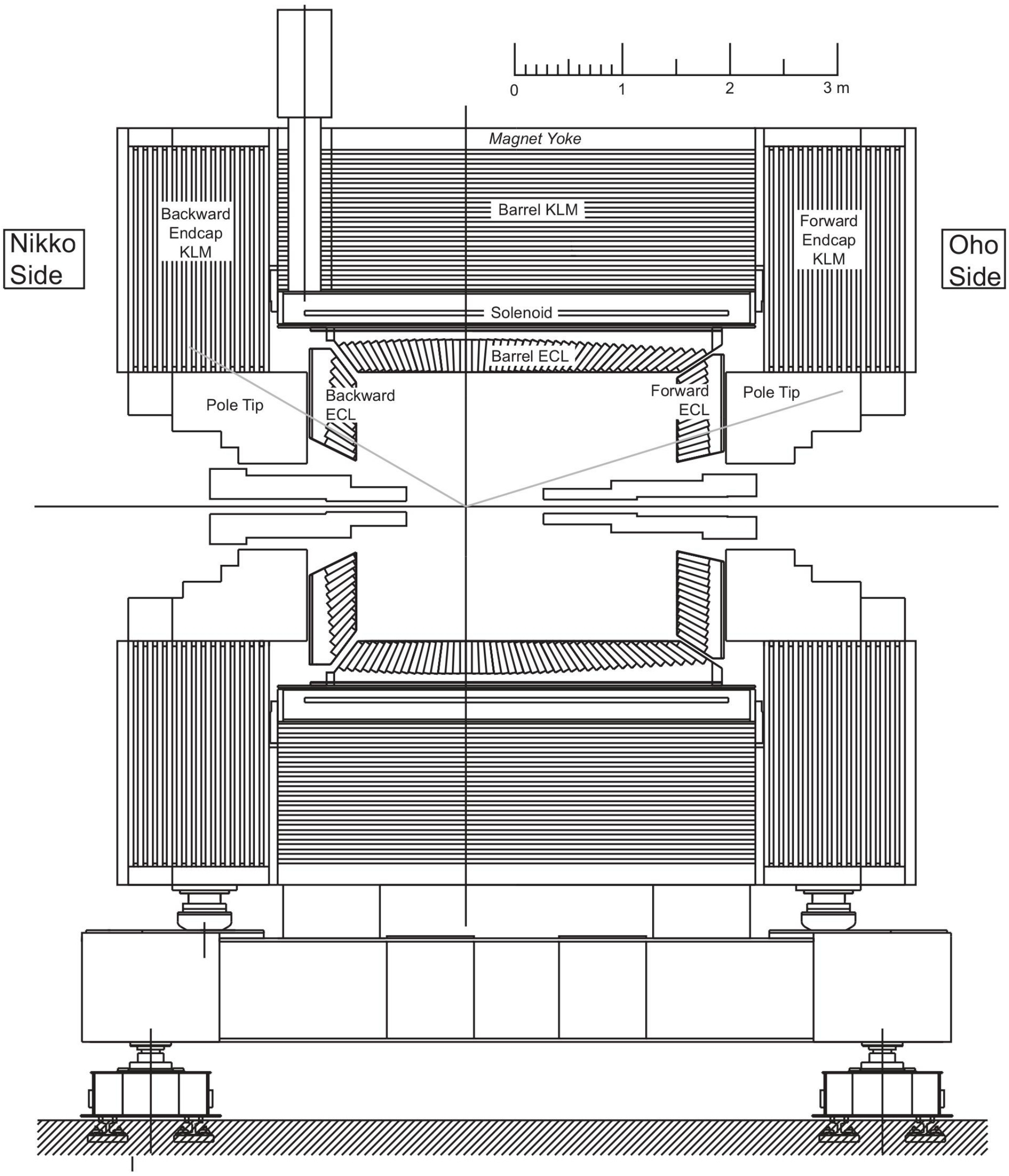

Figure 3.16: Side view of the KLM. The gray lines represent the nominal acceptance. Image taken from *The Belle*II *Technical Design Report* [76].

3.7 Electromagnetic Calorimeter: ECL

About 1/3 of B meson decays provide photons in an energy range from 20 MeV to 4 GeV, for this reason a high resolution ECL is very important. The tasks of ECL are: the detection of photons with high efficiency, the precise determination of the energy of the photons and a precise determination of angular coordinates, the identification of electrons, provide an appropriate trigger signal for the other detectors, provide the online and offline measurement of the luminosity and the detection of K_L together with the KLM.
For ECL it has been chosen to reuse *Belle* CsI(Tl) crystals changing the readout electronics in order to handle the higher background levels. CsI(Tl) crystals are characterized by scintillation light with a decay constant of 1.3 μs and by an average output of about 5 thousand photoelectrons per MeV with a noise level of 200 keV (the values reported was measured using calibration with cosmic rays muons) [76]. ECL consists of 3 m long barrel section, the inner radius is 1.25 m and the endcaps are located at $z = 1.96$ m and $z = -1.02$ m from the IP. ECL covers an angular acceptance from $\theta = 17^o$ to $\theta = 150^o$ except for two gaps of about 1^o wide between the barrel ECL (BECL) and the endcaps. The total amount of ECL crystals is 8736, divided in 6624 crystals in the BECL and 2212 crystals in the endcaps. The average size of each crystal is 6×6 cm^2 in cross section and 30 cm in length that corresponds to 16.1 X_0. The lateral size of crystals is chosen to be comparable with the Moliere Radius and the thickness is enough to prevent significant energy loss for photons up to several GeV.
In order to face the high background level in SuperKEKB, electronics based on waveform sampling with pipelined readout has been designed. The former allows to use time information in order to reject off-time events hits, the latter allows to parallelize readout process in order to reduce dead times (16 crystals are read at a time). The scintillation light detection is done using two sets of silicon photodiodes, with a sensitive area of 10 mm × 20 mm, glued in the back of crystals. A preamplifier is connected to each set of photodiode in order to have two independent output for each crystal. The two pulses are added and processed by two shaper boards, one characterized by a time constants of 0.2 μs used to generate the trigger signal, the other characterized by a time constant of 0.5 μs. The signal waveform produced by the second shaper board is sampled through 16 samples that are used to extract amplitude and timing. This new electronic allows to reduce the cluster fake rate of a factor of 7 maintaining an efficiency on photon detection of 97%, in accordance with simulations.

The general formula that express the resolution of calorimeters is $\sigma_E/E = \gamma/E \oplus \alpha/\sqrt{E} \oplus \beta$ where α is the stochastic term, γ is the noise term and β is the constant term that takes into account the stability of the calibration, the uniformity of the signal and leakage effects. The intrinsic energy resolution of the ECL measured using a prototype is reported in the following equation, where E is in GeV.

$$\frac{\sigma_E}{E} = \sqrt{\left(\frac{0.066\%}{E}\right)^2 + \left(\frac{0.81\%}{\sqrt[4]{E}}\right)^2 + (1.34\%)^2} \tag{3.4}$$

Figure 3.17 shows a schematic view of the ECL.

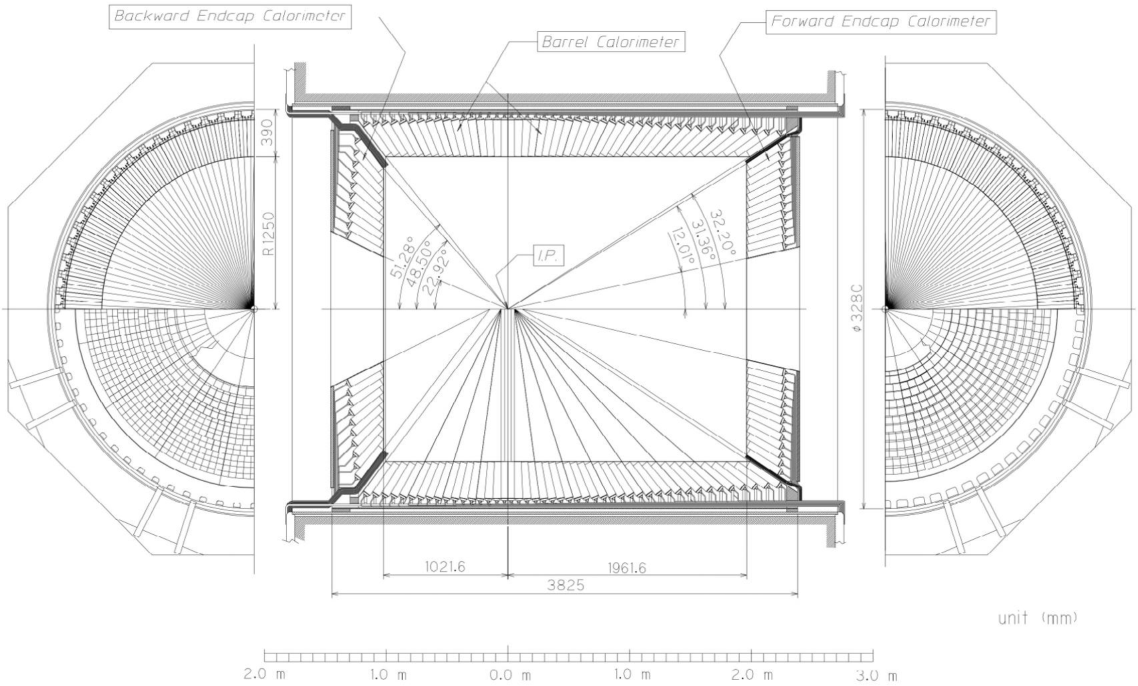

Figure 3.17: Schematic view of the ECL, all three detector regions, barrel as well as the forward and backward end-caps are shown in the image. The total number of crystals amounts to 8736 and the ECL covers about 90% of the solid angle in the center of mass reference system .The image was taken from Reference [79].

3.8 Trigger

In order to apply an efficient event selection at the designed luminosity of $\mathcal{L} = 8 \cdot 10^{35}$ cm^{-2} s^{-1} of SuperKEKB, the trigger system must satisfy the requirements listed in the following:

- around 100% efficiency for hadronic events from $\Upsilon(4S)$ B meson decays and from annihilation events in the continuum;
- maximum average trigger rate of 30 kHz;
- a fixed latency around 5 μs and a timing precision $\leq$ 10 ns.

The trigger rate and the total cross section of some relevant events at the designed luminosity of SuperKEKB are listed in Table 3.4. Bhabha events and $\gamma\gamma$ events are used to measure the luminosity and to study the response of the detector.

$B\bar{B}$ events and hadronic events from continuum are characterized by a large multiplicity of tracks in the final states, in order to select efficiently this kind of events it is possible to set the trigger to require a large number of tracks in the final state. It is more complicated design a trigger for low multiplicities events, as for example τ leptonic decays or processes involving dark sector particles, because they are characterized by zero or only two tracks in the final state, for this reason they are hardly distinguishable from background events. Moreover some of low multiplicities process, as for example $e^+e^- \to \mu^+\mu^- Z'(Z' \to \text{Invisible})$ studied in this thesis work, have a topology quite similar to Bhabha events, $\mu^+\mu^-$ events or $\gamma\gamma$ events that have a very large cross section. It is necessary, then, apply a veto in order to suppress Bhabha, $\mu^+\mu^-$ and $\gamma\gamma$ events and this cause a loss of trigger efficiency.

Process	Cross section σ_X (nb)	Event rate (Hz)
$\Upsilon(4S) \to B\bar{B}$	1.2	960
Hadron production from the continuum	2.8	2200
$\mu^+\mu^-$	0.8	640
$\tau^+\tau^-$	0.8	640
Bhabha events ($\theta_{lab} \geq 17^o$)	44	350 $^{(a)}$
$\gamma\gamma$ ($\theta_{lab} \geq 17^o$)	2.4	19 $^{(a)}$
2γ processes ($\theta_{lab} \geq 17^o$ and $p_T \geq 0.1$ GeV/c)	$\simeq 80$	$\simeq 15000$
Total	$\simeq 130$	$\simeq 20000$

$^{(a)}$ Rate is prescaled by a factor 1/100
since this events have large cross sections

Table 3.4: Total cross sections and trigger event rates of different processes at the $\Upsilon(4S)$ peak at the SuperKEKB designed luminosity of $\mathcal{L} = 8 \cdot 10^{35}$ cm^{-2} s^{-1}. Table taken from *The Belle*II *Technical Design Report* [76].

The trigger system is composed by the Level 1 trigger (L1) and the High Level Trigger (HLT) implemented in the Data Acquisition System (DAQ).

3.8.1 L1 Trigger

The L1 trigger system consists of sub-trigger systems that collect the trigger information of the relative sub-detector and send those information to a Global Reconstruction Logic (GRL) where a low level reconstruction is done combining the information of the individual sub-trigger systems. Results obtained by the GRL are sent to the final decision logic, the Global Decision Logic (GDL), that finally releases a trigger signal when its selection criteria are satisfied. In *Belle*II, each sub-trigger component is based on the Field Programmable Gate Array (FPGA) technology. A FPGA device consist of an integrated circuit whose functionality can be configured without disassembling the device or without send it back to the manufacturer to change it. The GRL is based mainly on the CDC and ECL trigger information, but also TOP and KLM are included in the system.

The CDC sub-trigger provides information about the tracks detected in the CDC. It consists of a 2D trigger that is based on the track reconstruction in the plane (x,y) and of a 3D trigger that adds information on the z-coordinate near to the IP. The 3D trigger is very important for the background rejection because tracks relative to background events are characterized by a z-coordinate not localized near the IP while tracks produced by e^+e^- collisions come from the IP and their z-coordinate is around zero.

The ECL trigger generates fast signals both for neutral and charged particles. Two different configurations have been designed, one based on the total energy deposit in the ECL and the other on the isolated clusters. The former is sensitive to physics events with high electromagnetic energy deposit while the latter is sensitive to multi-hadronic physics events that produce low energy clusters, and to MIPs. Furthermore the ECL trigger can identify Bhabha and $\gamma\gamma$ events that are characterized by a back-to-back topology: this is very useful to measure the luminosity in real time and to ensure a high trigger efficiency for low multiplicity events.

The TOP trigger provides precise timing and hit topology information and the KLM trig-

ger is used for event selection of μ pairs. The KLM trigger is independent from the CDC trigger and it is useful to measure efficiencies of the other sub-triggers and improve the trigger efficiency of low multiplicity events.
The GDL receives all sub-trigger information, and after logic calculations and prescaling it provides the L1 trigger. The total latency of the L1 trigger is around 5 μs.
The Trigger is affected by an uncertainty of around 10 ns called *trigger jitter* (TJ).

3.8.2 HLT

The HLT consists in a full reconstruction of the event using the event data from all detectors and a software trigger for the event is produced using the physics event-selection software that is composed by two parts:

- the Level 3 Trigger (L3): it makes a cut on the track multiplicity, on the vertex position of the event and on the total energy deposit in the ECL, after a fast track reconstruction using only the data provided by the CDC and a fast reconstruction of the ECL clusters. Applying the L3 trigger a reduction of data size of the 50% is expected and this pre-selection allow to reduce the processing time for each event;
- the physics-level event selection trigger: it performs the full event reconstruction using the same software used for the offline event reconstruction in order to avoid additional systematic uncertainties different from those of the offline reconstruction. The selection of the events applied by this trigger employ similar selection criteria used to produce skims, as for example the hadronic selection or the low-multiplicity selection. The code used for this level of selection has been used offline by *Belle* to do analysis on the physics of B mesons and D mesons and they produced respectively a reduction of 14.2% and 9.6% on events that passed the L3 trigger: the total selection of events that passed the L3 trigger is around the 25%. The reduction of the data size made by the HLT is around the 12.5% that is assumed to be of the 20% by the DAQ system.

3.9 Belle II software and computing

The computing system of *Belle*II uses a grid-based approach: an infrastructure of many facilities distributed to all members of the *Belle*II organization connected to a common software, in order to process the huge amount of data produced during the activity of *Belle*II. The data taken are stored, the calibration constants dependent on the condition of the accelerator and of all sub-detectors are continuously determined and written in database (DB), the raw data are processed and the high-level information are saved in small files called mDST. Offline, the mDST files are produced and contain NTuples with high-level information and analysis information that the user decides to save. In addition to the real data, MC samples with a higher size compared to that of real data are produced and stored. The MC simulations produce mDST files from which NTuples are produced and used for analysis, in the same way as for real data.
After that, the data are stored and offline software packages are used for processing the data. Offline software are used for MC simulations, reconstruction of tracks and physics analysis. The software framework used by the *Belle*II experiment is called Belle Analysis

Framework 2, or more briefly *basf2* [84], that is used both for online data management (as for example for the HLT) and for offline data management, as for example for physics analysis or detector software optimization.

Basf2 is based on modules for the framework, mostly written in C++, scripts, mostly written in python, and dataobjects. Modules are the main components of *basf2*, they allows to implement in the software framework all operations needed for the analysis or the optimization of detectors: from generation of MC samples to simulation of all detector and to reconstruction of tracks, from unpacking of raw data to physics analysis, extracting all parameters required by the user and saving them in appropriate files, as mDST. The modules are handled using appropriate scripts called *steering files* that allow to call the necessary modules, set the parameters and insert modules in *paths*. When the data are processed, *basf2* executes the modules in the order as they are recalled in the *steering file*. Each module can access the *DataStore*, which is a common repository to which all modules have access to writing and reading. Each module can read or write the *dataobjects*, which are the elementary classes of *basf2* written in C++ and which contain the information provided by the detector or by other modules. The information written in *dataobjects* are stored in the *DataStore*.

Finally the DB contains the information about the geometry of the detector, the information about the material budget of every single piece of the detector, the calibration constants, the accelerator parameters and all those information needed by the user in order to perform simulation, reconstruction of data and so on.

The user can access to the DB in order to update the information of the detector, for example update the calibration constants after a sub-detector calibration run, or in order to recall and use in modules and scripts the information contained in it.

Chapter 4

Calibration of the SVD *hit time* estimator

In this chapter, the method developed by the candidate to calibrate the SVD *hit time* estimator, called Center of Gravity ($\mathcal{COG}$), will be presented. After a first short description of the relevant features of the SVD reconstruction software, the importance of a good SVD *hit time* resolution for background rejection is discussed together with the definition of the $\mathcal{COG}$ time estimator. The method adopted to calibrate the $\mathcal{COG}$ is then described in detail: it exploits the correlation among the $\mathcal{COG}$ and the timing information provided by the CDC to improve the SVD *hit time* resolution. Results obtained by using both cosmic ray and collision data are presented, the chapter ends with a discussion of the future prospects of this work.

4.1 SVD reconstruction software

Before introducing the definition of the $\mathcal{COG}$ *hit time* estimator and the method for its calibration, it is useful to describe briefly the relevant features of the SVD reconstruction software, using some concepts that have been introduced in Section 3.9, useful to understand how the software works.

The primary purpose of the SVD reconstruction software is to build the *space points* used by the tracking software. The steps with which the software reconstructs the *space points* are listed in the following:

- the first step consists of processing the raw data provided by the detector in the form of dataobjects called RawSVD, which contain low-level information provided by the APV25 and the position information of the APV25 channels above the online zero suppression threshold applied by the peripheral electronics. The SVDUnpacker is an appropriate module that decodes information from RawSVD and returns as output the same information in a more usable way, providing the dataobject called SVDShaperDigits for each strip above threshold;

- the information contained in the SVDShaperDigits are: the numbers that identify layer, ladder, sensor and side corresponding to the strip read by APV25, the amplitudes of each of the six samples of the signal waveform provided by the APV25, which are stored in a 8-bit integer number, and the *trigger bin* (see Section 3.2.2) of the event;

- the information provided by the SVDShaperDigits are used, with the method described in next sections, to estimate the charge collected by the strip and the *hit time* with a module called SVDCoGEstimator, which also preserves information about position and returns a dataobject called SVDRecoDigit as output;
- a module called SVDSimpleClusterizer merges the adjacent strips to form the clusters. A cluster is defined as a group of adjacent strips in which at least one strip has a Signal-to-Noise-Ratio (SNR) ≥ 5 (*seed*), to suppress the contribution from noise signals, and the adjacent strips have a SNR ≥ 3. This module also provides the cluster position and the cluster time, both calculated as the weighted mean, respectively of the position and the time of the individual strips composing the cluster, weighted with the charge of the strips;
- the *space points* providing the 2-dimensional information used by the tracking are formed by combining clusters on one side with all clusters on the other side of each sensor.

Figure 4.1 shows schematically how the SVD reconstruction software works.

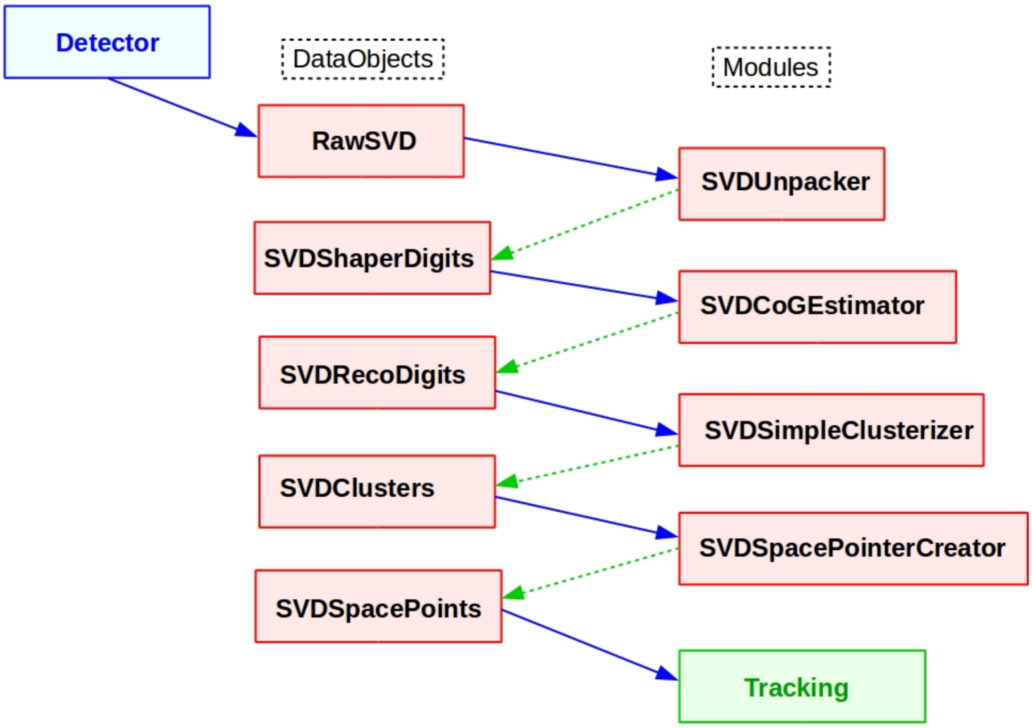

Figure 4.1: Schematic representation of the working principle of the SVD reconstruction software and of the steps needed by the SVD reconstruction software to reconstruct the *space points* starting from raw data. The modules take as input and return as output dataobjects, which contain the processed data provided by the SVD.

After the first steps of tracking reconstruction, the cluster position can be corrected using the information of the estimated incident angle of the track on the sensor to improve the quality of the tracks. In addition, the estimate of the energy loss in the sensor is provided to the PID algorithms. No further details are given on these two steps as they are not relevant for the work here described.

4.2 SVD *hit time* with the Center of Gravity

Hit time information are very important in SVD for background rejection. MC simulations show that hits from particles due to machine background (called "background hits") are approximately one order of magnitude more abundant than hits from tracks due to interesting signal events, in particular for the layer 3. It is estimated that background occupancy in the layer 3 is around 1% per sensor; this means that around 8 strips over 768 strips for each side have a signal above the threshold. As seen in section 2.1, the multiplicity of tracks in $b\bar{b}$ events is 11, on average. The layer 3 is composed by 7 ladders with 2 sensors for each ladder, so approximately one signal track is crossing each sensor giving one signal cluster per side and one *space point* per sensor. In the worst case, if the 8 strips over the threshold due to background hits are not adjacent, they form 8 background clusters of size 1 strip for each side, while the signal cluster is only 1. The combinatorial of the 9 clusters for each side (8 due to background and 1 due to signal) results in 81 *space points* of which only one is from an interesting particle. The remaining *space points* consists of 64 *space points* of background, i.e. made by both clusters associated to background particles, and 16 *space points* made by one cluster of signal and one cluster of background, known as *ghost hits*.

If the time of the interesting e^+e^- collision, the *event time*, is known it is possible to efficiently reject the clusters from background, as they are off-time with respect to the *event time*.

Also the *ghost hits* can be rejected using time information. They are generated, for example, by combining the information of two particles that cross the DSSD sensor in different events. If, for example, the charge released in the sensor by each particle is collected by only one strip for each side, two clusters of size 1 for each side are generated and in total four strips are fired. Combining the information provided by the four strips, four *space points* will be reconstructed, but only two of them are associated to particles while the others two *space points* are the *ghost hits*. Figure 4.2 shows an example of the *ghost hits*. A possibility is to evaluate the difference of time of the two strips (on U/p-side and on V/n-side) composing the two *space points*: if the time are not compatible the two space point can be rejected.

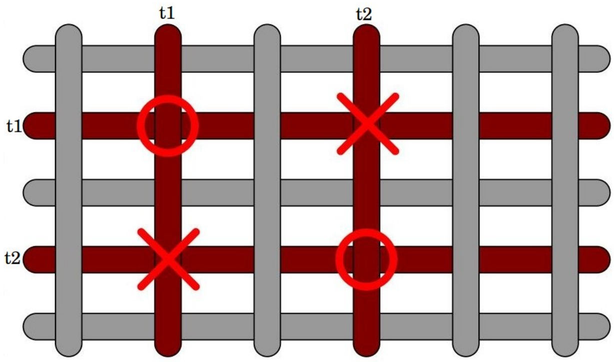

Figure 4.2: Example that explain what are the *ghost hits* in a DSSD sensor. Red circles are the positions in which the two particles cross the sensor in different times. Red cross are the *ghost hits* due to the four combinatorial possibilities. Image taken from Reference [81].

The particles produced in the e^+e^- annihilations, i.e. coming from the IP, are very energetic and, assuming that they travel at the speed of light in ~0.5 ns, they reach the farthest SVD layer, which is distant ~14 cm from the IP. Under this assumption, the measurement of the *hit time*, corresponding to the time when the signal is created in the SVD sensors, can be used as a good estimation of the *event time*[1]. The tracking performances can be significantly improved with a resolution on the *hit time* of the order of a few ns. The calibration of the *hit time* estimator becomes very important for background rejection of off-time clusters with respect to the *event time*.

The method developed to estimate the *hit time* of particles that cross each sensor is called *Center of Gravity* ($\mathcal{COG}$). As explained in Section 3.2.2, signals produced by particles crossing the sensors are read and sampled by APV25 chips. For each strip there are six samples available for the reconstruction of the collected signal and the time of passage of the particle in the SVD sensor.

Figure 4.3 shows an example of the signal waveform sampled.

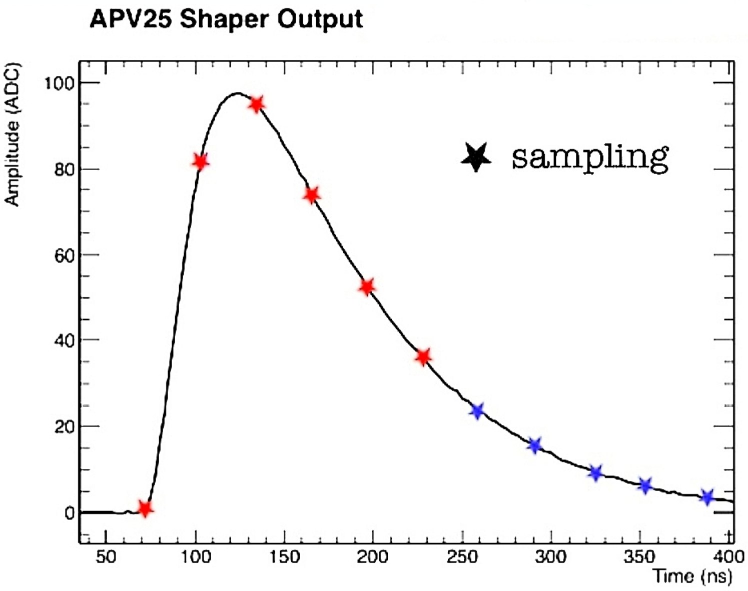

Figure 4.3: Example of a signal waveform sampled by the APV25 chips at 31.8 MHz, i.e sampling every ~31.45 ns. The *hit time* is the time when the signal start rising, while the *peak time* is the time when the signal reaches its maximum. Red stars are the six samples used to reconstruct the waveform. The *peaking time* is approximately ~50 ns after the signal start to rise (*shaping time* of the APV25) but can vary from strip to strip being sensitive also to the capacitive load of the APV25 corresponding channel.

The charge assigned to the strip is the biggest charge of the six samples.

The time when the signal start rising is called *hit time*, while the time when the signal reaches its maximum is called *peak time*. In order to obtain the *hit time*, first of all the six samples are used to estimate the peak time with the $\mathcal{COG}$ time estimator, and then several corrections are applied.

The $\mathcal{COG}$ peak time estimator is the weighted mean of the time of the six samples, the weight is the charge of the same samples. The definition is:

$$t_{CoGraw} = \frac{\sum\limits_{n=1}^{6} A_n t_n}{\sum\limits_{n=1}^{6} A_n} = \frac{\sum\limits_{n=1}^{6} A_n n}{\sum\limits_{n=1}^{6} A_n} \cdot \Delta t \qquad (4.1)$$

---

[1] The expected resolution of the *event time* using information from CDC, TOP and ECL is order of ns.

Where n indicates the number of the samples, t_n and A_n are respectively the time of each sample and the charge of each sample and $\Delta t = 31.45$ ns. To extract the *hit time* from $\mathcal{COG}$, a first correction is applied, called *peaking time correction*. This consists in subtracting the *peaking time* of that particular strip from the calculated t_{COGraw}. This *peaking time* is a strip-dependent quantity that varies with the different capacitive load associated with each strip, so it is different for n-side and p-side and for each strip of the forward sensors. Its value is measured for every strip during the SVD calibration runs and it is stored in the database. Unfortunately also after this first correction the $\mathcal{COG}$ is not yet a good estimator of the *hit time*. First of all the values of the *peaking time* stored in the DB are affected by an unknown shift that depends on the conditions at which the calibration runs have been performed. Furthermore, the $\mathcal{COG}$ estimator tends to underestimate the *hit time*, as shown later. For these reasons the $\mathcal{COG}$ needs to be further calibrated.

4.3 Center of Gravity Calibration

The calibration method has been developed using the cluster time, estimated by the SVD with the $\mathcal{COG}$, and the *event time* estimated by the CDC. The calibration method has been developed initially doing a SVD+CDC-only reconstruction of cosmic ray runs and exploiting the correlation among the *event time*, estimated by the CDC, and the cluster time, estimated as explained in previous sections as the weighted mean of the $\mathcal{COG}$ time estimator for each strip, weighted with the charge of each strip. These variables in the following text will be called respectively t_0 and t_{COG}.

Waveform difference on U/p and V/n sensor side

For the $\mathcal{COG}$ calibration the V/n-side and and the U/p-side of the sensors are studied separately, since the waveforms provided by the two sides are different due to several effects. The p and n side strips have different capacitive load that can change the waveform shape given by the APV25; furthermore the APV25 chip is operating in a different configuration for p and n side (inverter on/off), to be able to read signal of opposite charge collected on the two side of the sensors. Both these effects contribute to the difference observed in the shape of the APV25 signals obtained during calibration runs, injecting a known calibration pulse in the the internal APV25 calibration circuit. Figure 4.4 shown an example of these calibration output for the two sides of a layer 5 sensors. Signals on p side have a slight longer peaking time, about 10 ns, and larger width of about 20 ns.

In addition to these effects, visible already in calibration, the rise time of the real signal coming from the silicon sensor is also affected by the different mobility of holes and electrons: with holes, collected on U/p-side, being 3 times slower than electrons, collected on the V/n-side, the final signal of the APV25 for U/p-side is slower than on V/n-side, as shown in Figure 4.5, with an example of the waveform for the V/n-side and the U/p-side of the layer 5 in the case of simulated data. Figure 4.6 shows an example of sampled waveforms from cosmic ray data in which it is possible to see that the waveform of the U/p-side tends to be wider than the waveform of the V/n-side.
The differences between the waveforms on the two sides affect the $\mathcal{COG}$ time estimation: for V/n-side signals, that tends to be narrower than U/p-side signals, a better $\mathcal{COG}$ resolution is achieved. Further studies are still ongoing to understand the details of this difference observed in data.

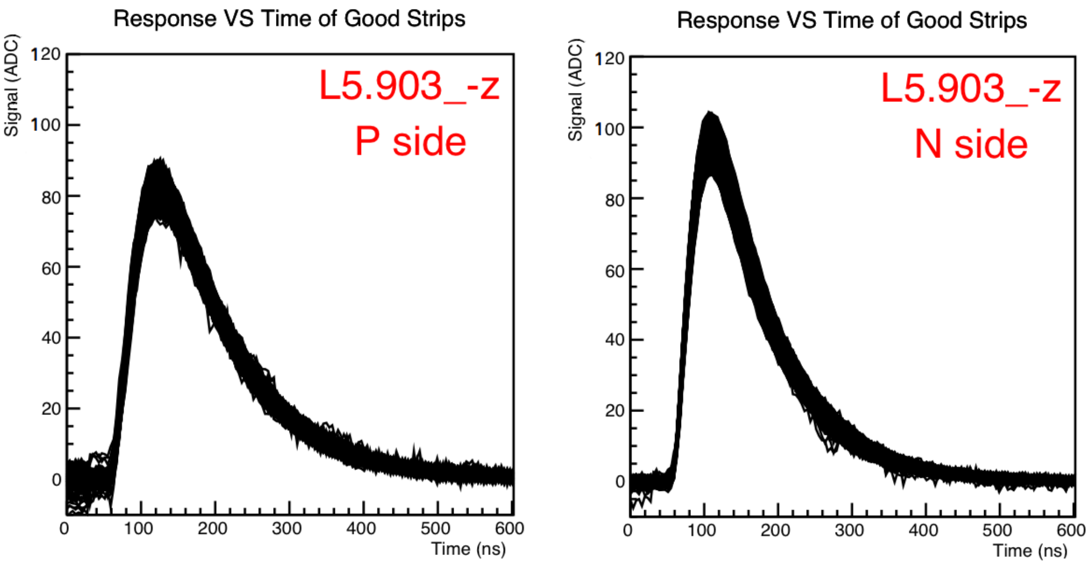

Figure 4.4: Example of real APV25 waveforms obtained in calibration runs: a calibration pulse is injected in each APV25 input with an internal calibration circuit. Signals from a layer 5 sensors are shown for U/p-side (left) and V/n-side (right). Signals on U/p-side tends to be wider and with a slight longer peaking time. All strips of one side are plotted.

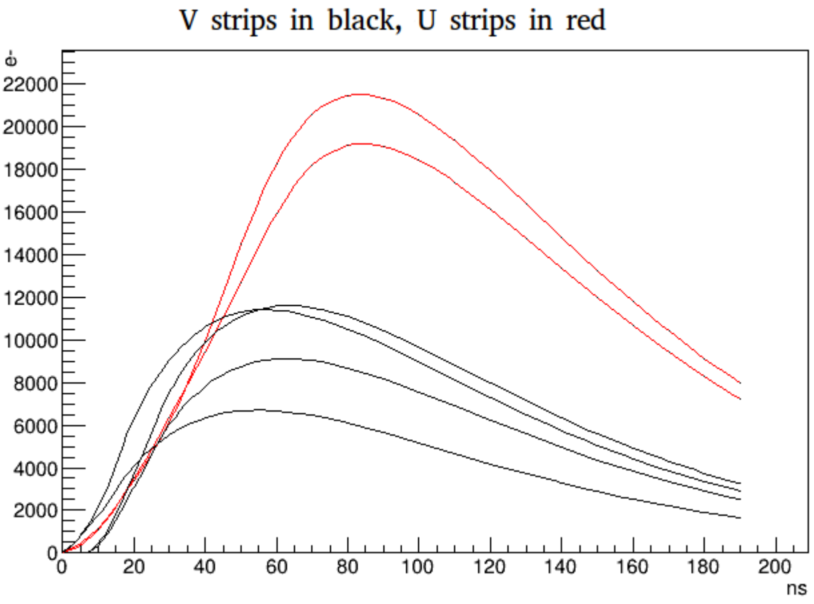

Figure 4.5: The graph shows the simulated waveform of the U/p-side (red) and of the V/n-side (black). The different height of the waveforms is due to the fact that 1-strip cluster for the V-side and 2-strip cluster for the U/p-side have been simulated to produce this graph. It is possible to see that the two waveforms have different rise time, V/n-side shows a faster rise time than the U/p-side since electrons, collected in the V/n-side, have a faster mobility than holes, collected in the other side. Simulation shown here is not yet tuned and the effect shown here is larger then the one observed on data.

SVD and CDC time references

For the $\mathcal{COG}$ calibration it is useful to separate events belonging to different *trigger bins* (TB), already introduced in Section 3.2.2. The TB is the time window of ~8 ns, in which the SVD has received the L1 Trigger signal, as shown in Figure 4.7, where the black lines represents the APV25 clock, while the green boxes represent the TBs and the yellow

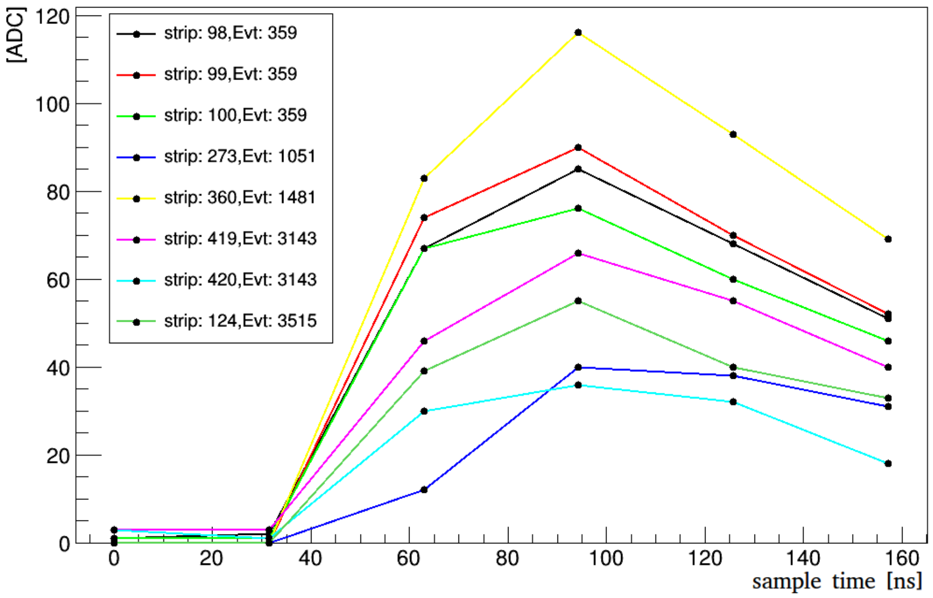

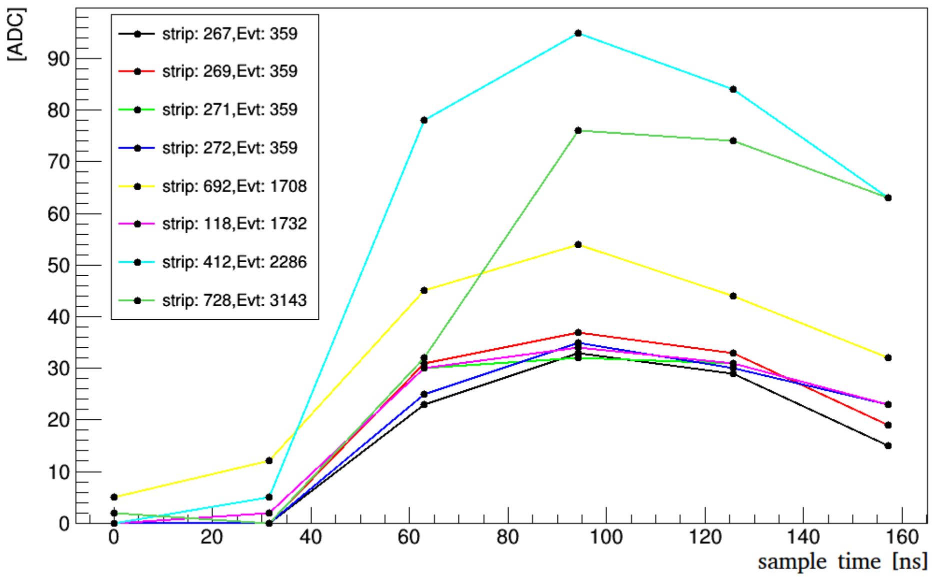

Figure 4.6: The graphs show the waveform for the V/n-side (above) and for the U/p-side (below) obtained by plotting the amplitude and the time for each sample provided by the APV25 for each strip. The amplitude is in ADC counts. The different height of the waveforms depends on the energy released by the particle that cross the sensor and on the charge collected by the strips. The plots are obtained from a cosmic ray run.

line represents the time at which the L1 trigger signal is received from SVD. Since the peripheral electronics controlling the APV25 chips has a clock which is 4 times faster than the APV25 clock, it can return in which quarter of the 31.45 ns of the APV25 clock period the trigger arrived (TB).

In order to understand the relation between the SVD and the CDC time of reference, it has to be considered the time acquisition system of SVD and CDC shown in Figure 4.7 and described below.

The red line represents the time at which a physics event occurs. After a fixed time ($\sim$5 μs) from the physics event, the L1 trigger sends a signal. The yellow band around the L1

trigger line represents the *trigger jitter*, which is ∼10 ns and has the effect to shift backward or forward in time signal sent by the L1 trigger, for this reason the time provided by the trigger can be measured in a different TB.
The red star indicates the trigger bin that contains the time of the trigger, in the example the TB number 1, while the blue star is the sample at the time equal to the *latency* in the SVD reference system frame, i.e. the origin of time of SVD corresponds to the time of the blue star minus the latency. The origin of the CDC time is defined with a fixed CDC latency ($\neq$ for SVD) from the L1 Trigger signal. The *event time* t_0 is measured in the CDC time reference, while the t_{COG} is measured in the SVD time reference.

The origin of time of the CDC and SVD are not synchronized and this information is stored in the TBs through the shift $a = \delta_t(3 - n_{TB})$ ns, where $\delta_t \sim 8$ ns and n_{TB} is the TB number, so the information provided by the TB can be exploited to correct the shift in time among the CDC *event time* and the *hit time*.
Therefore t_0 can be expressed as a function of the t_{COG} plus a shift a depending on the TBs (a) and a residual shift between SVD and CDC origin (c):

$$\begin{aligned} t_0 &= f(t_{COG}) + a + c \\ a &= \delta_t(3 - n_{TB}) \end{aligned} \tag{4.2}$$

The quantity $t_0 - a = f(t_{COG}) + c$ is expressed in the SVD time reference system. Studying the relation between t_0 and t_{COG}, $f(t_{COG}) + c$ can be extracted and used to calibrate the $\mathcal{COG}$.

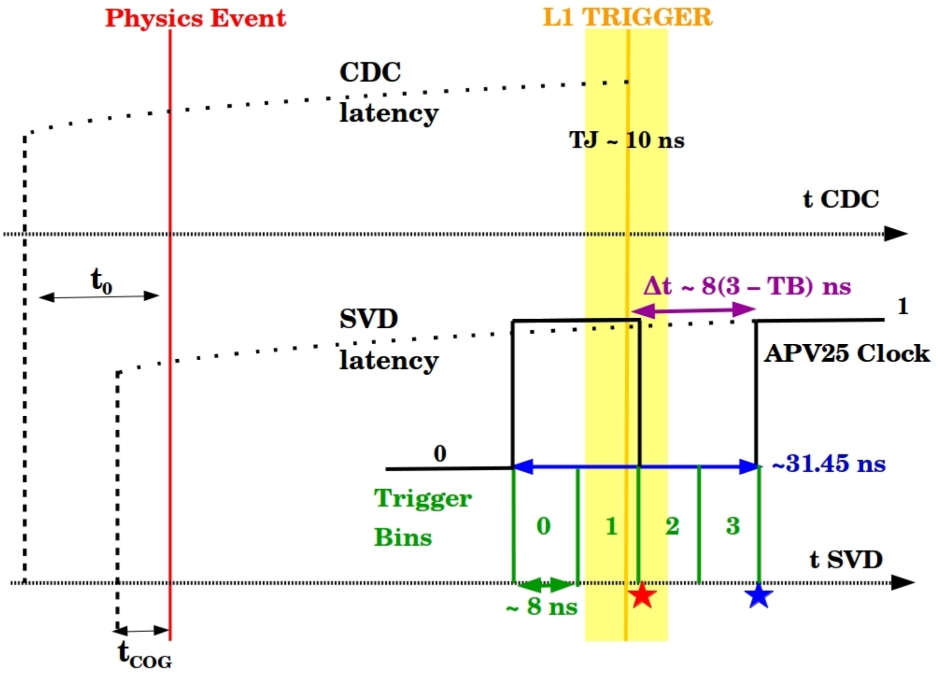

Figure 4.7: The working principle of TBs and the time acquisition system of SVD and CDC.

4.3.1 Calibration using Cosmic Ray data

The data set acquired during *Phase*-2 global cosmic ray run is used to study the $\mathcal{COG}$ calibration. For the study run 2804 has been analyzed. The initial study described in this section is done separating each TB and including a, defined in Equation 4.2, in the correlation function $f(t_{COG})$.

The t_0 event time provided by the CDC and and t_{COG} cluster time distributions for the V/n-side and the U/p-side of the layer 5 are shown in Figure 4.8.

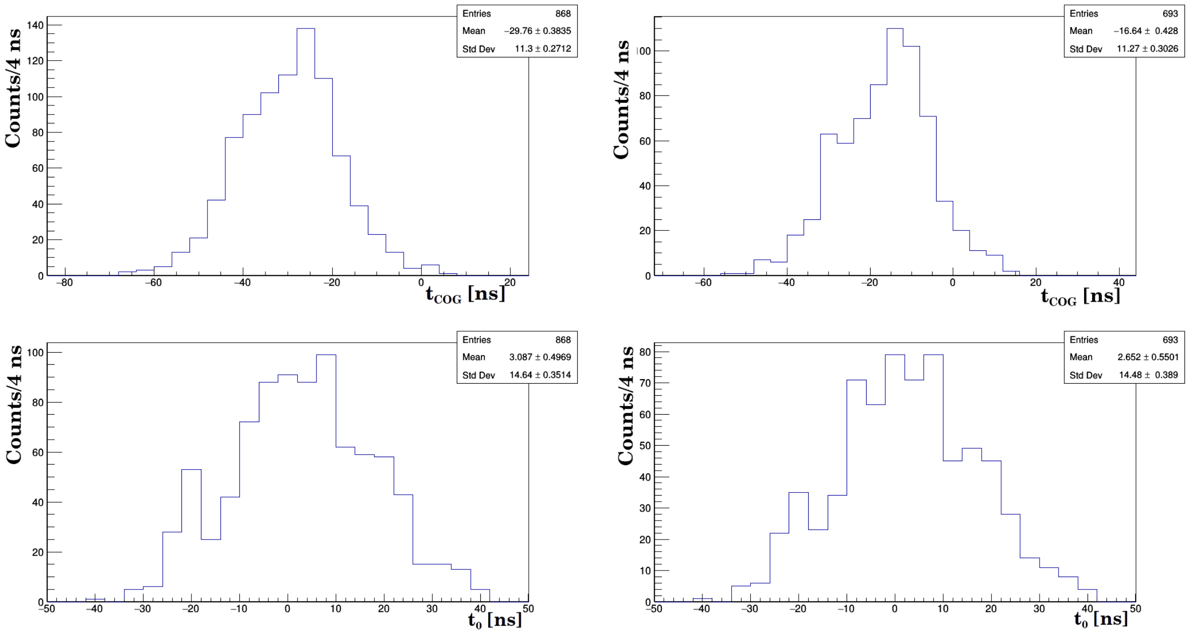

Figure 4.8: Above: $\mathcal{COG}$ time distributions respectively of the U/p-side (left) and the V/n-side (right) of the layer 5. Below: distributions of the t_0 associated to the same events of the selected strips in the plots shown above for the two different sides. The entries of the two sides are different because clusters that pass the selection described in the text are included, the two numbers are expected to be the same if clusters associated to the tracks are considered and this is not the case.

The scatter plots of t_0 versus t_{COG}, used to calibrate the COG exploiting the correlation among these variables, have been produced for each *trigger bin*. In order to improve the statistics, all clusters of all sensors of each layer are considered together for the calibration, except the forward sensors that are quite different from the other sensors, see Section 3.2 for the description of the SVD sensors. Figure 4.9 shows the scatter plots of t_0 versus t_{COG} for the V/n-side and the U/p-side of the layer 5, obtained using cosmic ray data. The different colors indicate the different TBs. A linear correlation between t_0 and t_{COG} is clear from the plots, therefore the relation 4.2 can be written as $t_0 = \alpha \cdot t_{COG} + \beta$, where β includes the parameters a and c defined in the previous section.

In order to obtain the parameters used for the calibration, for each TB, a linear fit of the profile of the scatter plot, which provides the slope α and the intercept β used to correct the $\mathcal{COG}$ TB by TB, has been performed. In Figure 4.10, an example of linear fit is shown. The intercept represents a *bias* on the $\mathcal{COG}$ estimation, while the slope indicates if the $\mathcal{COG}$ overestimates ($\alpha < 1$) or underestimates ($\alpha > 1$) the *event time*. The general trend of *bias* and slope versus the TB number is shown in Figure 4.11. The graphs show that the slope increases as the TB number increases, i.e. when the L1 trigger time is closer to the SVD origin of times, the underestimation of the *event time* provided by the $\mathcal{COG}$ compared to the CDC estimation increases; while the *bias* decreases as the TB number increases, i.e. when the L1 trigger time is closer to the SVD origin of times, the *bias* on the $\mathcal{COG}$ compared to the CDC estimation decreases, as expected.

The calibrated $\mathcal{COG}$ is defined as $t'_{COG} = \alpha \cdot t_{COG} + \beta$. The values of α and β are evaluated on the cosmic ray run 2804 and then are applied to correct the $\mathcal{COG}$ of a different cosmic ray run, in order to evaluate the validity of the method.

The residual of the $\mathcal{COG}$ is defined as the width of the distribution of the difference between the cluster time, estimated by the $\mathcal{COG}$, and the *event time*, estimated by the CDC. Figure 4.12 shows the $\mathcal{COG}$ resolution before applying the calibration for each TB. The idea behind the calibration method is to correct the $\mathcal{COG}$ *hit time* for each strip applying the calibration constants calculated in each TB. After this calibration the distribution for each TB overlap and the resolution improves.

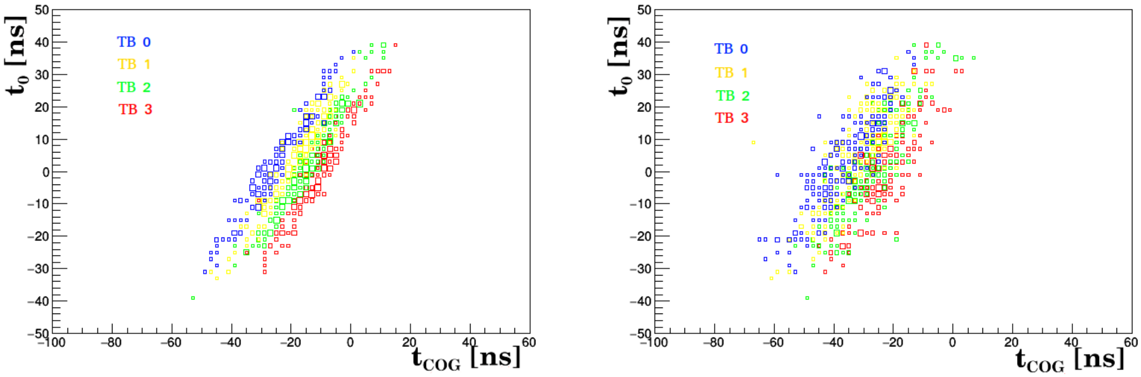

Figure 4.9: Left: Scatter plot t_0 vs t_{COG} for the V-side of the layer 5. Right: Scatter plot of t_0 vs t_{COG} for the U-side of the layer 5. Both have been obtained from the same cosmic ray run and by considering all sensors except the forward one. The TBs are well separated in the case of the V-side on the contrary of the U-side, which is characterized by a worse resolution. In both cases it is possible to observe a linear correlation between t_0 and t_{cog}.

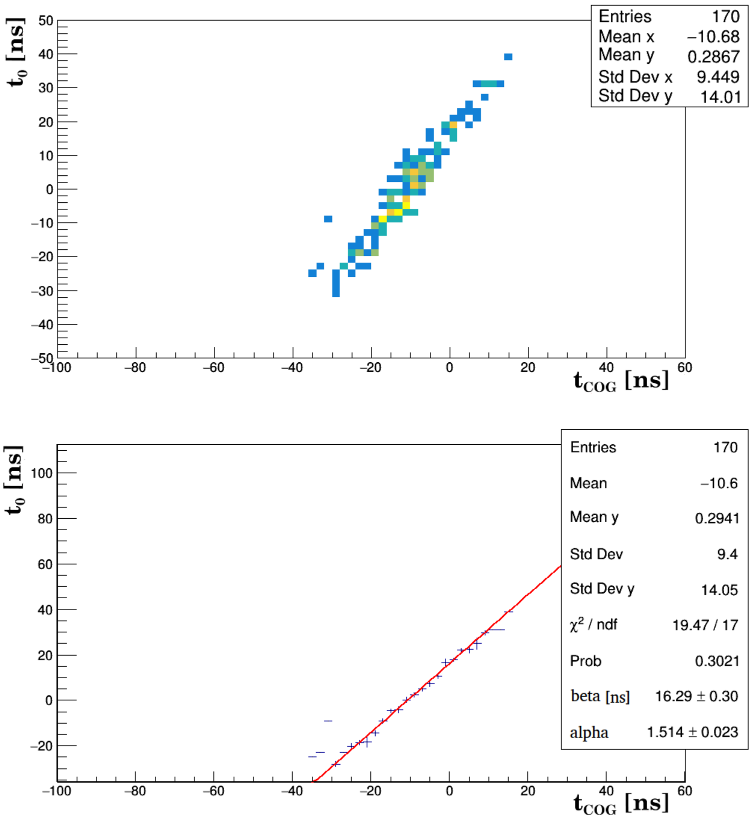

Figure 4.10: Above: Scatter plot t_0 vs t_{COG} for 5 V/n-side of the layer 5, TB number 3. Below: Linear fit of the profile of the same scatter plot.

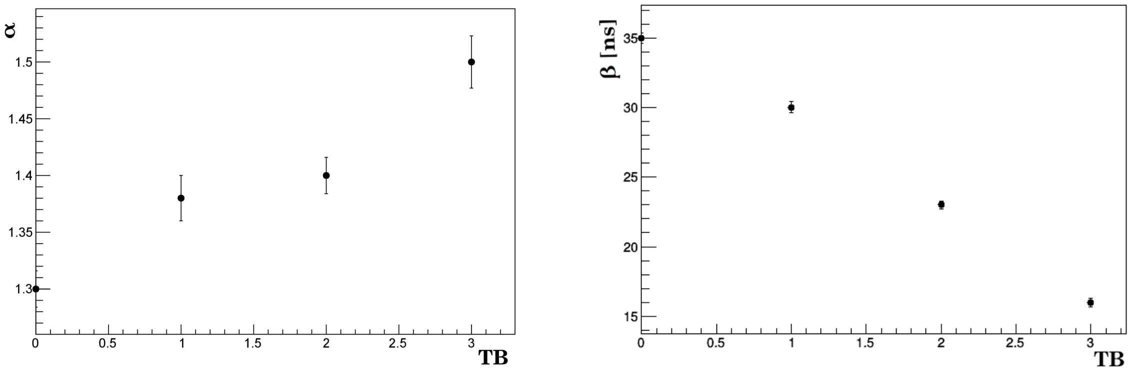

Figure 4.11: Left: Values of the slopes in function of the TB number. Right: Values of the intercepts in function of the TB number. Both are obtained from the linear fit of the profile of the scatter plot for the V-side of the layer 5.

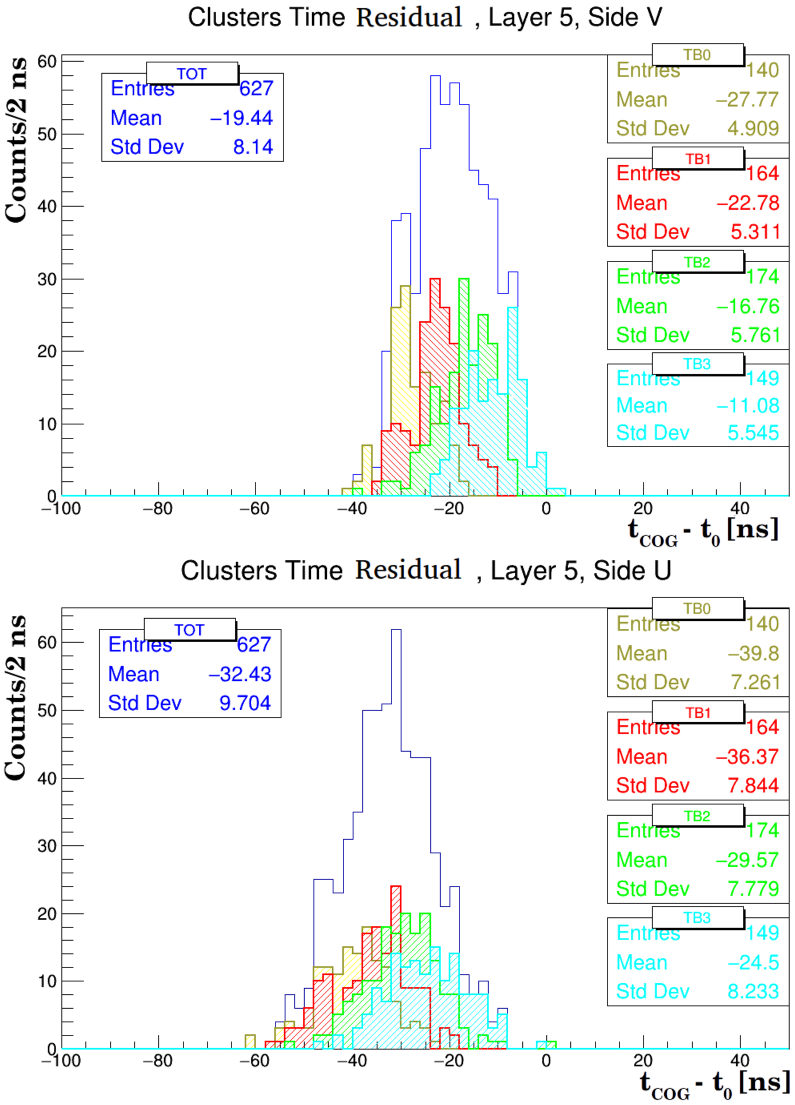
Clusters Time Residual , Layer 5, Side V

Clusters Time Residual , Layer 5, Side U

Figure 4.12: Distribution of the $t_{COG} - t_0$ obtained for the different TBs and the total distribution for the layer 5. Above: the V/n-side. Below: the U/p-side. The RMS of the distribution indicates the $\mathcal{COG}$ residual before the time calibration.

Figure 4.13 shows the $\mathcal{COG}$ residual before and after the calibration, for the V/n-side of the layer 5: the resolution improves from 7.7 ns to 3.6 ns, which is an improvement of the

~50%. Also the residual for the U/p-side of the layer 5 has been evaluated before and after the correction and it improves from 9 ns to 7.6 ns, which is an improvement of ~15%. In general, similar improvements have been observed for all layers. Since the width of the residual is the result of the $\mathcal{COG}$ resolution convolved with the CDC resolution (~2 ns), the width of the residual distribution represents an upper limit to the $\mathcal{COG}$ resolution. The achieved resolution on the V/n-side match the expected one reported in the *The Belle*II *Technical Design Report* [76].

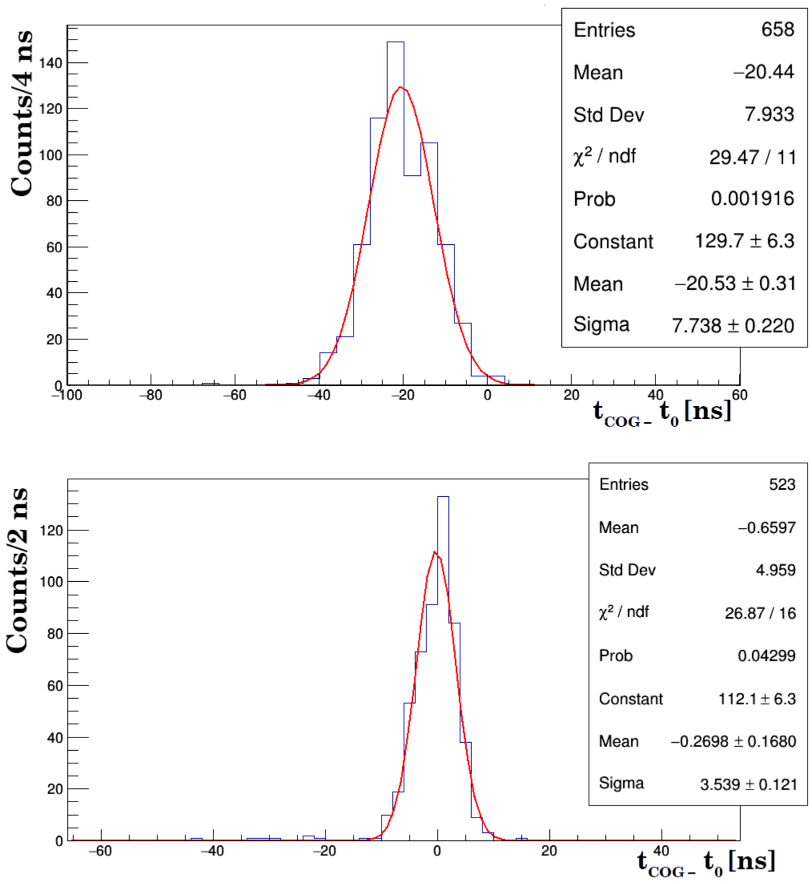

Figure 4.13: Above: the $\mathcal{COG}$ residual distribution before to apply the correction. Below: the $\mathcal{COG}$ resolution after that the correction has been applied. Both graphs have been done for the V/n-side of the layer 5. This is an example, in general the same residual distribution have been obtained for the V/n-side of the other layers.

4.3.2 Calibration using collision data

The same method described for the calibration of the $\mathcal{COG}$ tested with the cosmic ray data has been applied to collision data. However there is a fundamental difference in the data acquisition between cosmic ray and collision runs. During the cosmic ray runs the events were not synchronized with the APV25 clock, while for collisions, since the bunch crossing frequency is a multiple of the APV25 clock frequency, the APV25 readout was synchronized with the events.

Furthermore, the reconstruction of the collision data is similar to that performed for the cosmic ray data, but instead of select strips inside ROIs, only clusters associated to the tracks have been selected, after performing the tracking reconstruction.

All-events selected runs have been used for the study described in this selection.

The distributions of t_{COG} and t_0 for the V/n-side of the layer 3 are shown in Figure 4.14.

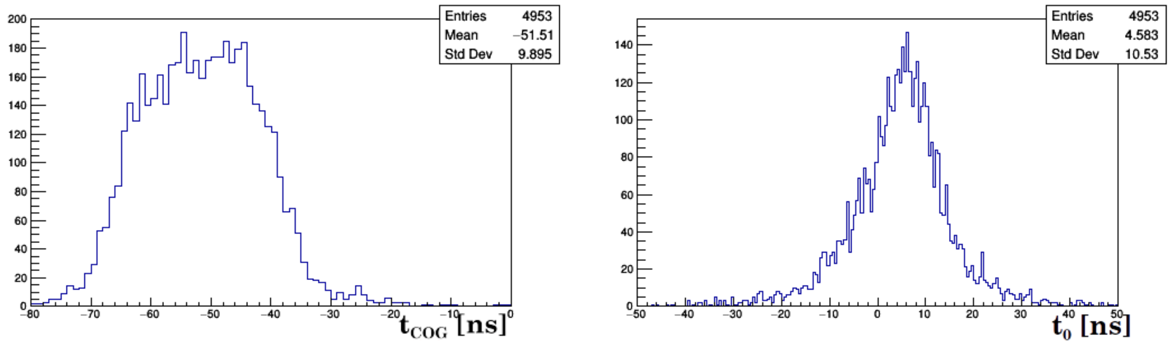

Figure 4.14: Left: t_{COG} distribution of the V/n-side of both sensors of the layer 3 for a generic collision run. Right: t_0 distribution of the same sensors and side for the same collision run.

The collision data runs are characterized by different *fill patterns*, which indicates the number of *bunch crossing* occurring for each TB.

An SVD+CDC-only reconstruction of a collision run with a *fill pattern* characterized by a *bunch crossing* each ∼8 ns, i.e. one *bunch crossing* for each TB, has been performed. Figure 4.15 shows the scatter plot of $t_0 - a$ versus t_{COG} for each TB, indicated by different colors. Considering one TB, the scatter plot is different from that shown in Figure 4.9 for the cosmic ray run, the reason is that cosmic ray are not related to a bunch crossing but they are distributed uniformly in time while in this case the collisions occur following the *fill pattern* scheme. In principle the scatter plot should appear in bands limited in the time region defined by the trigger bins in which the bunch crossing occurred, but because of the effect of the *trigger jitter*, which allows to scan a wider time region around each TB, the TBs result overlapped.

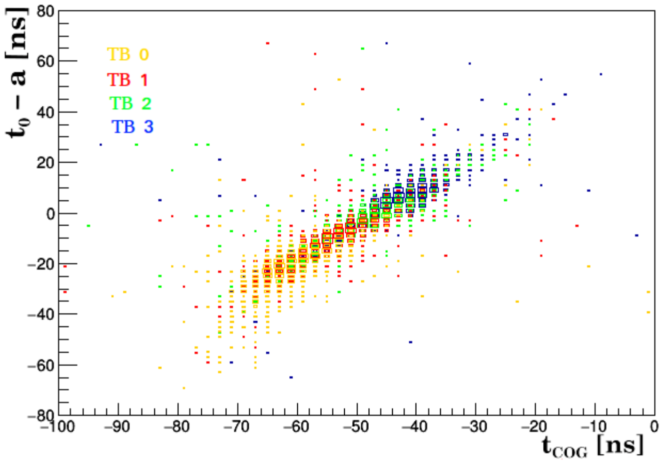

Figure 4.15: The scatter plot of $t_0 - a$ versus t_{COG} for the different TBs indicated with different colors. A linear correlation between $t_0 - a$ and t_{COG} can be observed.

Thanks to the synchronization of the CDC and SVD origin of time, a linear correlation between $t_0 - a$ and t_{COG} is observed, similarly to what is seen for cosmic rays. For this reason the same procedure used with cosmic rays will be applied to collision data. Figure

4.16 shows the scatter plot for the TB number 0 of the V-side of the layer 3, considering clusters reconstructed on both sensors, and the linear fit of the profile of the scatter plot. As in the case of the cosmic rays, the same procedure is applied to all layers and for each TB, joining together the clusters of both sensors of the layer 3 and the cluster of all sensors of the other layers, except the forward sensor. The values of α and β have been obtained from the fit and they have been used to correct the $\mathcal{COG}$ of a different run. The correction applied to the $\mathcal{COG}$ in the case of the collision data is analogous to that defined in the case of cosmic ray. An example of the final result obtained is shown in Figure 4.17. Both graphs shown in figure have been obtained from a generic collision data run and the parameters (α and β) used to do the correction have been obtained from a different collision run. Both runs are characterized by the same *fill pattern* of one bunch crossing for each TB. The final $\mathcal{COG}$ resolution obtained is around $\leq$4 ns for the V/n-side.

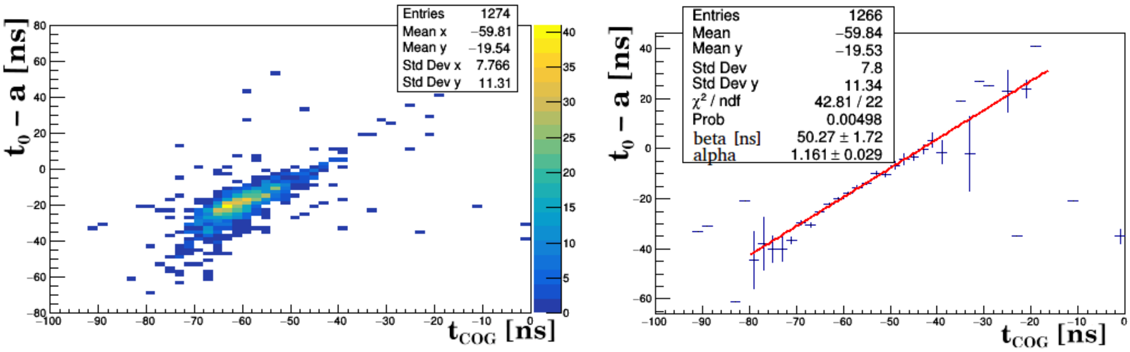

Figure 4.16: Left: scatter plot of the V/n-side of the layer 3 for the TB number 0, considering both sensors. Right: linear fit of the profile of the same scatter plot.

The plot shows a residual bias of ∼0.35 ns that is still under investigation.

For what concerns the U/p-side, in the case of collision runs no improvement on the $\mathcal{COG}$ resolution have been obtained with this method, on the contrary of what obtained with cosmic ray runs, where there was an improvement, although smaller than that obtained for the V/n-side. This is under investigation yet.

4.4 Future prospects

Currently the calibration has been tested on cosmic ray data and collision data, considering all clusters of similar sensors selected as described above and the final resolution obtained in the case of the V/n-side for the collision data is $\leq$4 ns. The python module SVDCoGCalibrationDBImporter developed by the candidate evaluates the parameters α and β and the residuals, for a set of sensors and for each TB. The python module also create the database objects that will be uploaded on the database, in order to use the update calibration constants during the standard reconstruction. The module that evaluates the $\mathcal{COG}$ (the SVDCoGEstimatorModule) has already been updated in order to include the calibration performed through the timing information provided by the CDC.

The performance of the calibration algorithm should still be tested on the forward sensors, and, with higher statistics, on individual barrel and backward sensors. Furthermore, the calibration method must be tested in more detail for the U/p-side of the sensors since, as already explained, they are more problematic with respect to the V/n-sides. In order to study the additional correction on the U/p-side, it is possible to study the correlation

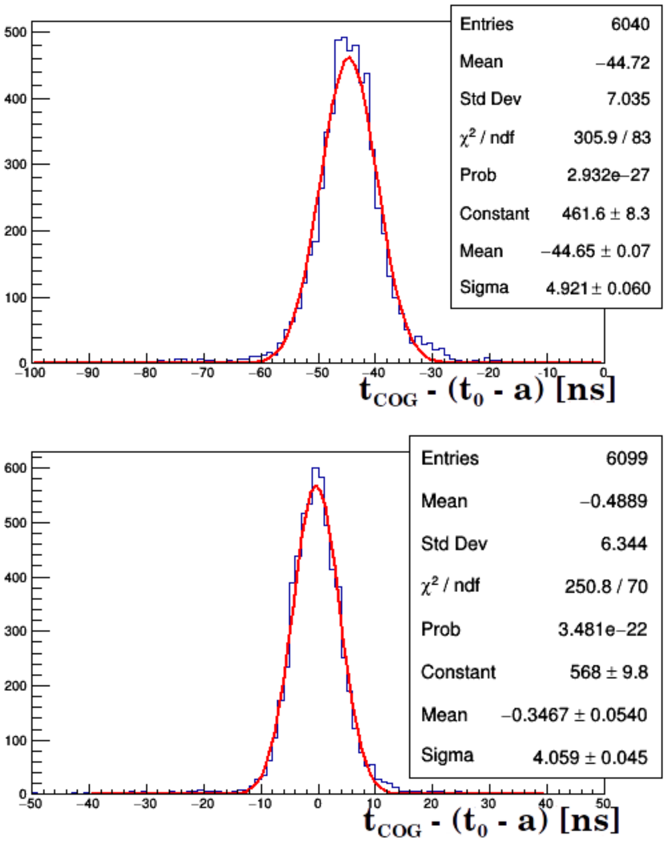

Figure 4.17: Above: the residuals $t_{COG} - t_0$ before to apply the correction on the $\mathcal{COG}$: the resolution is 4.9 ns. Below: the residuals after the correction of the $\mathcal{COG}$: the resolution is ∼4 ns.

between U/p and V/n times of *space points* associated to tracks.

Moreover it is necessary to associate an uncertainty to the calibrated $\mathcal{COG}$ for the clusters. The width of the residual distribution gives an indication of the error of the $\mathcal{COG}$, but in order to extract it, the correlation between the CDC and the SVD times should be correctly treated.

The knowledge of the *hit time* of the single strips could be finally exploited in the clusterizer to avoid adding background hits to signal clusters. This is another possible use-case for the *hit time* that could be studied.

Finally the impact of this calibration algorithm on the tracking performances will be evaluated soon.

Chapter 5

Analysis Overview

The motivations behind the study of the process $e^+e^- \to \mu^+\mu^- Z', (Z' \to \text{Invisible})$ have already been introduced in Section 1.5. Initially this analysis was thought to be performed on luminosity of *Phase*-2 corresponding to 20 fb^{-1}. However, the collected data set available is much smaller and corresponds to around 505 pb^{-1}.

In this Chapter, an overview on the analysis strategy is given. First the experimental signature of this process is described in Section 5.1, where the definition of the kinematic variable used for the signal yield extraction is provided. The preliminary studies performed on the simulated signal events are also reported, including the estimate of the signal cross section in the assumption of the $L_\mu - L_\tau$ model (see Section 1.3.1 for further details), the trigger efficiency and the expected mass and momentum resolution. The second section is dedicated to an overview of the possible background processes considered for this analysis, while the third section is focused on the generation and reconstruction of the process $e^+e^- \to J/\psi(\gamma), J/\psi \to \mu^+\mu^-$ used to evaluate the performances of the detector through the study of the J/ψ mass and muon momentum resolutions. Finally, a summary of the simulated MC samples and a description of the event generators used for their production is provided in the last section.

5.1 Signal events

The experimental signature of the process $e^+e^- \to \mu^+\mu^- Z'$ $(Z' \to \text{Invisible})$ consists of two tracks, consistent with the hypothesis of muons, plus missing mass calculated from the recoil against the dimuon candidate with respect to the total center of mass momentum. Everything other than dimuon candidate and its recoil mass which is reconstructed in the event belongs to the so-called *Rest of Event* (ROE). A reconstructed event is accepted only if the ROE is clean, with no additional tracks. Penetrating muons are able to cross the whole detector and they are identified thanks to the KLM, as explained in Chapter 3. Muon pairs are produced from e^+e^- annihilation at the center of mass energy of the $\Upsilon(4S)$ resonance therefore their invariant mass $M_{\mu\mu}$ is expected to peak around 10.58 GeV/c^2. In signal events, one of the two muons radiates the dark gauge boson Z', as shown in the Feynman diagram of the process in Figure 1.14, which consequently decays to an invisible state X, for example $X = \nu_{\mu,\tau}\bar{\nu}_{\mu,\tau}$, appearing as missing mass. In this case, $M_{\mu\mu} < \sqrt{s}$ and the difference between $M_{\mu\mu}$ and $\sqrt{s}$ is related to the mass of the emitted Z' boson. The signal yield is extracted by fitting the distribution of the recoil mass against the muon pair with respect to the center of mass momentum, which is expected to peak at the Z' mass for signal events.

The analysis plans to use the first data of the Belle-II experiment, collected during the running period known as *Phase*-2. It should be noted that the actual amount of data collected in *Phase*-2 is much smaller than anticipated, making it impossible to fully carry out the analysis. The recoil mass in the center of mass reference system is defined in Equation 5.1.

$$M^2_{recoil} = s + M^2_{\mu\mu} - 2\sqrt{s}(E^*_{\mu^+} + E^*_{\mu^-}) \tag{5.1}$$

Where $M^2_{\mu\mu} = (p_{\mu^+} + p_{\mu^-})^2$ is the square of the invariant mass of the muon pair, with p_{μ^+} and p_{μ^-} the four-momenta of the muons, and $E^*_{\mu^+}$ and $E^*_{\mu^-}$ are the energies of muons calculated in the center of mass system. In case the Z' is the only emitted particle in the event, the recoil mass M_{recoil} against the reconstructed muon pair corresponds to the mass of the radiated dark boson, which remains undetected.

Signal events have been generated by using the MadGraph5 framework, which allows to implement new physics models Beyond the Standard Model (BSM) and generate SM and BSM processes, providing cross sections and tools for event generation manipulation, [85]. Samples of 10 thousand events for different Z' masses in the range [0.5, 10] GeV/c^2 have been generated with MadGraph5, which provides an estimate of the cross section of the process, assuming the $L_\mu - L_\tau$ model, then the full detector reconstruction and the simulation of the generated samples, assuming the geometry of *Phase*-2, have been performed with GEANT4. The cross section for different Z' mass hypothesis, for a given coupling constant between the Z' boson and muons of $g' = 0.01$, is shown in Figure 5.1. The $L_\mu - L_\tau$ model predicts a cross section dependence on s which goes like $\sigma(e^+e^- \to \mu^+\mu^- Z') \sim g'^2(1 - M^2_{Z'}/s)$, and it vanishes for Z' masses approaching $\sqrt{s}$. Therefore for Z' masses larger than 8 GeV, even assuming a coupling of $g' = 0.1$, the expected sensitivity is too low for any detectable signal.

Given this cross section the total number of signal events expected at an integrated luminosity of 20 fb^{-1}, corresponding to the design luminosity for the *Phase*-2 commissioning, for $M_{Z'} = 1$ GeV/c^2 is around 120, assuming $g' = 0.01$.

The L1 trigger efficiency for signal events is estimated from the simulated MC samples and it is shown in Figure 5.2. The efficiency evaluated on the MC samples is constantly around the 82% for masses up to 8 GeV/c^2, while it starts decreasing for Z' masses larger than 8 GeV/c^2.

The analysis of the process $e^+e^- \to \mu^+\mu^- Z', (Z' \to \text{Invisible})$ is more challenging for lighter Z' masses when the recoil mass approaches the detector resolution. Figure 5.3 shows the muon momentum resolution depending on the Z' mass (left) and the Z' mass resolution as a function of the Z' mass itself (right). If the mass of the Z' is small, the radiating muon still carries a high momentum and it is hardly bent in the solenoid magnetic field and therefore being reconstructed with a worse resolution. Since the missing mass depends on the four-momenta of muons, the muon momentum resolution directly affects the recoil mass resolution. The mass resolution for $M_{Z'} = 500$ MeV/c^2 is around 170 MeV/c^2 and from the studies performed on the simulation, it is shown to limit the accessible mass of the Z'.

Due to the poor resolution of low Z' masses, signals for $M_{Z'} \leq 0.5$ GeV/c^2 are indistinguishable from the background $e^+e^- \to \mu^+\mu^-(\gamma)$, which peaks at small recoil masses, limiting the sensitivity of the experiment in this mass range. Figure 5.4 shows the recoil mass distributions for $M_{Z'} < 1$ GeV/c^2. They are produced requiring the muon identi-

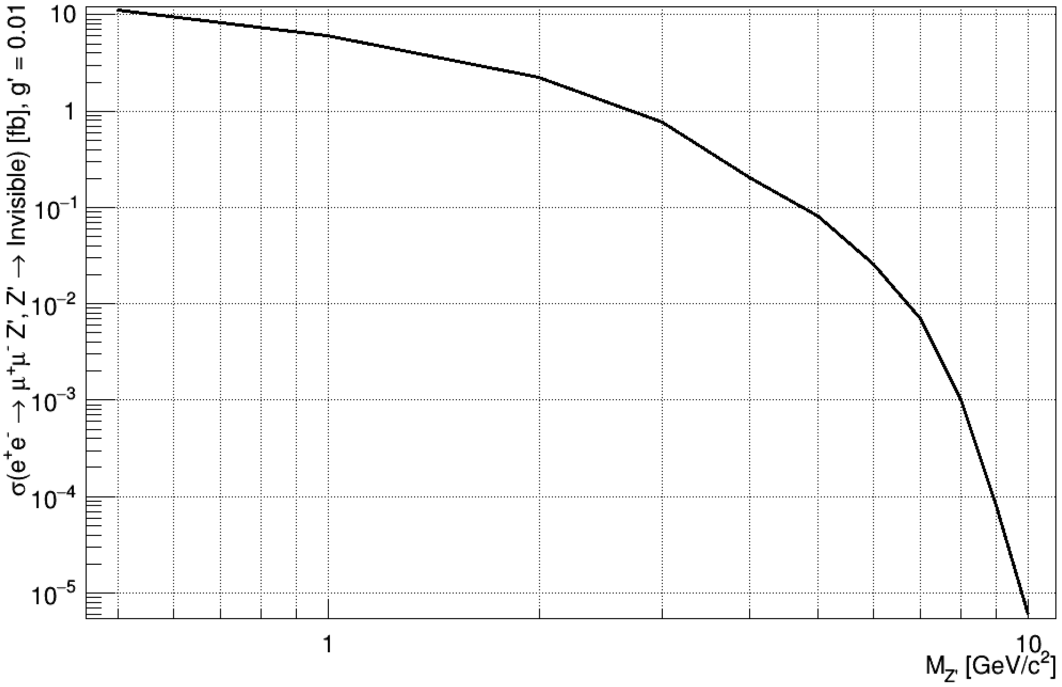

Figure 5.1: Cross section in fb of the process $e^+e^- \rightarrow \mu^+\mu^- Z'$ ($Z' \rightarrow$ Invisible) for different Z' mass hypothesis in the mass range [0.5,10] GeV/c^2. The Z'-muons coupling constant is assumed to be $g' = 0.01$. The cross section vanishes while Z' masses reach the energy $\sqrt{s} = 10.58$ GeV/c^2.

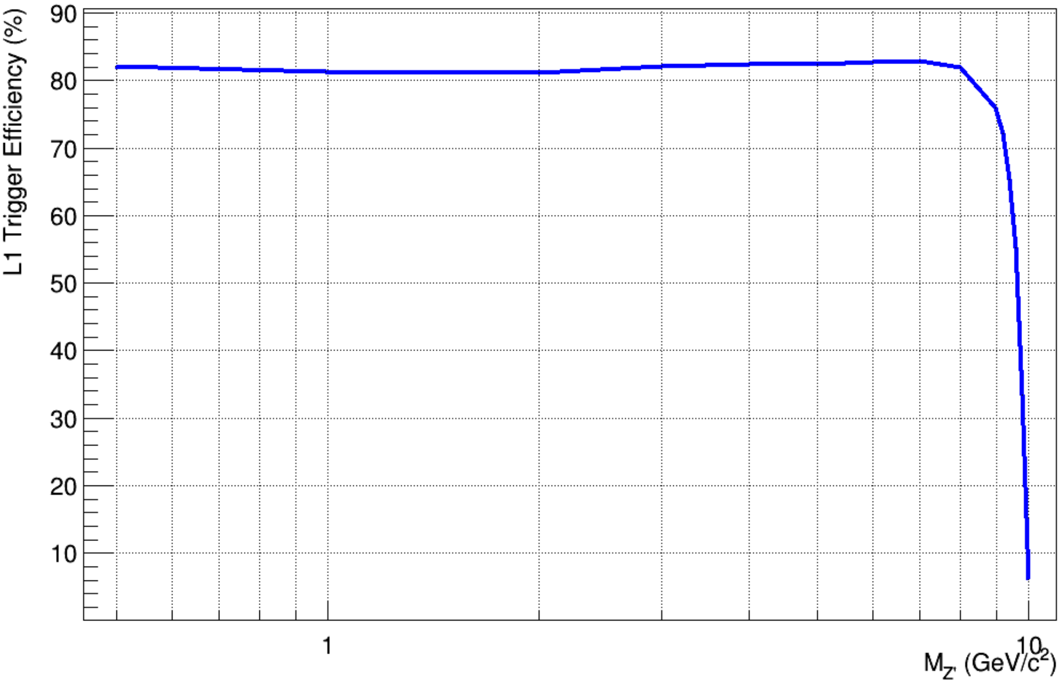

Figure 5.2: L1 Trigger efficiency for the process $e^+e^- \rightarrow \mu^+\mu^- Z'$ ($Z' \rightarrow$ Invisible), obtained from MC simulations. The efficiency evaluated on MC samples is around 82% for Z' masses up to 8 GeV/c^2.

fication probability larger than 0.9, the number of tracks in the ROE equal to zero and the invariant mass of the muon pair $M_{\mu\mu} < 10.2$ GeV$/c^2$. The background recoil mass distribution is indistinguishable from the signal process recoil mass distribution for small masses of the Z'. Finally, Figure 5.5 shows some examples of fitted recoil mass distribution for different hypothesis of the Z' mass. The fitting function is the sum of three Gaussian distributions, which corresponds to the typical MC resolution function according for the three contributions from the core of the distribution, the bad reconstructed candidate population and the outliers.

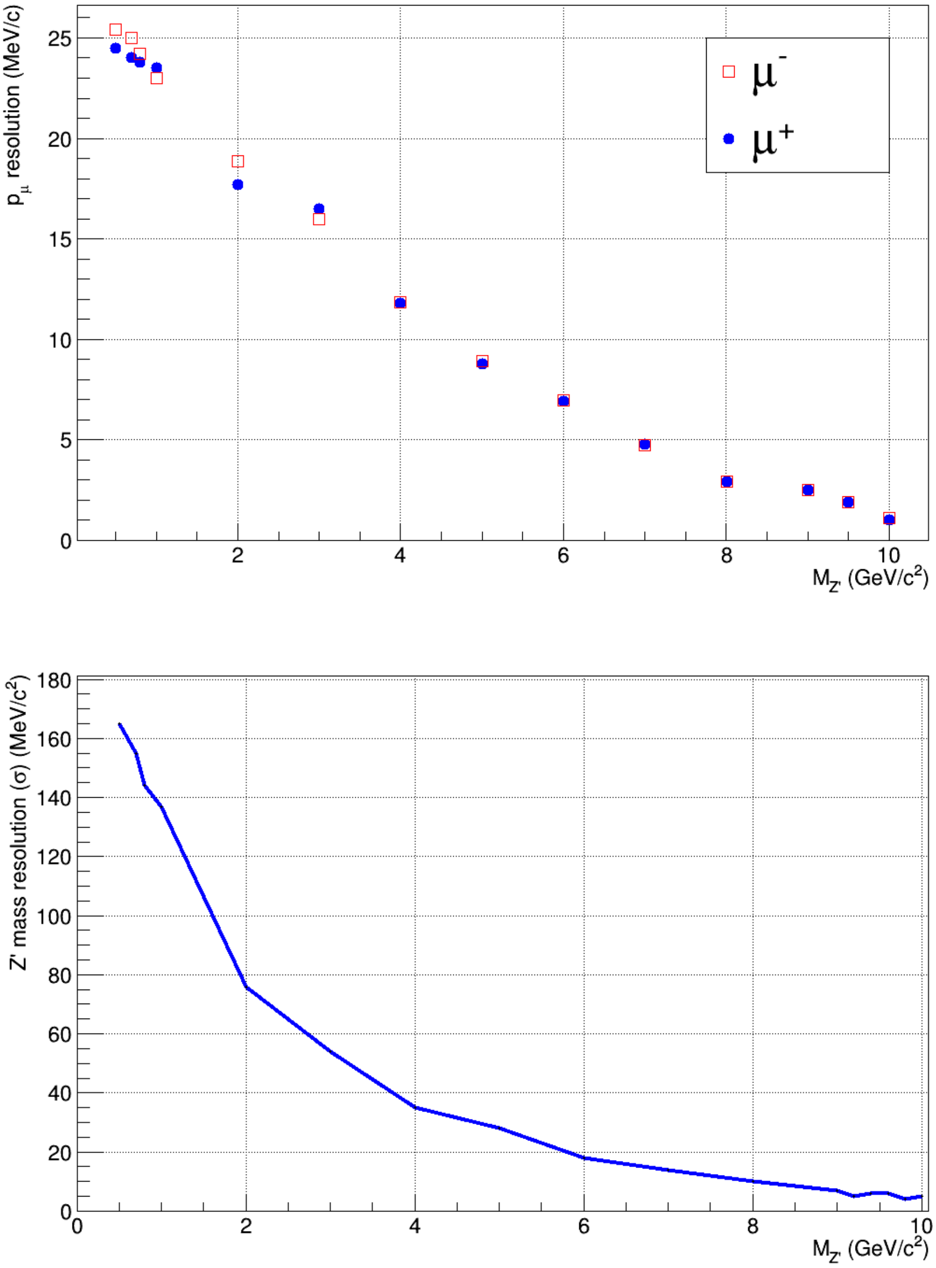

Figure 5.3: Above: Muon momentum resolution depending on the Z' mass. This are preliminary results obtained from the RMS of the muon momentum resolution distribution obtained using the MC truth, i.e. $\sigma = p_{rec} - p_{truth}$ where p_{rec} is the reconstructed muon momentum and p_{truth} is the muon momentum from the MC truth. The trend of the curve is as expected. Below: Mass resolution of the Z' mass. The mass resolution is the σ obtained from a Gaussian fit of the Z' mass distribution. The trend of the curve is as expected.

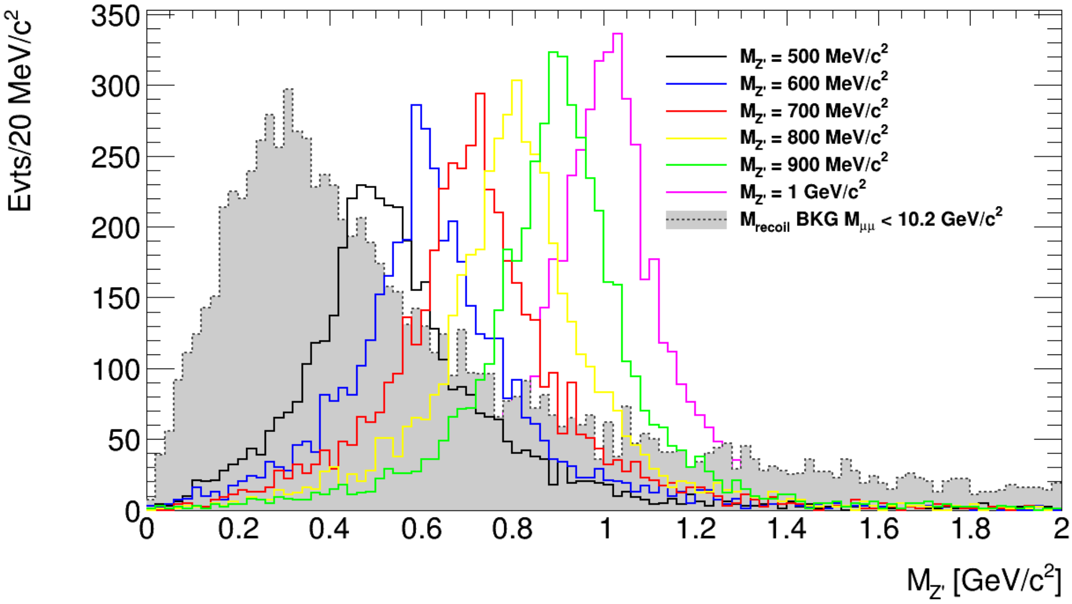

Figure 5.4: Recoil mass distributions of signal events for $M_{Z'} < 1$ GeV/c^2 and of the background process $e^+e^- \to \mu^+\mu^-\gamma$. In particular signal samples consist of 10 thousand events and the background consists of 100 thousands events, cross sections are not taken into consideration. The selection applied to samples are muon-ID higher than 90%, number of tracks in the ROE = 0 and $M_{\mu\mu} < 10.2$ GeV/c^2. The selection on the muon pair invariant mass reduce the $\mu\mu(\gamma)$ final state background, which peaks at low masses, and limits the Z' mass for low Z' mass hypothesis. The graph shows that the recoil mass distribution of the background is similar to the recoil mass of the signal for low Z' masses.

5.2 Background processes

The background processes expected for this analysis are QED processes in which there are two muons in the final state plus other particles that escape the detector. For example, one of the most relevant contribution comes from radiative electron-positron annihilation into a pair of muons, $e^+e^- \to \mu^+\mu^-(\gamma)$, whose experimental signature corresponds to two charged tracks identified as muons and a number of photons in the final state ≥ 1. Photons can be produced as initial state radiation (ISR) or final state radiation (FSR) and most of them are radiated at small polar angles θ_γ, escaping the acceptance of the detector and therefore appearing as missing mass.
A more complicated background process is $e^+e^- \to \tau^+\tau^-(\gamma)$ in which $\tau^\pm \to \mu^\pm\nu_\mu(\bar{\nu}_\mu)$. In this case, neutrinos are produced from the decays of τ leptons and since they are not detected, they can mimic a signal, appearing as missing mass. Other possible background sources are QED processes with four leptons in the final state, where at least two of them are muons and the second couple escapes the detector acceptance: for example $e^+e^- \to e^+e^-\mu^+\mu^-$ and $e^+e^- \to \mu^+\mu^-\mu^+\mu^-$. Also hadronic processes $e^+e^- \to q\bar{q}\gamma, (q = u, d, s, c)$ could represent a source of background, if pions produced by hadronization are misidentified as muons and the photon in the final state escapes the detector. Finally, another possibility is the emission of high-energy ISR photons that causes e^+e^- annihilation in the J/ψ narrow resonance, which consequently decays in two muons, and the high-energy ISR photons escape the detector.

The main background processes considered for the analysis are listed in the following:

- $e^+e^- \to \mu^+\mu^-(\gamma)$. Photons are mostly emitted as ISR because the probability

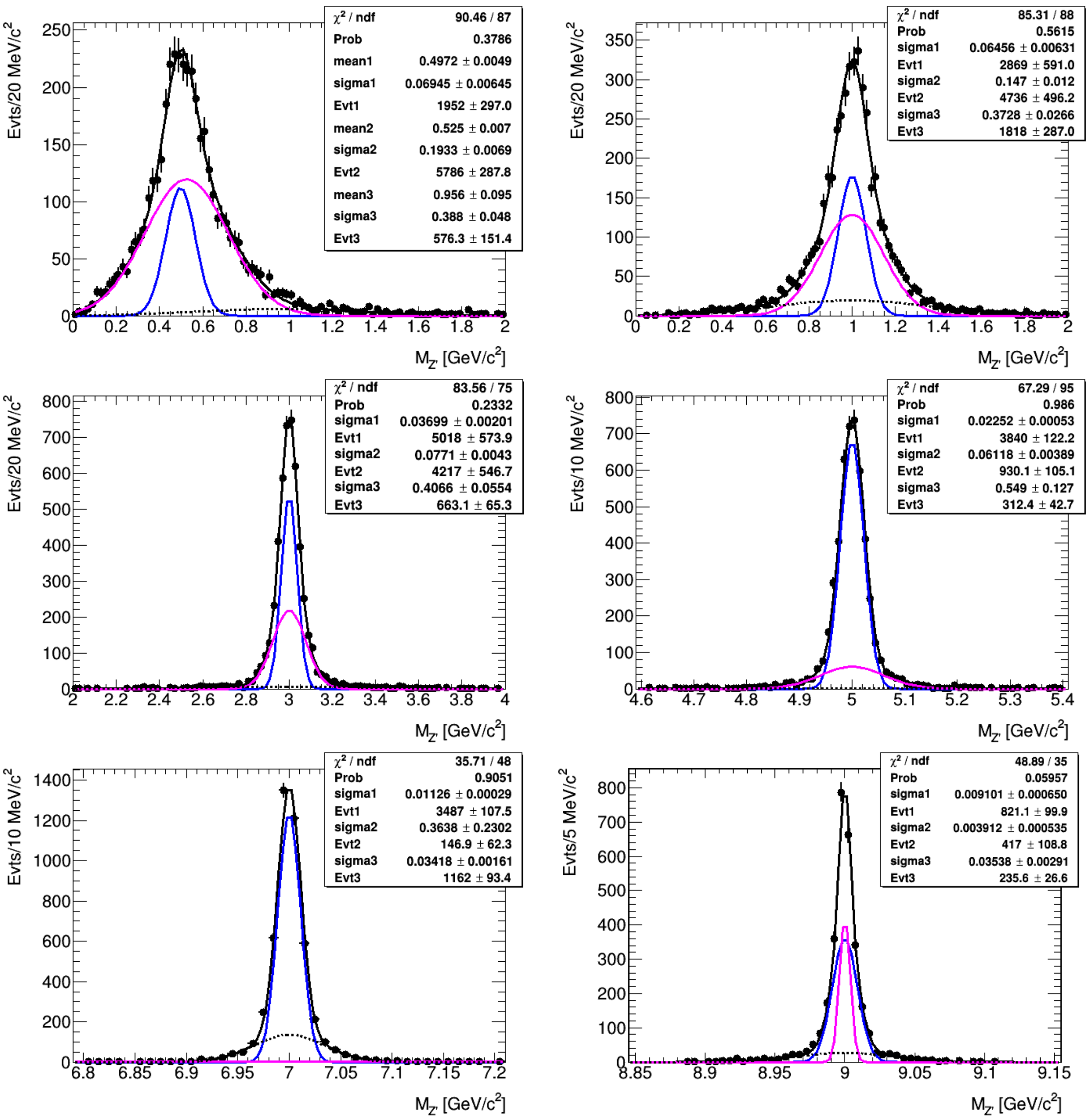

Figure 5.5: Recoil mass distribution of signal events for different Z' mass hypothesis. The recoil mass peaks at the Z' mass value. Distributions are fitted with the sum of three Gaussian, fixing the value of the Z' mass in the fit. The mass is not fixed in the case of $M_{Z'} = 500$ MeV/c^2, because at low masses resolution effects come into play and muons are reconstructed worse, causing a tail at high masses. Graphs show as the mass resolution improves as the Z' mass increases.

for the electron bremsstrahlung is favored with respect to that for muons, due to its dependence on the inverse squared mass ($\sim 1/M^2$) of the radiating particle. Therefore FSR is expected to be suppressed by a factor of $m_e/m_\mu^2 \sim 2 \cdot 10^{-5}$ with respect to ISR. Undetected photons appear as missing mass, affecting the muon pair invariant mass which results smaller than the $M_{\Upsilon(4S)}$. The cross section of this process is around 1 nb at the center of mass energy of the $\Upsilon(4S)$ resonance, so around three order of magnitude higher than the expected cross section of the process of interest. The recoil mass, $M_\gamma^2 = 0$, of this process is expected to peak at zero because of the emission of low-energy photons, so it affects the sensitivity of detection if the Z' boson have a small mass. However, being the sensitivity on small Z' masses already limited by poor resolution, this analysis focuses on $M_{Z'} \geq 1$ GeV where the background due to $e^+e^- \to \mu^+\mu^-(\gamma)$ is easily rejectable.

- $e^+e^- \to \tau^+\tau^-(\gamma), \tau \to \mu\nu\nu$. Also in this case the photon is almost exclusively emitted as ISR. The mean lifetime of tauons is around $2.9 \cdot 10^{-13}$ s, while is mass is around $m_\tau = 1.78$ GeV/c^2. Considering the boost of the center of mass of $\beta\gamma_{CM} = 0.28$, the tauons produced in electron-positron annihilation decay at hundreds of μm from the IP. In the laboratory frame, the cross section of the process is around 1 nb at the $\Upsilon(4S)$ energy peak and the branching ratio of muonic decay of the τ is around 17%, so the probability for both τ to decay to $\mu\nu\nu$ is around 3% . Neutrinos in the final state are lightest particles and they carry the highest momenta, producing a large missing mass in the event, indeed the recoil mass for this process is uniformly distributed and dominates for $2 \lesssim M_{recoil} \lesssim 7$ GeV/c^2, which is expected to affect high Z' masses. The background due to this process is more difficult to reject compared to background due to $\mu\mu(\gamma)$ final state processes because neutrinos simulate very well high Z' masses. Background events due to $\tau\tau(\gamma)$ final states can be reduced in *Phase*-3 data thanks to the full vertex detector, which allows to reconstruct the tauon decay vertex and reject events with muons that do not come from the IP.
- $e^+e^- \to e^+e^-\mu^+\mu^-$. This process has a cross section of around 18.9 nb, as estimated by the event generator used in the simulation. However, requiring at least that two tracks are inside the acceptance of the detector and with a minimum momentum of 100 MeV/c it is possible to reduce the cross section of a factor 0.25. Electrons that escape the detectors appear as missing mass, resulting in a recoil mass peak at high masses ($M_{recoil} \sim 8$ GeV/c^2).

Other processes considered are $e^+e^- \to \mu^+\mu^-\mu^+\mu^-$ and $e^+e^- \to J/\psi \to \mu^+\mu^-(\gamma)$. The former have a cross section of 0.3 fb, as estimated by the event generator without requiring any particular selection on the particles in the final state, while the latter has a cross section of around 10 pb, as obtained from the event generator by limiting the invariant mass of the muon pair around the J/ψ mass, $2.9 < M_{\mu\mu} < 3.2$ GeV. Both are estimated to be negligible for the analysis, in particular the background source that involve the J/ψ is negligible if events with $M_{\mu\mu} \sim M_{J/\psi}$ are excluded. For a good background rejection it is fundamental to achieve optimal PID performance and minimize the background contribution coming from misidentification of pions which are wrongly reconstructed as muons. For this purpose the tuning of the PID variable, defining the probability for a charged track to be respectively a muon (muon-ID) or a pion (pion-ID) is required.

5.3 Generation and reconstruction of the process $e^+e^- \to J/\psi(\gamma), J/\psi \to \mu^+\mu^-$

The process $e^+e^- \to J/\psi\gamma, J/\psi \to \mu^+\mu^-$ has been used to evaluate the expected performances of the detector during the *Phase*-2 commissioning for what concerns the mass resolution on the J/ψ mass and the momentum resolution on muons of a known energy. Since the J/ψ mass is known, the mass distribution can be fitted fixing the mass of the particle. In this way the fit is more stable and the resolution is the only free parameter to extract from it. Furthermore, the decay width of the J/ψ is around 93 keV and it is negligible compared to the experimental resolution. For this reason the distribution $M_{J/\psi,truth} - M_{J/\psi,rec}$ gives exactly the experimental resolution, which can be obtained from a Gaussian fit.

Events have been simulated using the EvtGen generator [86]. EvtGen is a MC generator originally designed for the simulation of the physics of B and D meson decays. This generator is able to take into account cascade decays involving multiple vertices, to handle a wide range of spin configurations and it includes also $\mathcal{CP}$-violation and mixing effects. The generator is controlled by a *Decay.dec* script, in which the decays to be simulated are written in the appropriate syntax. In the *.dec* file it is possible to set the desired branching fractions and the desired model, for example scalar, vector and tensor decays or leptonic, semileptonic and baryonic decays. EvtGen can be configured to employ external generators, for example PYTHIA to generate inclusive decays [87] and PHOTOS to introduce radiative corrections [88].

EvtGen has been compared with PHOKHARA, which is another generator that allows to generate processes including narrow resonances and to limit the invariant mass of the muons in the final state around the J/ψ mass. They showed similar performances and the same angular distributions.

The MC sample used to check the detector performances consists of the full detector reconstruction and simulation of 25 thousands events $e^+e^- \to J/\psi\gamma, J/\psi \to \mu^+\mu^-$. The events are reconstructed by requiring probability for being identified as muon higher than 90% and imposing a loose selection on the J/ψ candidate, which consists of applying the following requirements: a dimuon invariant mass in the range $2.9 < M_{J/\psi} < 3.2$ GeV/c^2; the energy of the ISR photons $E_\gamma > 0.075 GeV$ and no tracks in the ROE. In the reconstruction, the mass vertex fit and the MC truth match, which checks if the reconstructed particles match with the generated particles, have also been applied.

Figure 5.6 shows the J/ψ mass resolution and the muon momentum resolution obtained. The resolution is defined as the width of the $M^{truth}_{J/\psi} - M^{rec}_{J/\psi}$ distribution fitted with the sum of three Gaussians, where $M^{truth}_{J/\psi}$ is the mass of the MC truth and $M^{rec}_{J/\psi}$ is the mass reconstructed, and it is around 10 MeV. It is only a preliminary check to evaluate the performances of the reconstruction. If the resolution of the dimuon candidate mass would have been larger than 100 MeV, it is not expected to do better on the recoil mass resolution, which depends on the dimuon invariant mass.

5.4 Monte Carlo samples

For the background studies, each of the background processes of interest for this analysis, already discussed in Section 5.2, have been simulated as MC samples, for a total number of produced events corresponding to an integrated luminosity of 10 fb^{-1}. The interaction with the detector is then simulated by using the *Geometry and Tracking 4* (GEANT4) package [89] and the same reconstruction performed on data is applied. GEANT4 is a toolkit that simulates the passage of particles through matter and it is composed by different tools that allow to simulate the geometry of the detector, the passage of particles through matter, their interactions and their decay processes, the response of the detector crossed by particles and it provides the information of the simulated runs with the configuration used in the experiment. Events for the processes $e^+e^- \to \mu^+\mu^-(\gamma)$ and $e^+e^- \to \tau^+\tau^-(\gamma)$ have been generated using the FORTRAN-based KKMC generator [90], which is the default generator to simulate two-fermion final states $l\bar{l}, l = \mu, \tau, \nu$ and the $q\bar{q}$ continuum at the $\Upsilon(4S)$ energy peak. KKMC generates also QED corrections of multiphoton ISR, FSR and *Initial-Final-State Interference* (IFI) and it includes also electroweak corrections. The theoretical precision of cross sections calculated by KKMC for lepton-pair

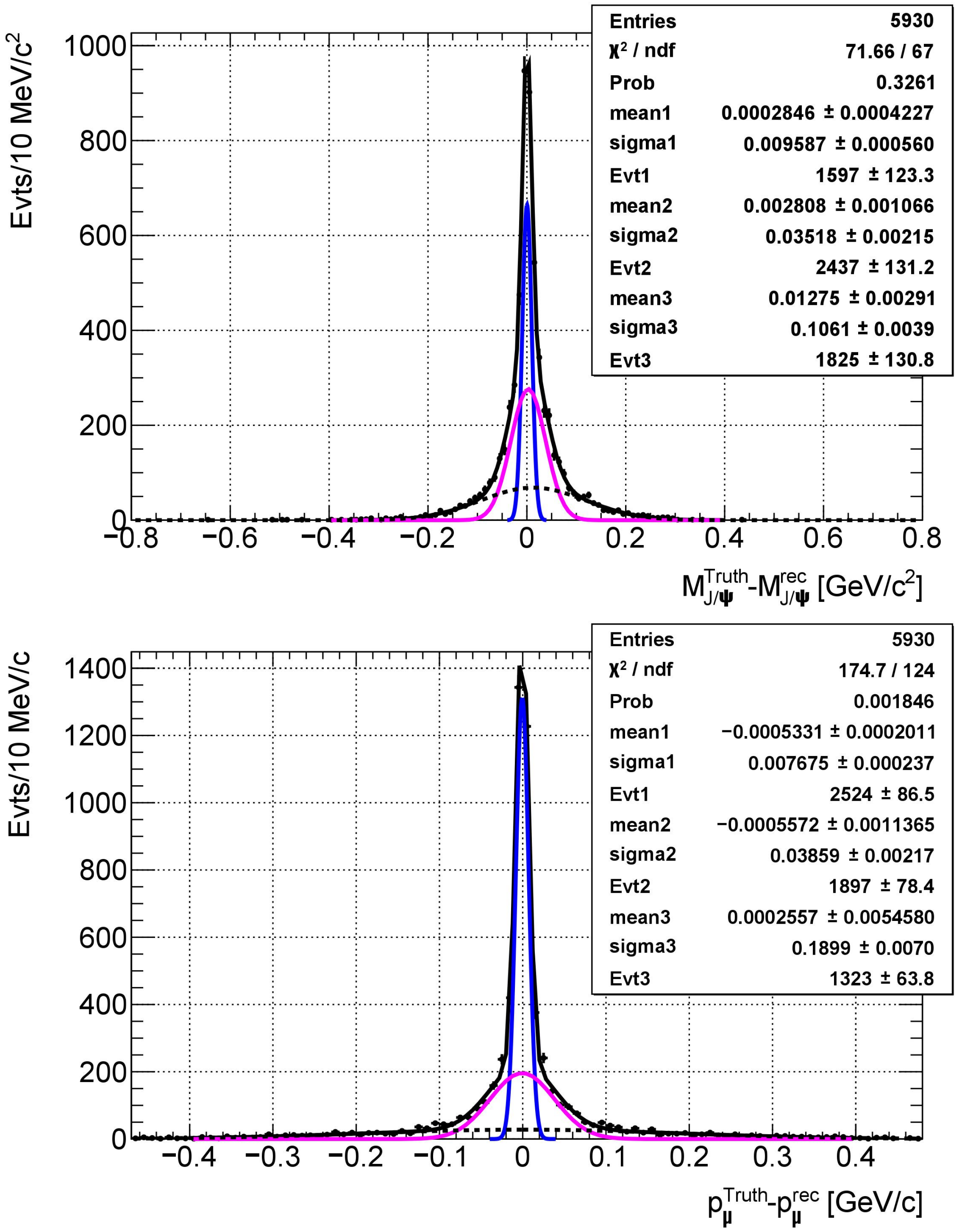

Figure 5.6: Above: J/ψ mass resolution. The graph shows the difference between the J/ψ mass obtained by the MC truth and the J/ψ mass reconstructed from the muon invariant mass. The distribution has been fitted through the sum of three Gaussian distributions, one for the well reconstructed muons, one for the core of the distribution and one for the outliers. The interesting resolution is peak resolution, which is around 10 MeV. Below: muon momentum resolution for muons coming from the J/ψ. The distribution is the difference between the muon momenta obtained by the MC truth, p_{μ}^{Truth} and the reconstructed muon momenta p_{μ}^{rec}. The distribution has been fitted with the sum of three Gaussian distributions and the resolution of the central peak, corresponding to well reconstructed muons, is around 5 MeV/c.

final states is assessed to be better than 0.5% for final states within the detector acceptance and produced at the $\Upsilon(4S)$ energy peak or at higher energies. For $q\bar{q}$ final states a larger uncertainty is expected but not quantified yet. Other generators for the $\mu^+\mu^-(\gamma)$ final states are BABAYAGA@NLO, which have a comparable precision at the $\Upsilon(4S)$ energy peak, and PHOKHARA, which have a comparable precision at the $\Upsilon(4S)$ peak if at least one photon with an energy in the center of mass higher than 50 MeV is simulated in the event.

BABAYAGA@NLO is the default FORTRAN-based generator used to simulate Bhabha events (e^+e^- final states), exclusive $\gamma\gamma$ and $\mu^+\mu^-$ final state events at all energies, including narrow resonances [91]. It generates multi-photon ISR, FSR and IFI and it includes electroweak corrections at the *Leading Order* (LO). Cross sections are estimated by the generator with a theoretical precision of about 0.1% for e^+e^- and $\gamma\gamma$ final states and 0.5% for $\mu\mu$ final states at the $\Upsilon(4S)$ energy peak.

PHOKHARA is a FORTRAN-based generator [92] [93] and is used to simulate different leptonic and hadronic final states both with and without photon emission. The generator gives also the possibility to include narrow resonances as the J/ψ and $\Psi(2S)$. For the $\mu^+\mu^-$ final state, *Next-to-Leading Order* (NLO), ISR and FSR with the simultaneous emission of one ISR and one FSR photon are available, and also the full *Next-to-Next-to-Leading Order* (NNLO)[1] corrections including the IFI.

For tuning purpose, different configurations of the PHOKHARA generator have been tested for the generation of the samples used in the resolution studies for the production of the resonant dimuon final state $e^+e^- \rightarrow J/\psi\gamma, J/\psi \rightarrow \mu^+\mu^-$. Finally, it was decided to use only the NLO configuration with ISR, because corrections introduced by the NNLO and IFI are negligible with respect to uncertainties introduced by the parameters setting.

Always for tuning purposes, three different samples of 10 thousand events for the process $e^+e^- \rightarrow \mu^+\mu^-(\gamma)$ have been simulated by using the above mentioned MC generators. In order to reproduce the same cross sections some adjustment was needed for the parameters of the simulation with PHOKHARA and BABAYAGA@NLO. The result from KKMC generator which gives a cross section $\sigma = 1.13 \pm 0.02$ nb, is assumed as reference and corresponds to that reported in the *Belle II Theoretical Interface Platform* [73]. After the tuning, the cross sections given by the three MC generators are consistent within their uncertainty: the cross section estimated by KKMC is $\sigma = 1.13 \pm 0.02$ nb, BABAYAGA@NLO and PHOKHARA estimate a cross section respectively of $\sigma = 1.08 \pm 0.05$ nb and $\sigma = 1.15 \pm 0.04$ nb. Kinematics distributions have been compared and validated for the three samples and after the tuning they agree as expected. Finally the KKMC generator has been chosen, because it is faster and it is the default generator for this kind of processes, so it does not require a specific parameter tuning.

The process $e^+e^- \rightarrow e^+e^-\mu^+\mu^-$ has been generated using the FORTRAN-based AAFH generator [94], which simulates four-fermion final states, also including all LO QED diagrams and their interference, but neither higher order QED corrections nor weak corrections. The highest event rates at Belle II energies arise from $e^+e^- \rightarrow e^+e^-e^+e^-$ and $e^+e^- \rightarrow e^+e^-\mu^+\mu^-$, the former has a cross section of 40.8 nb while the last has a cross section of 18.9 as already said.

Table 5.1 summarizes the MC samples produced for the analysis.

---

[1] The *Leading-Order* terms in a model are those with the highest order of magnitude. The NLO terms are those with the higher order of magnitude after the LO, and the next set of terms after the NLO is called NNLO.

Kind of process	Process	MC sample size	Genarator
Signal	$e^+e^- \to \mu^+\mu^- Z'(Z' \to \text{Invisible})$	10k Evts, $M_{Z'} \supset [0.5, 10]$ GeV/c^2	MadGraph5
Background	$e^+e^- \to \mu^+\mu^-(\gamma)$	10 fb^{-1}	KKMC
	$e^+e^- \to \tau^+\tau^-(\gamma)$	10 fb^{-1}	KKMC
	$e^+e^- \to e^+e^-\mu^+\mu^-$	10 fb^{-1}	AAFH
Control process	$e^+e^- \to J/\psi\gamma, J/\psi \to \mu^+\mu^-$	25k Evts	EvtGen

Table 5.1: Summary of MC samples used in the analysis. Signal MC samples of 10k events have been produced for $M_{Z'} = 0.5, 1, 2, 3, 4, 5, 6, 7, 8, 9, 10$ GeV/c^2. For preliminary tests and for the validation of generators, many more samples have been produced.

Chapter 6

Event selection and sensitivity estimate

In this chapter the studies for the background rejection will be reported. For a preliminary background reduction, a preselection on the reconstructed events has been applied and it will be described in the first section. In the same section, the recoil mass distribution after the preselection for both background and signal MC samples will be shown. In the second and third sections, a description of the potential discriminating variables and the method used to optimize the selection will be given. The optimization method consists of maximizing the *Punzi Figure of Merit* as explained in this section. In the fourth section, the sensitivity to the parameters of the model, as estimated on the results from the selection optimization will be discussed. Finally, in the last section will be reported some recent results obtained at *Belle*II using the data set corresponding to 505 pb^{-1}, collected in *Phase*-2, and a very preliminary MC-data comparison for this analysis

6.1 Event reconstruction and preselection

The event reconstruction is performed in the same way for both simulated signal and background samples and consists of requiring two tracks identified as muons with a probability (muon-ID) higher than 0.7, the χ^2 probability of the fit to the tracks higher than 0.001 and the dimuon candidate to be inside the detector acceptance, defined as the range $17^o < \theta_\mu < 150^o$ for the polar angle of the track in the center of mass reference system. Furthermore, the two tracks must come from the IP, i.e. they are characterized by $z0 < 2$ cm and $d0 < 0.5$ cm, where $z0$ is the distance of the track from the IP along the beam axis, while $d0$ is the distance of the track from the IP in the transverse plane (x, y), both are estimated from the fit to the track as final result from the track finding algorithm.
All other particles are reconstructed int the *Rest-Of-Event* (ROE), where only photons with an energy higher than 100 MeV and inside the acceptance of the detector are reconstructed, while photons with an energy lower than 100 MeV, which are mostly coming from beam background, are ignored because potentially not dangerous and very different from ISR photons that can mimic the signal peak.
The vertex fit to the muon tracks selected is performed with the *Reconstruction of vertices in Abstract Versatile Environments* (RAVE) [95] package, which is a tool-kit for vertex reconstruction.
After the reconstruction, fake candidates are rejected by applying the following preselec-

tion, which consists of the following requirements:

- the energy of ECL clusters associated with the tracks is lower than 1 GeV since the purpose of the selection is to select events with two muon tracks, and muons release a small energy in the ECL;
- a muon-ID > 0.9, i.e. the probability of the charged to be muons is higher than 90%;
- the direction of the recoil with respect to the muon pair points in the acceptance of the barrel ECL, i.e. the polar angle of the recoil is included in the range [33^o, 128^o]. This selection improves the reconstruction efficiency of high energetic photon events that have a photon within a cone of 15^o with respect to the direction of the recoil, which are those events where the photon can be identified with the recoil. This kind of events are rejected;
- the extra energy in ECL, which is the energy released in the ECL in the event not associated to the reconstructed particles, is lower than 1 GeV, in order to reject events with particles releasing energy in the calorimeter other than the muon pair tracks.
- No additional tracks must be found in the ROE.

Considering the L1 trigger efficiency on the reconstruction of signal events, which is around the 82% for Z' masses up to 8 GeV/c^2, as shown in Figure 5.2, the total signal efficiency of this pre-selection is around 35%. Since the pre-selection described here is not optimized yet, the final pre-selection that will be used for this analysis could be changed.

The recoil mass distribution of background MC samples for the three main considered background processes with the pre-selection applied is shown in Figure 6.1. The graph confirms the considerations in the Section 5.2: the recoil mass of the $e^+e^- \to \mu^-\mu^+(\gamma)$ events peaks at small recoil masses since the invariant mass of real photons is zero, the recoil mass of the $e^+e^- \to \tau^-\tau^+(\gamma)$ events mostly contributes between 2 GeV/c^2 and 7 GeV/c^2 since neutrinos are undetected, while the recoil mass distribution of the $e^+e^- \to e^+e^-\mu^-\mu^+$ events contributes for high masses, higher than 7 GeV/c^2, since electrons carry the highest momentum and they are out of the acceptance of the detector, being therefore reconstructed as the missing mass. Figure 6.2 shows the recoil mass distributions for MC signal samples produced for eight different Z' mass hypothesis in the range [1,8] GeV/c^2, which are the only masses considered in the analysis since the poor resolution at low masses affects negatively the sensitivity to the signal. On the other hand, for masses higher than 8 GeV/c^2 the cross section becomes too small and the L1 trigger efficiency decreases quite quickly, as explained in Section 5.1.

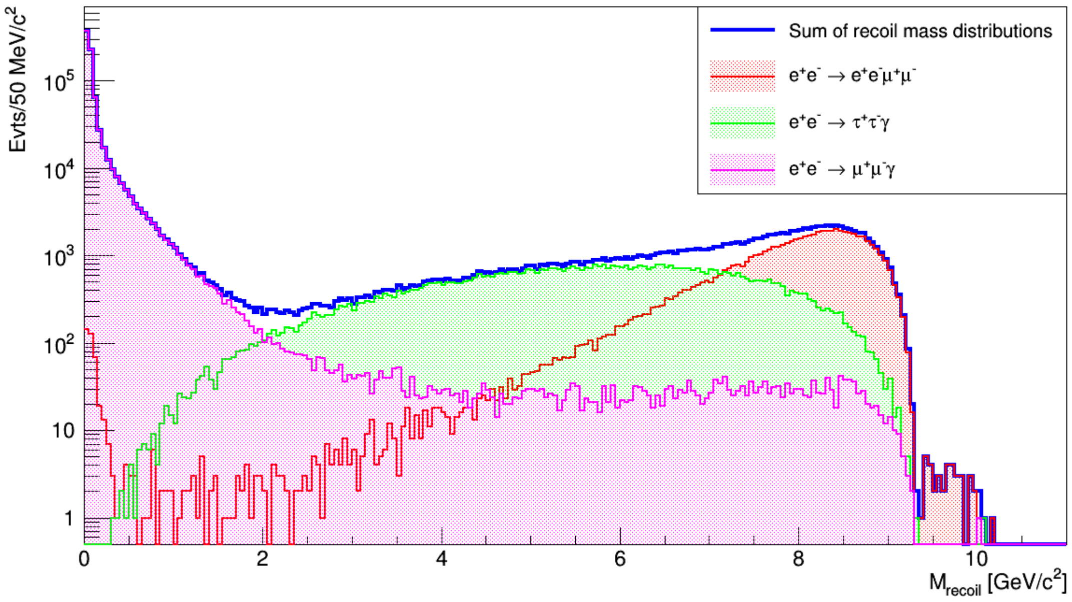

Figure 6.1: Recoil mass distribution of MC background samples after the preselection described in the text. The magenta curve is the recoil mass distribution of the process $e^+e^- \to \mu^+\mu^-(\gamma)$, while the green and the red curves are the recoil mass distributions respectively of the processes $e^+e^- \to e^+e^-\mu^+\mu^-$ and $e^+e^- \to \tau^+\tau^-(\gamma)$. The blue curve is the sum of the recoil mass distributions of the three background processes. The distributions are evaluated at the integrated luminosity of 10 fb^{-1}.

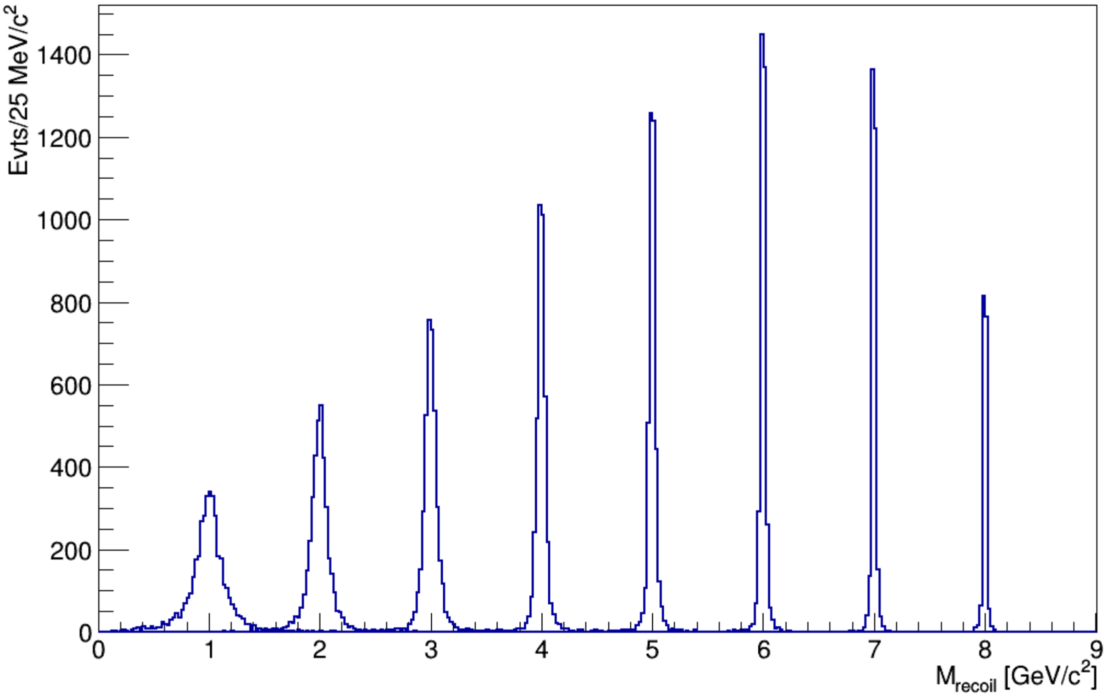

Figure 6.2: Recoil mass distribution of signal events for $M_{Z'} = 1, 2, 3, 4, 5, 6, 7, 8$ GeV/c^2 after the pre-selection. The signal samples used to produce this plot consists of 10 thousand events.

6.2 Discriminating variables

In order to further reject the background, several variables are being considered, but only two discriminating variables will be discussed here, the polar angle $\theta_{\mu\mu}$ and the transverse momentum $p_{T\mu\mu}$ of the dimuon candidate. Both variable emerged analysing the $e^+e^- \to \mu^+\mu^-(\gamma)$ background events, showing distributions with high discriminating power. The distributions of $\theta_{\mu\mu}$ and $p_{T\mu\mu}$ for signal and background events are shown in Figure 6.3. Signal event distributions are normalized at 1 while the background event distribution is normalized at 0.1, for what concerns the $\theta_{\mu\mu}$ distribution, and at 0.2, for what concerns the $p_{T\mu\mu}$ distribution, for the purpose of visibility and shape comparison. The polar angle of the dimuon candidate for background events peaks at small angles differently from signal events, in the same way the transverse momentum distribution for background events peaks at small values while for signal events it is distributed between 0 GeV/c and $\sim$ 5 GeV/c and for higher Z' masses hypothesis the distribution shift towards smaller values. In order to verify if they can be good discriminant variables between signal events and background events, the same distributions has been observed considering all background samples, Figure 6.4. The main difference between the distributions in this case and in the previous case where only $e^+e^- \to \mu^+\mu^-(\gamma)$ background events were considered is the tail at high $\theta_{\mu\mu}$ and $p_{T\mu\mu}$ values that in the previous case was not present, but in both cases background distributions peak at small $\theta_{\mu\mu}$ and $p_{T\mu\mu}$ values. The graphs have been obtained from MC samples reconstructed as explained in the previous section and with the pre-selection applied. The two considered variables indicate the direction of the dimuon candidate. The transverse momentum is the component of the momentum projected onto the transverse plane (x, y) perpendicular to the beam axis (z) and it is defined as $p_T = \sqrt{p_x^2 + p_y^2}$, where p_x and p_y are the momentum components of the dimuon candidate respectively along the x and y coordinate, while the polar angle θ is defined as $tan^{-1}(p_T/p_z)$, where p_z is the momentum component of the dimuon candidate along the z coordinate.

From the definition of the two variables, it is easy to see that they are correlated, for these reason only the transverse momentum will be considered for a preliminary selection.

In Figure 6.5, the correlation between the recoil mass distribution and the transverse momentum for signal (above) and background events (below) is shown. The graph shows that the recoil mass does not depend on the transverse momentum of the dimuon candidate for signal events, while it peaks at small transverse momentum values for background events, so being a good variable for signal-background separation.

The recoil mass distributions for the different considered background sources before and after the selection are shown in Figure 6.6. In particular, black points represent the total recoil mass distribution selecting events with $p_{T\mu\mu} > 1$ GeV/c while the orange points represent the same distribution for $p_{T\mu\mu} > 1.7$ GeV/c.

In order to optimize this selection requirement, it is necessary to choose a figure of merit and maximize it. Since this kind of analysis is a *search*, it has to be independent from any assumption on the signal cross section, which is unknown. For this reason the *Punzi Figure of Merit* has been chosen to optimize the selection [96].

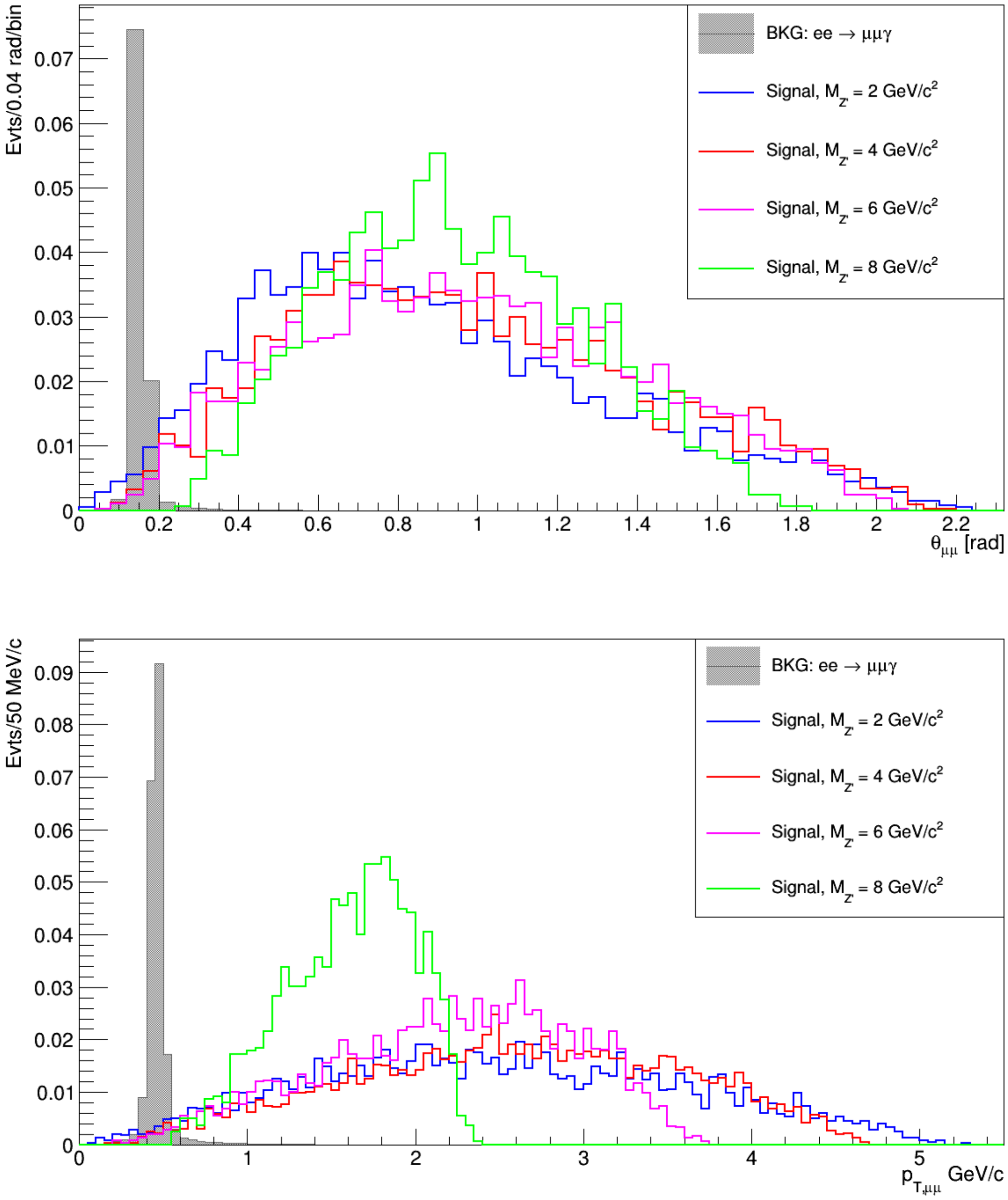

Figure 6.3: Above: Polar angle of the dimuon candidate $\theta_{\mu\mu}$ of $e^+e^- \to \mu^+\mu^-(\gamma)$ background events and of signal events for $M_{Z'} = 2, 4, 6, 8$ GeV$/c^2$. The $\theta_{\mu\mu}$ for background events peaks at small angles, while the $\theta_{\mu\mu}$ for signal events is distributed between $\sim 0^o$ and $\sim 130^o$. Below: Transverse momentum of the dimuon candidate $p_{T\mu\mu}$ of $e^+e^- \to \mu^+\mu^-(\gamma)$ background events and of signal events for $M_{Z'} = 2, 4, 6, 8$ GeV$/c^2$. The variable $p_{T\mu\mu}$ peaks at small value for background events while for signal events it has a different distribution.

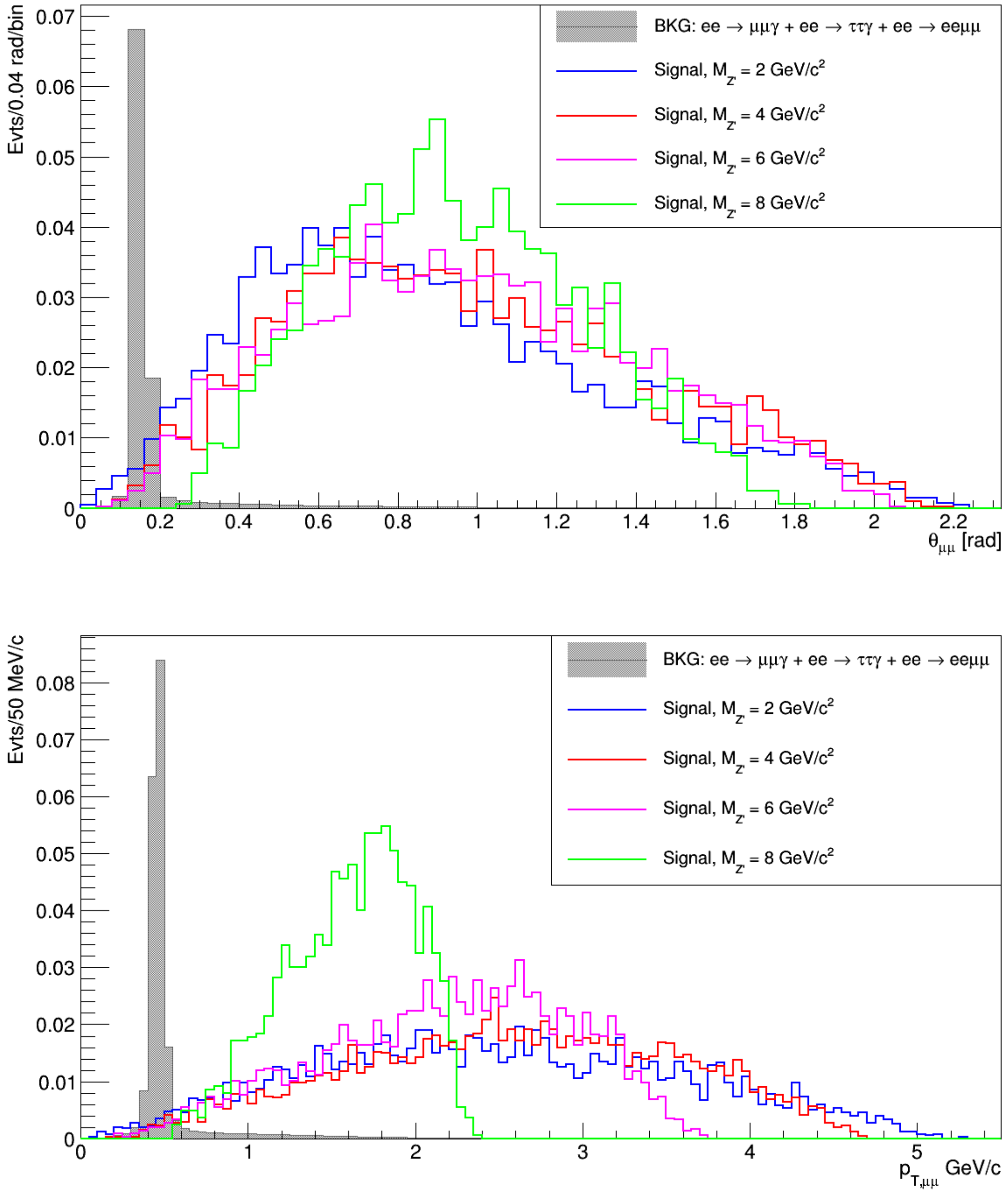

Figure 6.4: Above: Polar angle of the dimuon candidate $\theta_{\mu\mu}$ of $e^+e^- \to \mu^+\mu^-(\gamma)$, $e^+e^- \to \tau^+\tau^-(\gamma)$ and $e^+e^- \to e^+e^-\mu^+\mu^-$ background events and of signal events for $M_{Z'} = 2, 4, 6, 8$ GeV$/c^2$. The $\theta_{\mu\mu}$ for background events peaks at small angles, while the $\theta_{\mu\mu}$ for signal events is distributed between $\sim 0^o$ and $\sim 130^o$. Below: Transverse momentum of the dimuon candidate $p_{T\mu\mu}$ of $e^+e^- \to \mu^+\mu^-(\gamma)$, $e^+e^- \to \tau^+\tau^-(\gamma)$ and $e^+e^- \to e^+e^-\mu^+\mu^-$ background events and of signal events for $M_{Z'} = 2, 4, 6, 8$ GeV$/c^2$. The variable $p_{T\mu\mu}$ peaks at small value for background events while for signal events it has a different distribution.

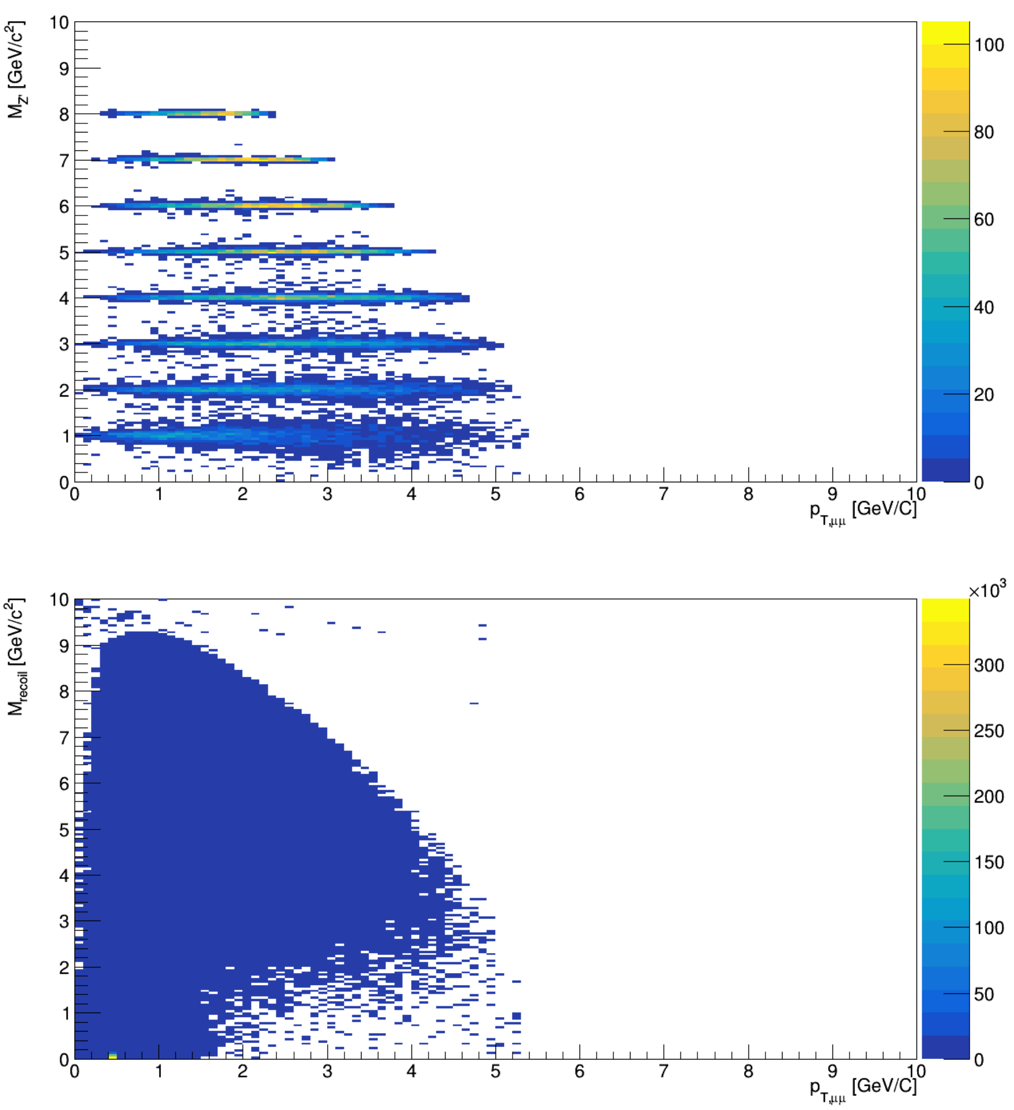

Figure 6.5: Above: Scatter plot of the recoil mass versus the transverse momentum of the dimuon candidate for signal events, which shows that there is not correlation between the two variables. Below: Scatter plot of the recoil mass and the transverse momentum of the dimuon candidate for background events, which shows a peak at $M_{recoil} = 0$ and small values of the transverse momentum.

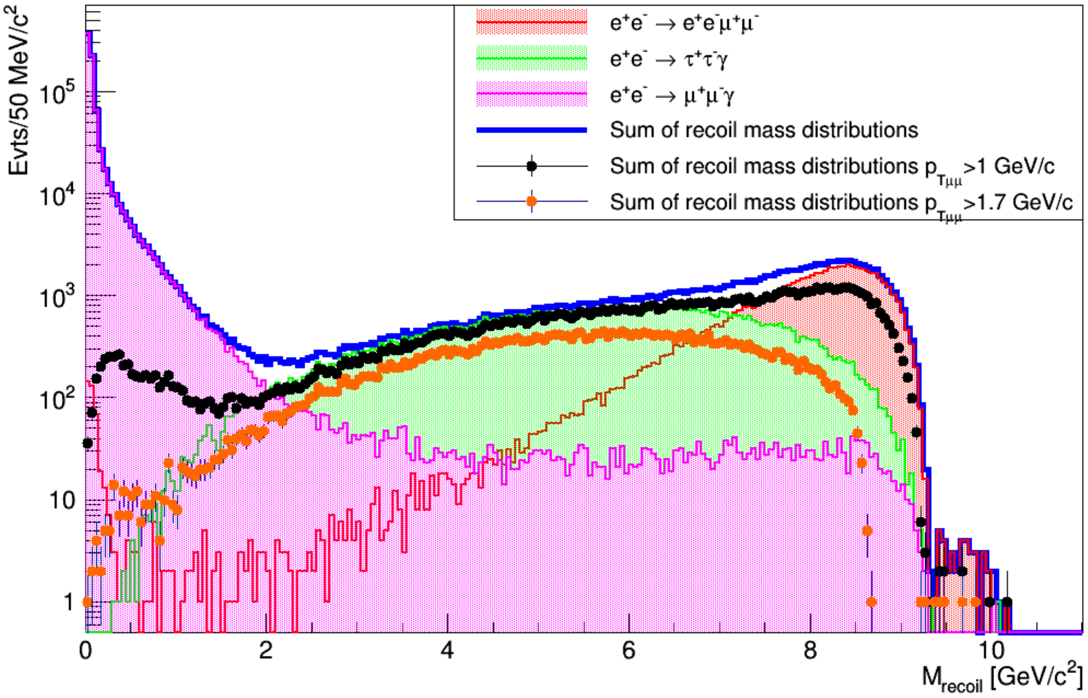

Figure 6.6: Recoil mass distribution of the MC background samples. The magenta curve is the recoil mass distribution of the process $e^+e^- \to \mu^+\mu^-(\gamma)$, while the green and the red curves are the recoil mass distributions respectively of the processes $e^+e^- \to e^+e^-\mu^+\mu^-$ and $e^+e^- \to \tau^+\tau^-(\gamma)$. The blue curve is the sum of the recoil mass distributions of the three background processes. The black points and the orange points represent respectively the total recoil mass distribution for $p_{T\mu\mu} > 1$ GeV/c and $p_{T\mu\mu} > 1.7$ GeV/c. The distributions are evaluated at the integrated luminosity of 10 fb^{-1}.

6.3 Figure of Merit

This analysis is a test of the hypothesis H, which is the current best theory that asserts that the measured observables are described by the background model only, against the hypothesis H', which is a new theory introducing a description of the observed distributions based on the sum of the background and signal models. Both the number of background and signal events depend on the selection t, while only the signal yield depends also on some additional parameters n and the goal is to estimate the maximum sensitivity of the experiment on the parameters n.

The sensitivity region of a *search* is defined by the *power function* $1 - \beta(n) > CL$, where β is the probability to reject the hypothesis H' even if it is true and CL is the confidence level $1 - \alpha$. The parameter α is the significance level of the test, which corresponds to the probability to reject the hypothesis H even if it is true. If the true value of the parameter n satisfies the *power function*, then the discovery probability performing the experiment is at least CL, otherwise if the experiment does not lead to the discovery then the results are some limits on n that exclude the region defined by the *power function* at the chosen CL. The region of the parameters defined by the *power function* assures to obtain a result, either the discovery of the process or the exclusion region of some parameters from which the process depends, and it is called *sensitivity region*.

This definition of *sensitivity region* is independent from the expected number for signal events and therefore from the cross section of the process analyzed, and allows, with some

assumptions [96], to define a figure of merit that depends only on the selection t.
Other possible figure of merit are:

- $S(t)/\sqrt{B(t)}$, where $S(t)$ and $B(t)$ are respectively the number of signal and background events expected by applying the selection t. This figure of merit has a linear dependence on the number of signal events, for this reason the optimal t does not depend on the number of signal events, but it diverges for $B(t) \to 0$.
- $S(t)/\sqrt{S(t)+B(t)}$ can be maximized only if the cross section of the searched process is known, since it depends on the total number of events as $1/\sqrt{S(t)+B(t)}$ and not by the number of signal and background events separately.

The optimization of the selection usually consists of maximizing the chosen figure of merit. Since in this case the cross section of the process is unknown, and can only be estimated from the MC simulation, assuming different hypotheses for the coupling constant g' and for the $M_{Z'}$, to optimize the selection a figure of merit that does not depends on the parameters of the model is needed. For this reason the figures of merit described above are not a good choice in this case.
A good figure of merit for this analysis is therefore the *Punzi Figure of Merit*, defined as $\epsilon(t)/[a/2+\sqrt{B(t)}]$, where t is the selection, $\epsilon(t)$ is the signal efficiency of the selection, a is the number of sigma corresponding to a Gaussian test at significance α. The significance level α and the number of sigma a have been set respectively to 0.1, which corresponds to choose a $CL = 90\%$, and 1.6, for this analysis.
It should be noticed that the *Punzi Figure of Merit* does not diverge for small values of $B(t)$ because of the correction term $a/2$ and does not depends from the cross section since in the signal efficiency computation the dependence on the σ_{signal} cancels out.

The optimization of the selection has been performed using the MC samples for different *mass bins*, that are defined as the 3σ-wide mass window centered at the generated Z' mass, where σ is the width of a single Gaussian fit to the signal peak. For the different Z' mass hypotheses considered in this analysis, *mass bins* are listed in Table 6.1. The number of background events used in the optimization of the selection for each mass are those entering the corresponding mass bin after the selection has been applied.

$M_{Z'}$ (GeV/c^2)	Mass bin (GeV/c^2)
1	[0.60, 1.40]
2	[1.76, 2.24]
3	[2.84, 3.16]
4	[3.88, 4.12]
5	[4.91, 5.09]
6	[5.94, 6.06]
7	[6.96, 7.04]
8	[7.97, 8.03]

Table 6.1: The mass bins defined for the different Z' mass hypotheses used in the analysis. They correspond to the 3σ-wide mass window centered at the generated Z' mass hypothesis, where σ is the width of a single Gaussian fit to the signal peak. They are used to evaluate the number of background events and the optimization of the selection performed using the transverse momentum of the dimuon candidate, mass by mass.

The signal efficiency of the selection performed using the transverse momentum of the dimuon candidate is calculated as the number of events after the selection divided by the number of events before applying the selection: $\epsilon(t) = S(t)/S(t=0)$, where $S(t)$ is the number of signal events as a function of the selection t. Some examples of the selection efficiency distributions are shown in Figure 6.7, where the selection requirement applied is $p_{T\mu\mu} > t$, where t varies from 0 GeV/c to 3 GeV/c, with 50 MeV/c steps. Since the $S(t)$ distribution is described by the binomial probability density function, indeed a signal event either passes the selection or does not, as a consequence also the efficiency is distributed as a binomial variable and its uncertainty is calculated as $\delta\epsilon(t) = \sqrt{\epsilon(t)(1-\epsilon(t))/S(t=0)}$.

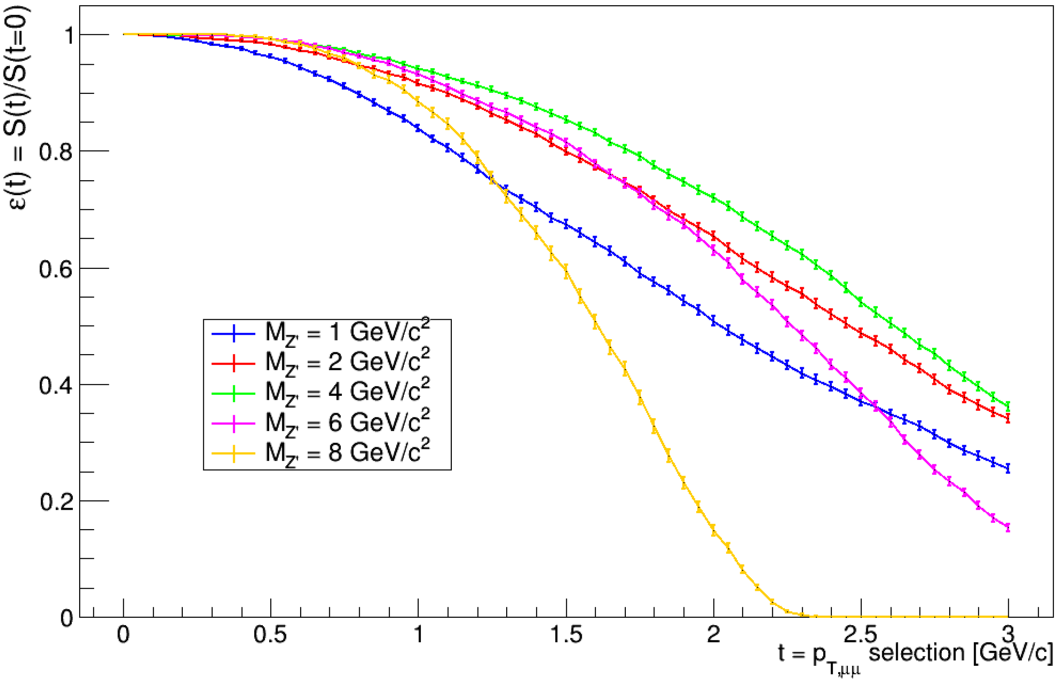

Figure 6.7: Efficiency $\epsilon(t) = S(t)/S(t=0)$ in function of the selection $0 < t < 3$ GeV/c, for different Z' mass hypotheses considered in the analysis. The efficiency uncertainty is computed as $\delta\epsilon(t) = \sqrt{\epsilon(t)(1-\epsilon(t))/S(t=0)}$.

Some examples for different mass hypotheses and different mass bins of the *Punzi Figure of Merit* evaluated as a function of the selection are shown in Figure 6.8. Uncertainties are evaluated as $\delta\epsilon(t)/[a/2+\sqrt{B(t)}]$ (setting $a = 1.6$), where $\delta\epsilon(t)$ is the efficiency uncertainty and $B(t)$ is the number of background events that pass the selection for each mass bin. The curve shows a region in which the value of the figure of merit reaches its maximum and it is quite stable, and the correspondent value t to use in the selection is chosen in this region of stability. The values obtained from the selection are shown in Table 6.2.

6.4 Sensitivity of *Belle*II

The number of background events in each mass bin and the signal efficiency from the optimized selection, together with the signal resolution for the different Z' mass hypothesis, the luminosity, the acceptance of the detector and the relative uncertainties are used in the *Bayesian Analysis Toolkit* (BAT) software [97] to estimate the 90% *CL* upper limits on the cross section of the process. The goal is to evaluate the sensitivity of the experiment on the g' coupling constant at 90% of confidence level, for each Z' mass hypothesis.
For each considered case, the upper limits on the cross section of the process can be

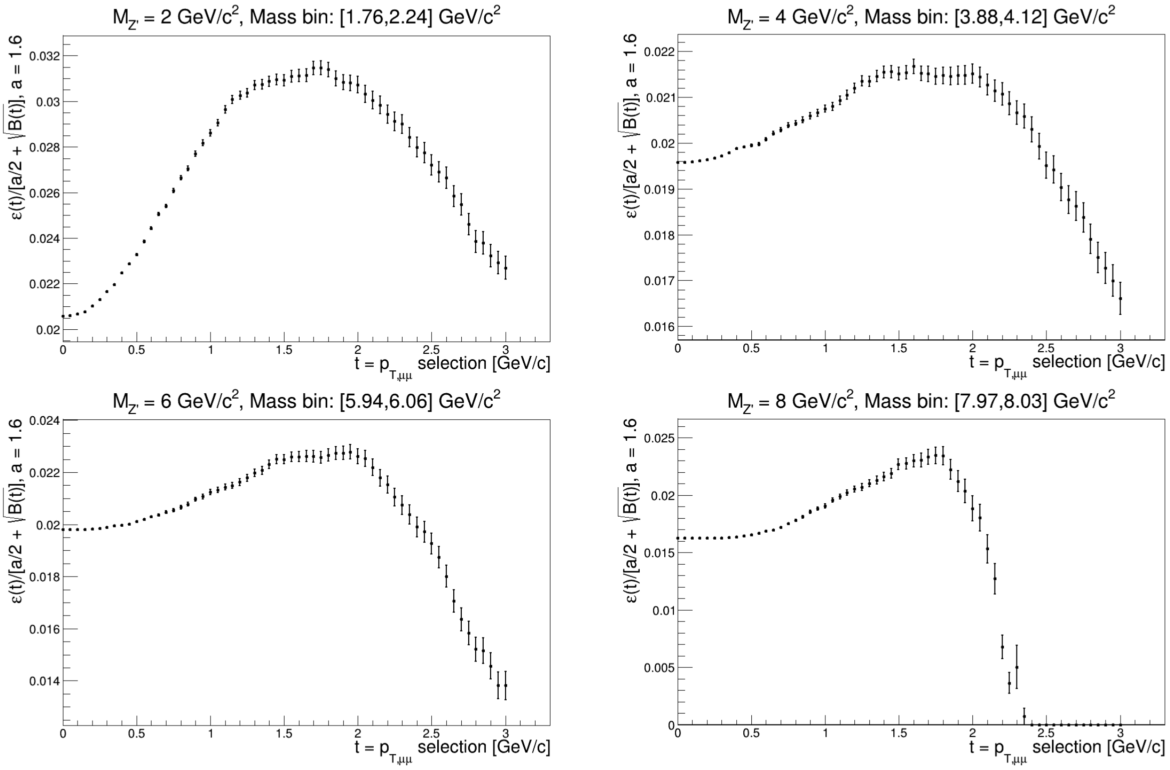

Figure 6.8: *Some examples of the Punzi Figure of Merit* as a function of the selection t, for different Z' mass hypothesis.

$M_{Z'}$ (GeV/c^2)	Mass bin (GeV/c^2)	t (GeV/c)	$B(t)$	$\epsilon(t)$
1	[0.60, 1.40]	1.75	208	0.591 ± 0.008
2	[1.76, 2.24]	1.75	505	0.732 ± 0.007
3	[2.84, 3.16]	1.70	956	0.787 ± 0.006
4	[3.88, 4.12]	1.80	1248	0.776 ± 0.007
5	[4.91, 5.09]	1.80	1285	0.768 ± 0.007
6	[5.94, 6.06]	1.80	926	0.708 ± 0.008
7	[6.96, 7.04]	1.70	590	0.63 ± 0.01
8	[7.97, 8.03]	1.80	173	0.33 ± 0.01

Table 6.2: Summary of the selection chosen for the different mass bins. $B(t)$ is the number of background events evaluated in the mass bin at the integrated luminosity of 10 fb^{-1}, $\epsilon(t)$ is the signal efficiency of the selection evaluated.

translated into the upper limits of the parameters of the $L_\mu - L_\tau$ model, which is described in Section 1.3.1.

The method used to estimate the 90% CL upper limits is described below:

- MC samples production: The MadGraph5 (MG5) generator used to generate the signal events computes the partial width of the Z' decay given the Z' mass and the coupling g' and then it generates the events and provides estimation of the production cross section multiplied by the assumed $B.R.$, which can be computed starting from the Table 1.5 reported in Section 1.3.1, where the partial widths are estimated from the model;
- BAT software estimation: The MC samples produced by MG5 are then used to optimize the analysis method by exploiting the properties studied on the signal MC

sample and identifying the most efficient selection criteria for signal and background separation. The efficiency values obtained from this study are then supplied to the BAT software that computes the 90% CL upper limits of the cross section of the process, again multiplied by the estimated $B.R.$, except for the case $B.R. = 1$, where it is assumed the Z0 decays into a kinematically allowed light DM;

- the production cross section provided by MG5 is estimated for a given value of g' and since in the production vertex (see Figure 1.14) g' enters linearly, the cross section, being proportional to $|M^2|$, goes like g'^2. If the g' used in MG5 to generate the events is for example $g' = 0.01$ then the cross section for $\hat{g}' = 0.001$ is simply the cross section estimated from MG5 with $g = 0.01$ multiplied by $(\hat{g}'/g')^2$;

- the BAT software provides an estimation of the measured cross section that can be compared with the cross section estimated from MG5 to obtain the value of g' measured from the data;

- the same procedure has to be repeated for each $M_{Z'}$ generated.

The number of background events and the signal efficiency evaluated from the MC samples, after the optimization of the selection, have been used to evaluate the 90% CL upper limits on the parameters of the $L_\mu - L_\tau$ model $(g', M_{Z'})$, and the curves in Figure 6.9 report the upper limits obtained for different integrated luminosity at the *Belle*II experiment: the integrated luminosity refers to the expected one for the end of the *Phase*-2, which was of 20 fb^{-1}, the full data size expected for *Belle*II, which is of 50 ab^{-1}, and an intermediate integrated luminosity of 2 ab^{-1}. The solid lines refer to the sensitivity on the g' parameter as a function of the Z' mass in the hypothesis that the Z' decays in a neutrino pair final state, which are evaluated accounting for the $B.R.$ estimated from the model, reported in Table 1.5, while the dashed lines refer to a $B.R. = 1$, which is assumed if the Z' decays in dark matter particle final state, which should be the favored channel if a dark matter particle lighter than the Z' exists. In the case $M_{Z'} < 2M_\mu$ the branching ratio $B.R.(Z' \to \nu\bar{\nu}) = 1$ and the solid line becomes equal to the dashed line.
These estimated upper limits are still a very preliminary result.
Finally, the red band represents the values of the parameter space which can explain the anomalous magnetic moment of the muon $(g-2)_\mu \pm 2\sigma$. The poor resolution for small Z' masses and the cross decreasing for higher Z' masses allow to be sensitive on the sensitivity to the parameters of the $L_\mu - L_\tau$ model at *Belle*II only in the range $1 < M_{Z'} < 8$ GeV$/c^2$. This is the reason why the curves are flat for $M_{Z'} < 1$ GeV$/c^2$.
The sensitivity obtained is a very preliminary result since it must be considered that the sensitivity estimated does not take in account tracking and trigger efficiencies. Currently the studies about the trigger efficiency and the track finding efficiency are ongoing. It should be noted that the most of the analysis, and in particular the selection, is model independent, and can also be used to constraint other new physics models with the same experimental signature. The limits on g' are of course obtained using the $L_\mu - L_\tau$ model and only apply in that context.

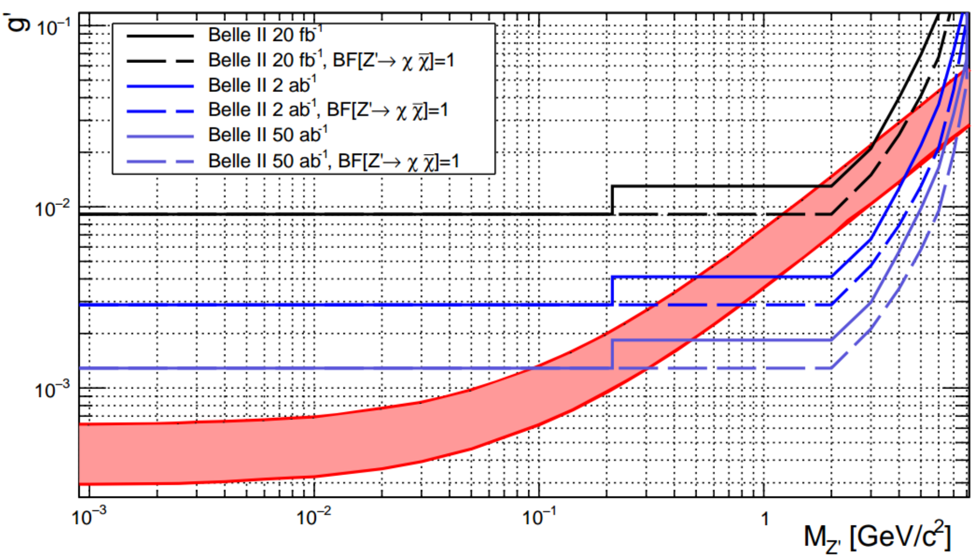

Figure 6.9: The 90% CL upper limits to the g' as a function of $M_{Z'}$ for different integrated luminosities at *Belle*II. The solid lines represent the case where the Z' boson decays in a neutrino pair and are estimated considering the partial widths estimated from the $L_\mu - L_\tau$ model, while the dashed lines represent the case where the invisible decay of the Z' is in a light dark matter particle final state, i.e. assuming $B.R. = 1$. This is a very preliminary result.

6.5 First results on data at *Belle*II

The data sample collected during the *Phase*-2 corresponds to an integrated luminosity of 505 pb^{-1}, which is being used to rediscover the early physics and to test the detector performances. Some examples of the recent results obtained in the reconstruction of photons and charged tracks, are shown in the following section.

Tracks reconstruction performance The capability to reconstruct a charged track identified as a muon has been tested through the reconstruction of the J/ψ mass peak in a data set that corresponds to an integrated luminosity of 250 pb^{-1}, shown in Figure 6.10 (left), that has been extracted from a kinetic fit to the invariant mass of the muon pair in the process $J/\psi \to \mu^+\mu^-$.

The J/ψ mass peak has been reconstructed also by a kinetic fit to the invariant mass of an electron pair in the process $J/\psi \to e^+e^-$ in a data set of 476 pb$^-$1, see Figure 6.10 (right).

Photon reconstruction performance The capability to reconstruct photons has been tested by reconstructing the mass of the π^0 in process $\pi^0 \to \gamma\gamma$ in a data set of 5 pb^{-1}, selecting photons with $E_\gamma > 150$ MeV, see Figure 6.11 (left). Moreover, photon reconstruction as the recoil against a muon pair in the processes $e^+e^- \to \mu^+\mu^-(\gamma)$ has been tested on a data set of 250 pb^{-1}, for a photon momentum range of $1 < p_{recoil} < 8$ GeV/cm (see Figure 6.11, right).
A good reconstruction of the photon, performed for example studying the photon as recoil with respect to the muon pair in the process $e^+e^- \to \mu^+\mu^-(\gamma)$, is necessary also for the analysis presented in this thesis, in particular for what concerns the optimization of the selection based on photon discriminating variables used for the background rejection.

Longitudinal size of the IP The performances of all the detector subsystems have been tested with the measurement of the longitudinal size of the IP, $z0$, by reconstructing two-tracks events in the first data at *Belle*II, see Figure 6.12.
The measured $z0$ for a given track is also exploited to provide the definition of a good track.

For what concerns the analysis presented in this thesis, a very preliminary MC-data comparison, on some relevant variables for the Z' to invisible search, has been performed using the background MC samples corresponding to an integrated luminosity of 10 fb^{-1} described in Section 5.4 and the fifth reprocessing of the data set currently available. Both MC sample and data set have been reconstructed using the reconstruction and preselection described in Section 6.1, the only difference regards the muon selection, since PID and vertexing, both currently under study, are not applicable on *Phase*-2 data set. The ongoing analysis proved that an efficient muon selection can be obtained by requiring:

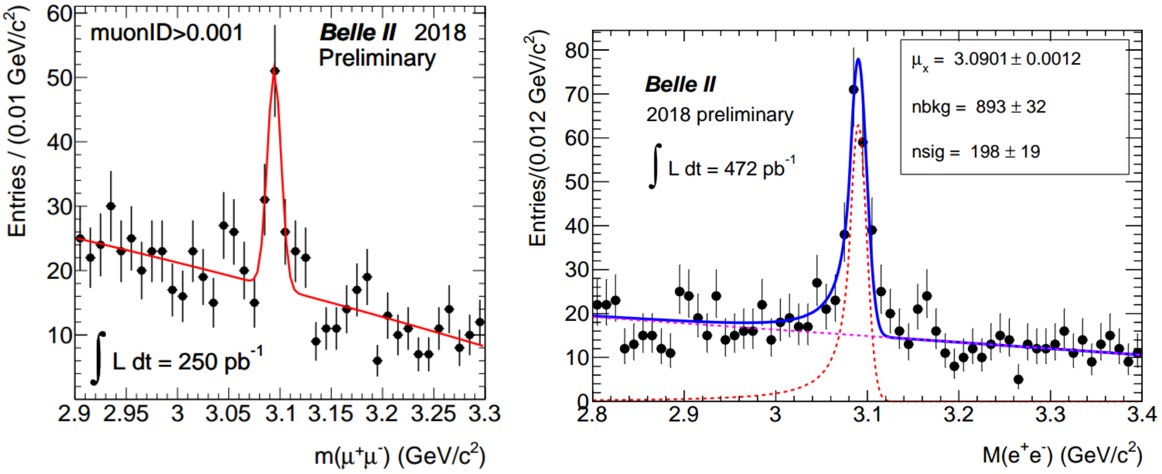

Figure 6.10: Left: the invariant mass distribution of $J/\psi \rightarrow \mu^+\mu^-$ candidates in 250 pb^{-1} of *Phase*-2 data. Right: the invariant mass distribution of $J/\psi \rightarrow e^+e^-$ candidates in 476 pb^{-1} of Phase 2 data.

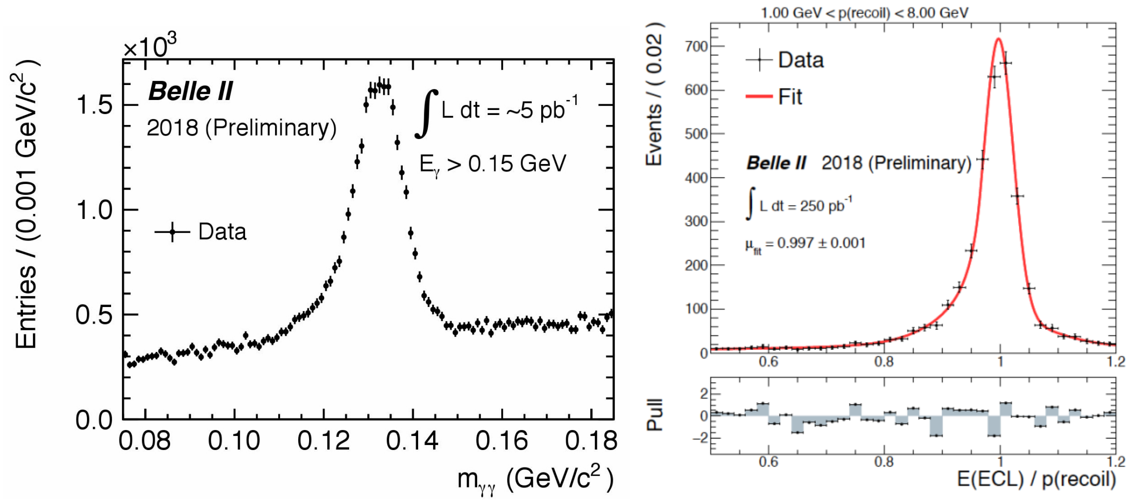

Figure 6.11: Left: the invariant mass distribution of $\pi^0 \rightarrow \gamma\gamma$ in 5 pb^{-1} of *Phase*-2 collision data. The photons coming from the π^0 candidates are required to have an energy higher than 150 MeV and to be within the acceptance of the CDC. Right: the single photon reconstruction as recoiling momentum against the muon pair, in $e^+e^- \rightarrow \mu^+\mu^-(\gamma)$ events.

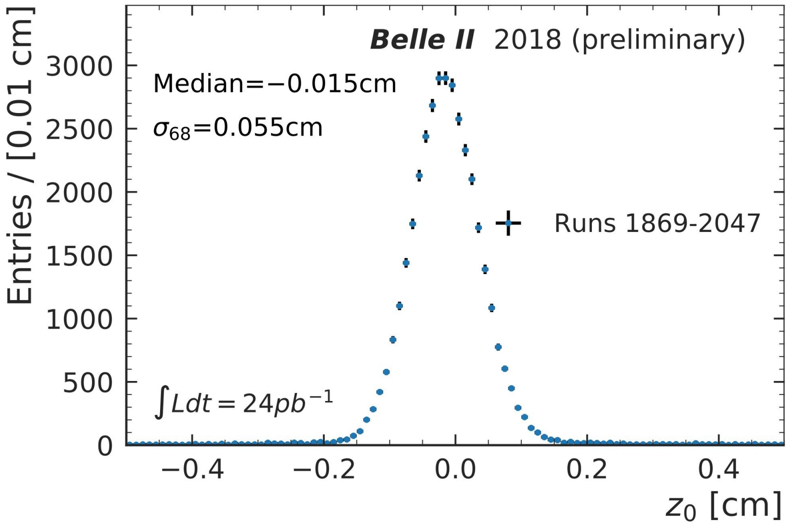

Figure 6.12: Distribution of the longitudinal size of the IP $z0$ measured on two-track events using the first data collected at *Belle*II.

- at least an ECL cluster associated to the tracks;
- the energy deposit in the cluster associated to the tracks must be lower than 400 MeV;
- the ratio between the energy and the momentum associated to the tracks must be lower than 0.25.

This muon selection has been applied to produce the preliminary MC-data comparison plots. An additional selection based on the transverse momentum of dimuon candidate by requiring $p_{T\mu\mu} > 1$ GeV/c has been applied, for this preliminary comparison the optimization through the *Punzi Figure of Merit* has not be considered yet.
The following graphs are produced without taking into account the trigger efficiency on data, since it is currently under study, and the histograms have been normalized to the number of entries. Although a full understanding of these plots is still missing and is under study, they provide a first look at data.

Figure 6.13 shows the MC-data comparison for the $d0$ distribution, where $d0$ is the distance of the tracks from the IP in the transverse plane, and for the $z0$ distribution, where $z0$ is the distance of the tracks from the IP along the beam axis. Both distributions shown here are relative to the μ^+ tracks. The $d0$ distribution obtained from data shows two peaks that can be explained by the fact that the IP is not positioned at nominal $x = y = 0$. This produces a modulation in $d0$ as a function of the azimuthal angle ϕ, as shown in Figure 6.14. Since the minimum and maximum of this oscillation are more populated, this generates the observed double peaks when projecting onto $d0$ axis.
Also the $z0$ distribution for data shows a shift with respect to that obtained from the MC simulation, indicating that the real collision point does not coincide with the nominal IP. It has to be noticed that the selection of tracks requires tracks coming from the IP, indeed the selection $d0 < 0.5$ cm and $z < 2$ cm, which is a quite loose selection, has been applied. Figure 6.15 shows the transverse momentum distributions (above) and the polar angle distributions (below) respectively of the dimuon candidate (left) and of the recoil with respect to the muon pair (right).

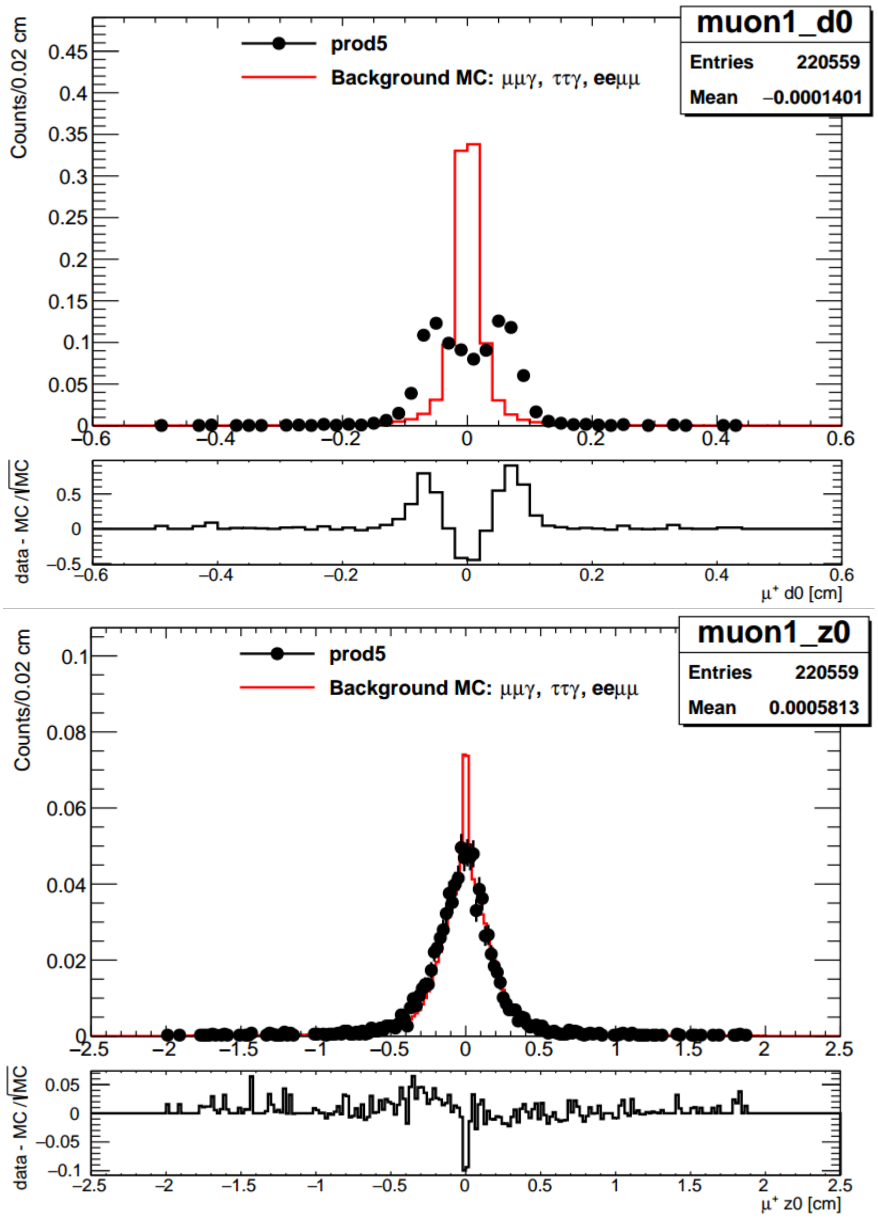

Figure 6.13: Above: MC-data comparison for the $d0$ distribution. Below: MC-data comparison for the $z0$ distribution. Both have been obtained for μ^+ tracks, but they are the same for μ^- tracks as expected.

From the distribution of the recoil polar angle it can be noticed that the selection of events where the direction of the recoil points in the acceptance of the barrel ECL, i.e. in the range $33^o < \theta < 128^o$ ($\sim$[0.58, 2.23] rad), has been applied. Again, for both variables a shift between data and MC distribution is observed, and this feature is still to be investigated.

Figure 6.16 shows the transverse momentum of the muons (above) and their polar angle (below). It is interesting to observe that around 0.58 rad ($\sim 33^o$) and 2.25 rad ($\sim 128^o$) the muon polar angular distributions show a dip, the reason is that only tracks with a cluster associated are reconstructed and in correspondence of those angles there is a gap between the barrel ECL and the endcaps ECL in which the clusters are not reconstructed. The acceptance covered by the endcaps ECL is approximately in the ranges $17^o \lessapprox \theta \lessapprox 33^o$ (forward endcap) and $128^o \lessapprox \theta \lessapprox 155^o$ (backward endcap), which corresponds to $\sim$[0.29,0.58] rad and $\sim$[2.25,2.71] rad, for this reason the observed discrepancies could be explained with a problem of association of clusters with tracks in the endcaps ECL. For what concerns the structures observed in the distributions in the range corresponding to the barrel region of the ECL, it is possible that they can be solved applying the trigger efficiency on data, but this is an ongoing study.

The graphs shown in this section are still under investigation, however, they represents the very first look at data for this analysis and they are a starting point to provide a full understanding of the detector and on how to further proceed with this study, although the

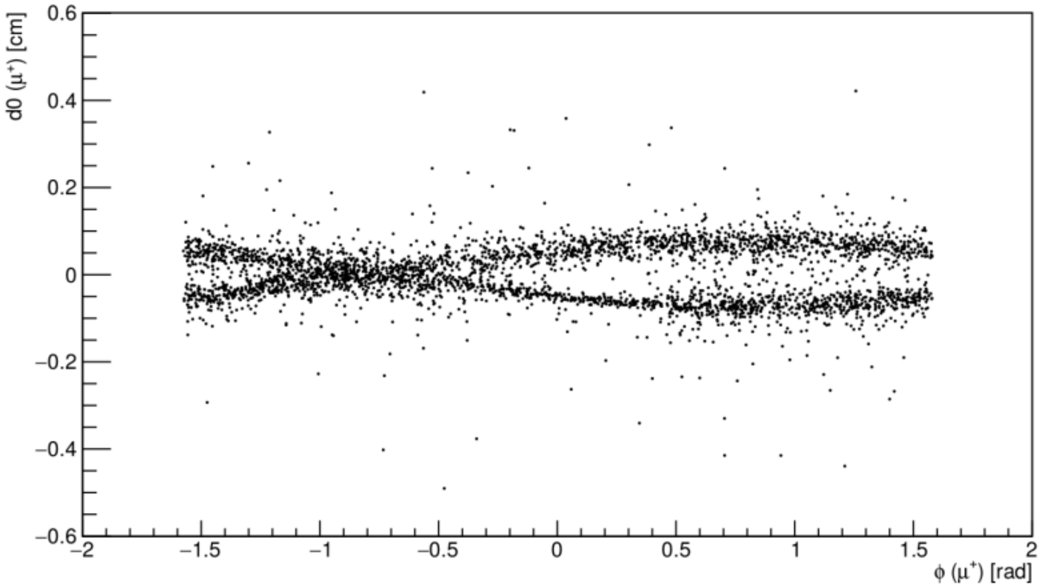

Figure 6.14: Modulation observed for $d0$ as a function of the azimuthal angle ϕ, due to the fact that the true IP is not at $x = y = 0$. The modulation projected onto the $d0$ axis causes the two peaks in $d0$ distribution shown in Figure 6.13.

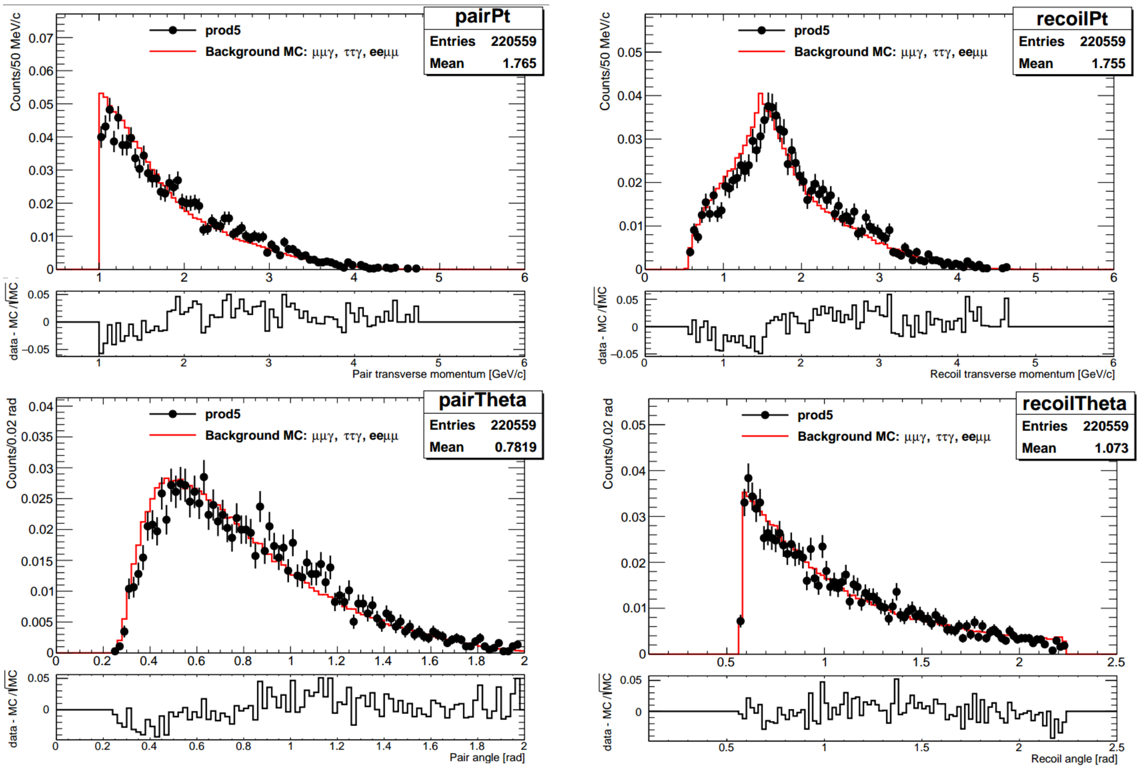

Figure 6.15: MC-data comparison of the transverse momentum distributions (above) and of the polar angle distributions (below), respectively of the dimuon candidate (left) and of the recoil (right).

Phase-2 data will not be used for the final analysis.

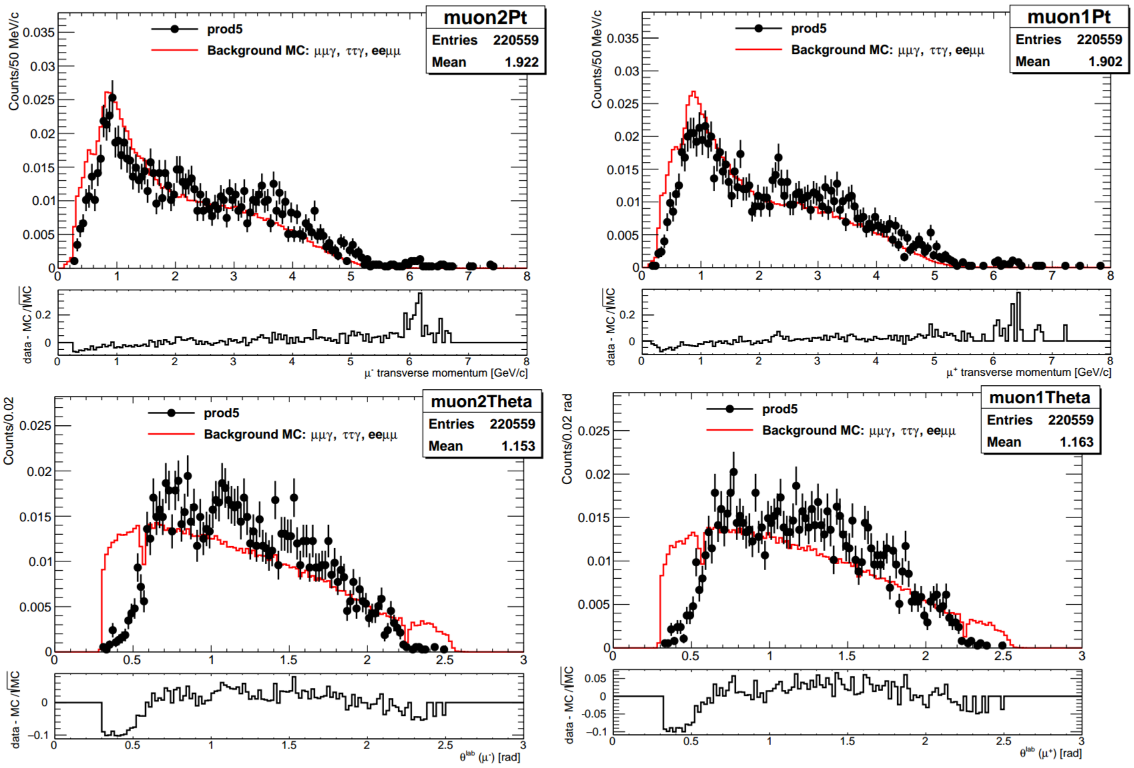

Figure 6.16: Above: MC-data comparison of the transverse momentum (above) and of the polar angle (below) distributions, respectively of the μ^- (right) and of the μ^+ (left).

Conclusions

In this thesis work, a MC-based preliminary analysis of the process $e^+e^- \to \mu^+\mu^- Z'(Z' \to \text{Invisible})$ that allows to estimate the sensitivity of *Belle*II on the parameters $(g', M_{Z'})$ of the $L_\mu - L_\tau$ model for different integrated luminosities has been presented. The 90% CL upper limits on the parameters of the model have been estimated through a preliminary optimization of the selection performed only by using the transverse momentum of the dimuon candidate as discriminating variable. Further discriminating variables are currently under study and when they will be fully understood, an approach based on the *Multivariate Analysis*, which also takes into account the correlations between the discriminating variables, will be tested.

The $L_\mu - L_\tau$ is a theoretically and experimentally well motivated model that extends the SM with an additional symmetry that preserves the difference between the leptonic number of the muon and tauon, therefore it is a theory free of gauge anomalies and renormalizable. This theory introduces a light Z' boson that couples only with muons and tauons through a coupling constant with leptons g', and it could explain the DM relic abundance in the Universe as well as the $(g-2)_\mu$ anomaly and the neutrino mass for a coupling constant $g' \sim 10^{-4} - 10^{-3}$ and for a Z' mass in the range MeV/c^2-GeV/c^2 [98]. Furthermore, recent experimental results, already mentioned in the thesis, showed the phenomenology introduced by this model as a possible explanation for some tensions between the measurements obtained and the SM prediction.

The purpose of this thesis is to show the feasibility of the search for the process $e^+e^- \to \mu^+\mu^- Z'(Z' \to \text{Invisible})$ at *Belle*II, which is theoretical well motivated. Furthermore, although the data set collected at *Belle*II during the *Phase*-2 is not enough to reach the estimated sensitivity obtained from simulations and the detector performances are not the optimal ones yet, it is relevant to note that the goal of the presented preliminary analysis is to test the detector performances and to improve the knowledge about the analysis tools, used and developed in this analysis, in order to be ready for the larger data set that will be collected during the *Phase*-3.

As regards specifically the future of the analysis, the next steps are to understand the collected data in order to study what has been observed through the MC simulations, define a definitive analysis strategy optimized on the MC-data comparison and finally validate the analysis method through the MC-data comparison. In particular:

- complete the study of further variables with high discriminating power between signal and background events, and finalize the selection optimization through the *Punzi Figure Of Merit* method. The possibility to implement a multivariate analysis to further separate the signal from the background, especially for what concerns the rejection of $e^+e^- \to \tau^+\tau^-(\gamma)$ and $e^+e^- \to e^+e^-\mu^+\mu^-$ events will be studied;
- model the recoil mass distributions for signal events by introducing the ISR tail effect.

To account for this effect a more complicated model with respect to the sum of three Gaussians is required, since the ISR effect introduce a radiative tail for high values of the signal M_{recoil} distribution, which should be a combination of a Gaussian and a Crystal ball function;

- compare the MC-data shapes and the validate of the MC-based selection on data, which requires to fully understand the detector performances. In particular it is fundamental to study the trigger and the track finding efficiencies, whose study strategies have already been defined;
- define the method to evaluate the upper limits on the parameters of the model before unblinding the recoil mass distribution, for the signal yield extraction;
- study of the systematic uncertainties that contribute to the analysis;

The studies to fully understand the detector performances are already ongoing and they are performed on the data set currently available, which corresponds to an integrated luminosity of 505 pb^{-1}. With these studies *Belle*II has already shown to be able to rediscover the early physics that is accessible with the current data sample.

Currently, two main studies on first collision data are of particular interest for the search studied in this thesis: one regards the trigger efficiency for two muon tracks events and the other regards the track finding efficiency. Both are ongoing studies and they are expected to be finalized before the beginning of *Phase*-3, probably in February or March 2019.

Finally, the particle identification is necessary to improve the rejection of events characterized by tracks mis-identified as muons and a tuning of the PID variables is fundamental to do a comparison between data and MC simulations. The variables providing particle identification probability are currently under study.
For what concerns the identification of muons, since there were some issues with the KLM, which is the most relevant sub-detector for the identification of muons, during the *Phase*-2 data taking period, the use of PID variables to select muon candidates is currently deprecated. For this reason, ongoing analyses use a selection that consists of employ the ECL information about the energy deposit in clusters associated to the tracks and the measurement of the momentum of the tracks for the muon identification. In particular, it has been shown that a selection consisting of require ECL clusters with an energy deposit lower than 0.4 GeV and the ratio E/p lower than 0.25 allows to remove electron contamination, but to reject background due to the mis-identification of pions as muons, further optimization based on PID is needed.

During the work related to the analysis, also a contribution to improve the performances to the SVD subsystem has been given. In particular the work done within the SVD group concerned the development of the calibration method of the algorithm employed by the SVD to estimate the *hit time* of particles crossing each sensor, which is called $\mathcal{COG}$. Precise timing information are relevant for the background rejection of those events that are off-time with respect tp the *event time* or due to the combinatorial association of the positional information provided by the SVD. The first layer of the SVD is distant about 3.9 cm from the IP so the levels of background that the SVD must face are very high in the high luminosity environment of SuperKEKB, indeed the simulations showed the difficulties to perform tracking efficiently due to the high number of background hits with respect to the signal hits, in particular in the first SVD layer. For this reason the rejection of background is very important and the timing information provided by the SVD allow to do that. The method consists of using the *event time* estimation provided by the CDC, which is currently the only available, in order to correct the *hit time* estimation provided by the SVD. After the calibration, a final resolution of ~4 ns, for the V/n-side of the sensors composing the SVD layers, have been obtained. The result is quite good, but the resolution for the U/p-side of the sensors and the potentiality of the calibration for what concerns the background rejection must be evaluated on data yet. Finally also the uncertainty to associate to the calibrated value of the must be estimated.

Concluding, the work presented in this thesis is a very preliminary analysis that allows to understand the feasibility for the search of $e^+e^- \to \mu^+\mu^- Z'$, ($Z' \to$ Invisible) at *Belle*II. The process analyzed has never been studied before in other experiments and the idea was to perform the full analysis on the expected 20 fb^{-1} for the *Phase*-2. Due to the smaller data set collected of only 505 pb^{-1}, it has been possible only to perform some MC-based preliminary analyses, which is however important to highlight the issues to be faced for preparing the analysis on a larger data set and to test the tools implemented. An estimate of the sensitivity to a theoretically well motivated new physics model has been provided for different integrated luminosities foreseen at *Belle*II. Although the analysis strategy is not completely defined yet and there are several studies to be optimized, a very preliminary MC-data comparison has been performed between the background MC samples produced, which corresponds to an integrated luminosity of 10 fb^{-1}, and the fifth reprocessing of the data set collected.

Bibliography

[1] The BABAR Collaboration. *An Introduction to Quantum Field Theory*. Westview Press, 1998.

[2] M. Tanabashi et al. “Particle Data Group”. In: (2018). URL: `http://pdglive.lbl.gov/Viewer.action`.

[3] Nicola Cabibbo. “Unitary Symmetry and Leptonic Decays ”. In: (1963). URL: `https://journals.aps.org/prl/pdf/10.1103/PhysRevLett.10.531`.

[4] Gianfranco Bertone, Dan Hooper, and Joseph Silk. “Particle Dark Matter: Evidence, Candidates and Constraints”. In: (2004). URL: `https://arxiv.org/pdf/hep-ph/0404175.pdf`.

[5] T. S. Albada et al. “Distribution of Dark Matter in the Spiral Galaxy NGC 3198”. In: (1985). URL: `http://articles.adsabs.harvard.edu/cgi-bin/nph%20iarticle_query?db_key=AST&bibcode=1985ApJ...295..305V&letter=.&classic=YES&defaultprint=YES&whole_paper=YES&page=305&epage=305&send=Send+PDF&filetype=.pdf`.

[6] Charles W. Misner, Kip S. Thorne, and John Archibald Wheeler. *Gravitation*. W. H. Freeman and Company, 1973.

[7] Lars Bergström and Ariel Goobar. *Cosmology and Particle Astrophysics, 2° Ed.* Springer, Praxis Publishing, 2006.

[8] Maurizio Gasperini. *Lezioni di Cosmologia Teorica*. Springer, 2012.

[9] Bernard Schutz. *A first course in General Relativity*. Cambridge University Press, 2009.

[10] Wilkinson Microwave Anisotropy Probe (WMAP) team. *WMAP 9-year results released*. URL: `https://map.gsfc.nasa.gov/news/`.

[11] R. G. Hamish Robertson. “KATRIN: an experiment to determine the neutrino mass from the beta decay of tritium”. In: (2013). URL: `https://arxiv.org/abs/1307.5486`.

[12] I. Bigi. “CP Violation - An Essential Mystery in Nature′s Grand Design”. In: (1997). URL: `https://arxiv.org/abs/hep-ph/9712475`.

[13] Tha Macho Collaboration. “The MACHO Project: Microlensing Results from 5.7 Years of LMC Observations”. In: (2000). URL: `https://arxiv.org/abs/astro-ph/0001272v1`.

[14] Miguel A. Monroy-Rodríguez and Christine Allen. “The end of the MACHO era-revisited: new limits on MACHO masses from halo wide binaries”. In: (2014). URL: `https://arxiv.org/abs/1406.5169v1`.

[15] Monique Signore and Denis Puy. “Cosmic microwave background and first molecules in the early Universe”. In: (2009). URL: https://www.researchgate.net/publication/226870591_Cosmic_microwave_background_and_first_molecules_in_the_early_universe?enrichId=rgreq-f58da7b7b38cd7bb1602b680542abf15-XXX&enrichSource=Y292ZXJQYWdlOzIyNjg3MDU5MTtBUzozNTc2ODUxMTY1ODgwMzJAMTQ2MjI5MDE4NTQ1NA==&el=1_x_3&_esc=publicationCoverPdf.

[16] John Macdonald. “Generation of WIMP Miracle-like Densities of Baryons and Dark Matter”. In: (2012). URL: https://arxiv.org/pdf/1201.3124.pdf.

[17] R. Essig et al. “Dark Sectors and New, Light, Weakly-Coupled Particles”. In: (2013). URL: https://arxiv.org/pdf/1311.0029v1.pdf.

[18] Michel Cassé and Pierre Fayet. “Light Dark Matter”. In: (2005). URL: https://arxiv.org/abs/astro-ph/0510490v1.

[19] John F. Beacom, Nicole F. Bell, and Gianfranco Bertone. “Gamma-Ray Constraint on Galactic Positron Production by MeV Dark Matter”. In: (2004). URL: https://arxiv.org/abs/astro-ph/0409403v1.

[20] C. Bœhm et al. “Light and Heavy Dark Matter Particles”. In: (2003). URL: https://arxiv.org/abs/hep-ph/0311143v1.

[21] C. Bird, R. Kowalewski, and M. Pospelov. “Dark matter pair-production in $b \to s$ transitions.” In: (2006). URL: https://arxiv.org/abs/hep-ph/0601090v2.

[22] Jim Alexander et al. “Dark Sectors 2016 Workshop: Community Report”. In: (2016). URL: https://arxiv.org/abs/1608.08632.

[23] David E. Kaplan. “Asymmetric Dark Matter”. In: (2009). URL: https://arxiv.org/pdf/0901.4117.pdf.

[24] Rouven Essig et al. “Direct Detection of sub-GeV Dark Matter with Semiconductor Targets”. In: (2016). URL: https://arxiv.org/pdf/1509.01598.pdf.

[25] Yonit Hochberg et al. “Mechanism for Thermal Relic Dark Matter of Strongly Interacting Massive Particles”. In: (2014). URL: https://arxiv.org/abs/1402.5143.

[26] Eric Kuflik et al. “Elastically Decoupling Dark Matter”. In: (2016). URL: https://arxiv.org/abs/1512.04545.

[27] L. Bouchet et al. “INTEGRAL SPI All-Sky View in Soft Gamma Rays: Study of Point Source and Galactic Diffuse Emissions”. In: (2008). URL: https://arxiv.org/abs/0801.2086.

[28] R. Bernaber et al. “Dama Results”. In: (2003). URL: https://arxiv.org/abs/astro-ph/0305542v2.

[29] O. Adriani et al. “An anomalous positron abundance in cosmic rays with energies 1.5-100 GeV”. In: (2009). URL: https://www.nature.com/articles/nature07942.

[30] A. U. Abeysekara et al. “Extended gamma-ray sources around pulsars constrain the origin of the positron flux at Earth”. In: (2017). URL: http://science.sciencemag.org/content/sci/358/6365/911.full.pdf.

[31] FERMI LAT Collaboration. “Measurement of separate cosmic-ray electron and positron spectra with the Fermi Large Area Telescope”. In: (2012). URL: https://arxiv.org/abs/1109.0521.

[32] AMS-02 Collaboration. “High Statistics Measurement of the Positron Fraction in Primary Cosmic Rays with the Alpha Magnetic Spectrometer on the International Space Station”. In: (2016). URL: https://arxiv.org/pdf/1612.09579.pdf.

[33] Fred Jegerlehner and Andreas Nyffeler. “The Muon g-2”. In: (2009). URL: https://arxiv.org/pdf/0902.3360v1.pdf.

[34] C. Langerbruch. “Lepton Flavour Universality tests in B decays as a probe for New Physics”. In: (2018). URL: https://arxiv.org/pdf/1805.04370.pdf.

[35] David Curtin et al. “Illuminating Dark Photons with High-Energy Colliders”. In: (2015). URL: https://arxiv.org/abs/1412.0018v2.

[36] Gordan Krnjaic. “Probing Light Thermal Dark-Matter With a Higgs Portal Mediator”. In: (2016). URL: https://arxiv.org/abs/1512.04119.

[37] R. D. Peccei and Helen R. Quinn. “Constraints imposed by CP conservation in the presence of pseudoparticles”. In: (1977). URL: https://journals.aps.org/prd/pdf/10.1103/PhysRevD.16.1791.

[38] *Fundamental Physics at the Intensity Frontier*. 2012. URL: https://arxiv.org/abs/1205.2671.

[39] Frank F. Deppisch, P. S. Bhupal Dev, and Apostolos Pilaftsis. “Neutrinos and Collider Physics”. In: (2015). URL: https://arxiv.org/abs/1502.06541.

[40] Bob Holdom. “Two U(1)’s and Epsilon Charge Shifts”. In: (1986). DOI: 10.1016/0370-2693(86)91377-8.

[41] Kai Schmitz. “Kinetic Mixing in Field Theory”. In: (2009). URL: https://bib-pubdb1.desy.de/record/88159/files/Kinetic_Mixing_in_Field_Theory.pdf.

[42] S. Heinemeyer and C. Schappacher. “High-Precision Electroweak SUSY Production Cross Sections at e^+e^- Colliders”. In: *14th DESY Workshop on Elementary Particle Physics: Loops and Legs in Quantum Field Theory 2018 (LL2018) St Goar, Germany, April 29-May 4, 2018*. 2018. URL: https://arxiv.org/pdf/1807.04009.pdf.

[43] Hitoshi Murayama. “Supersymmetry phenomenology”. In: *Proceedings, Summer School in Particle Physics: Trieste, Italy, June 21-July 9, 1999*. 2000. URL: https://arxiv.org/abs/hep-ph/0002232.

[44] Duarte Azevedo et al. “Models with Extended Higgs Sectors at Future e^+e^- Colliders”. In: (2018). URL: https://arxiv.org/abs/1808.00755.

[45] Julian Heeck and Werner Rodejohann. “Gauged $L_\mu - L_\tau$ Symmetry at the Electroweak Scale”. In: (2011). URL: https://arxiv.org/abs/1107.5238v2.

[46] T. Araki et al. “Detecting the $L\mu - L\tau$ gauge boson at Belle II”. In: (2017). URL: https://arxiv.org/abs/1702.01497.

[47] Wolfgang Altmannshofer et al. “Dressing $L_\mu - L_\tau$ in Color”. In: (2016). URL: https://arxiv.org/abs/1403.1269.

[48] A. J. Krasznahorkay, T. J. Ketel, and A. Krasznahorkay. “Observation of Anomalous Internal Pair Creation in ^{8}Be: A Possible Indication of a Light, Neutral Boson”. In: (2016). URL: https://journals.aps.org/prl/pdf/10.1103/PhysRevLett.116.042501.

[49] IceCube Collaboration. “Observation of High-Energy Astrophysical Neutrinos in Three Years of IceCube Data”. In: (2014). URL: https://journals.aps.org/prl/pdf/10.1103/PhysRevLett.113.101101.

[50] Takeshi Araki et al. “Cosmic neutrino spectrum and the muon anomalous magnetic moment in the gauged $L\mu - L\tau$ model”. In: (2015). URL: https://journals.aps.org/prd/pdf/10.1103/PhysRevD.91.037301.

[51] Sean Fraser et al. “The EDGES 21 cm Anomaly and Properties of Dark Matter”. In: (2018). URL: https://arxiv.org/abs/1803.03245.

[52] Asher Berlin et al. “Severely Constraining Dark Matter Interpretations of the 21-cm Anomaly”. In: (2017). URL: https://arxiv.org/abs/1803.02804v1.

[53] Seungwon Baeka and Pyungwon Ko. “Phenomenology of $U(1)_{L_\mu - L_\tau}$ charged dark matter at PAMELA/FERMI and colliders”. In: (2009). URL: http://iopscience.iop.org/article/10.1088/1475-7516/2009/10/011/pdf.

[54] The BABAR Collaboration. “Search for a muonic dark force at BABAR”. In: (2016). URL: https://arxiv.org/abs/1606.03501.

[55] The BABAR Collaboration. “Search for invisible decays of a dark photon produced in e^+e^- collisions at BABAR”. In: (2017). URL: https://arxiv.org/abs/1702.03327v2.

[56] Eder Izaguirre et al. “Accelerating the Discovery of Light Dark Matter”. In: (2015). URL: https://arxiv.org/pdf/1505.00011.pdf.

[57] Haipeng An et al. “Probing the Dark Sector with Dark Matter Bound States”. In: (2016). URL: https://arxiv.org/pdf/1510.05020.pdf.

[58] Takeshi Araki et al. “Detecting the $L_\mu - L_\tau$ gauge boson at Belle II”. In: (2017). URL: https://journals.aps.org/prd/abstract/10.1103/PhysRevD.95.055006.

[59] Rouven Essig, Philip Schuster, and Natalia Toro. “Probing dark forces and light hidden sectors at low-energy e^+e^- colliders”. In: (2009). URL: https://journals.aps.org/prd/abstract/10.1103/PhysRevD.80.015003.

[60] Patrick J. Fox and Erich Poppitz. “Leptophilic Dark Matter”. In: (2009). URL: https://arxiv.org/pdf/0811.0399.pdf.

[61] The BABAR Collaboration. “Search for low-mass dark-sector Higgs bosons”. In: (2012). URL: https://arxiv.org/pdf/1202.1313.pdf.

[62] *Belle* Collaboration. “Search for the dark photon and the dark Higgs boson at Belle”. In: (2015). URL: https://arxiv.org/pdf/1502.00084.pdf.

[63] The KLOE Collaboration. “Search for dark Higgsstrahlung in $e^+e^- -> \mu^+\mu^-$ and missing energy events with the KLOE experiment”. In: (2015). URL: https://arxiv.org/abs/1501.06795.

[64] The BABAR Collaboration. “Search for new π^0-like particles produced in association with a τ-lepton pair”. In: (2014). URL: https://arxiv.org/abs/1411.1806v2.

[65] The BABAR Collaboration. “Search for a Narrow Resonance in e^+e^- to Four Lepton Final States”. In: (2009). URL: http://slac.stanford.edu/pubs/slacpubs/13750/slac-pub-13758.pdf.

[66] ATLAS Collaboration. "Search for Higgs bosons decaying to aa in the $\mu\mu\tau\tau$ final state in pp collisions at $\sqrt{s} = 8$ TeV with the ATLAS experiment". In: (2015). URL: https://arxiv.org/abs/1505.01609.

[67] CMS Collaboration. "Search for a very light NMSSM Higgs boson produced in decays of the 125 GeV scalar boson and decaying into tau leptons in pp collisions at $\sqrt{s} = 8$ TeV". In: (2016). URL: https://arxiv.org/abs/1510.06534.

[68] LHCb Collaboration. "Search for hidden-sector bosons in $B^0 \to K^{0*}\mu^+\mu^-$ decays". In: (2015). URL: https://arxiv.org/abs/1508.04094.

[69] LHCb Collaboration. "Search for Majorana neutrinos in $B^- \to \pi^+\mu^-\mu^-$ decays". In: (2014). URL: https://arxiv.org/abs/1401.5361.

[70] LHCb Collaboration. "Search for long-lived particles decaying to jet pairs". In: (2015). URL: https://arxiv.org/abs/1412.3021.

[71] Asmaa Abada et al. "Inclusive Displaced Vertex Searches for Heavy Neutral Leptons at the LHC". In: (2018). URL: https://arxiv.org/pdf/1807.10024.pdf.

[72] Martin Bauer, Matthias Neubertb, and Andrea Thammb. "Collider Probes of Axion-Like Particles". In: (2017). URL: https://arxiv.org/pdf/1708.00443.pdf.

[73] Emi Kou et al. "Belle II Theory Interface Platform". In: (2015).

[74] A. J. Bevan et al. "The Physics of the B Factories". In: (2015). URL: https://arxiv.org/pdf/1406.6311.pdf.

[75] Michael E. Peskin and Dan V. Schroeder. *The BABAR Physics Book: Physics at an Asymmetric B Factory*. 1995.

[76] Belle II Collaboration. "Belle II Technical Design Report". In: (2010). URL: https://arxiv.org/pdf/1011.0352.pdf.

[77] J. W. Flanagan and Y. Ohnishi. "Letter of Intent for KEK Super B Factory. Part III: Accelerator Design". In: (2004). URL: http://superb.kek.jp/documents/loi/img/LoI_accelerator.pdf.

[78] T. Hara, T. Kuhr, and Y. Ushiroda. "Belle II Coordinate System and Guideline of Belle II Numbering Scheme". In: (2011). URL: https://indico.mpp.mpg.de/event/2308/material/0/1?contribId=0.

[79] I. Adachi et al. "Detectors for extreme luminosity: Belle II". In: (2018). URL: https://www.sciencedirect.com/science/article/pii/S0168900218304200.

[80] Simo Ramo. "Currents Induced by Electron Motion". In: (1939). URL: https://ieeexplore.ieee.org/stamp/stamp.jsp?tp=&arnumber=1686997.

[81] Manfred Valentan. "The Silicon Vertex Detector for b-tagging at Belle II". In: (2013). URL: http://www.ub.tuwien.ac.at/diss/AC11413158.pdf.

[82] M.J. French et al. "Design and results from the APV25, a deep sub-micron CMOS front-end chip for the CMS tracker". In: (2011). URL: https://www.sciencedirect.com/science/article/pii/S0168900201005897#!.

[83] M. Staric. "Pattern recognition for the time-of-propagation counter". In: (2010). URL: https://www.sciencedirect.com/science/article/pii/S0168900210022473.

[84] T. Kuhr et al. "The Belle II Core Software". In: (2018). URL: https://arxiv.org/abs/1809.04299.

[85] Johan Alwall et al. "MadGraph 5 : Going Beyond". In: (2011). URL: https://arxiv.org/abs/1106.0522.

[86] Anders Ryd et al. "EvtGen: A Monte Carlo Generator for B-Physics". In: (2004). URL: http://robbep.home.cern.ch/robbep/EvtGen/GuideEvtGen.pdf.

[87] Torbjorn Sjostrand, Stephen Mrenna, and Peter Z. Skands. "A Brief Introduction to PYTHIA 8.1". In: (2008). URL: https://arxiv.org/abs/0710.3820.

[88] N. Davidson, T. Przedzinski, and Z. Was. "PHOTOS interface in C++: Technical and Physics Documentation". In: (2016). URL: https://arxiv.org/abs/1011.0937.

[89] S. Agostinelli et al. "GEANT4: A Simulation toolkit". In: *Nucl. Instrum. Meth.* A506 (2003), pp. 250–303. DOI: 10.1016/S0168-9002(03)01368-8.

[90] S. Jadach, B. F. L. Ward, and Z. Was. "The Precision Monte Carlo event generator K K for two fermion final states in e+ e- collisions". In: (2000). URL: https://arxiv.org/abs/hep-ph/9912214.

[91] G. Balossini et al. "Photon pair production at flavour factories with per mille accuracy". In: (2008). URL: https://arxiv.org/abs/0801.3360.

[92] Henryk Czyz and Agnieszka Grzelinska. "PHOKHARA 7.0 Monte Carlo generator: The Narrow resonances implementation and new pion and kaon form factors". In: (2011). URL: https://arxiv.org/abs/1101.2967.

[93] H. Czyż, M. Gunia, and J. H. Kühn. "Simulation of electron-positron annihilation into hadrons with the event generator PHOKHARA". In: (2013). URL: https://arxiv.org/abs/1306.1985.

[94] F. A. Berends et al. In: *Nucl. Phys.* 40 B253 (1985), pp. 441–463.

[95] Wolfgang Waltenberger, Winfried Mitaroff, and Fabian Moser. "RAVE - a Detector-independent Vertex Reconstruction Toolkit". In: (2007). URL: http://www.hephy.at/project/ilc/reports/RaveVertigo/Proceedings/07_VCI_rave.pdf.

[96] Giovanni Punzi. "Sensitivity of searches for new signals and its optimization". In: (2003). URL: https://arxiv.org/abs/physics/0308063.

[97] Allen Caldwell, Daniel Kollar, and Kevin Kroeninger. "BAT - The Bayesian Analysis Toolkit". In: (2008). URL: https://arxiv.org/abs/0808.2552v1.

[98] Sudhanwa Patra et al. "Gauged $U(1)_{L_\mu - L_\tau}$ model in light of muon $g-2$ anomaly, neutrino mass and dark matter phenomenology". In: (2017). DOI: 10.1016/j.nuclphysb.2017.02.010.

[99] Tom W. B. Kibble. "The Standard Model of Particle Physics". In: (2013). URL: https://arxiv.org/pdf/1412.4094.pdf.

[100] The BABAR Collaboration. "Search for a Dark Photon in e^+e^- Collisions at BABAR". In: (2014). URL: https://journals.aps.org/prl/abstract/10.1103/PhysRevLett.113.201801.